# 3D Printing of Activated Carbon and Exemplary Application as Adsorbent in the Electric Swing Adsorption

Steldinger, Hendryk

(2020)

DOI (TUprints): https://doi.org/10.25534/tuprints-00011724

Publication type: Ph.D. Thesis

Division: 07 Department of Chemistry

Original source: https://tuprints.ulb.tu-darmstadt.de/11724

# 3D Printing of Activated Carbon and Exemplary Application as Adsorbent in the Electric Swing Adsorption

## 3D Druck von Aktivkohle und ihre Anwendung als Adsorptionsmittel in einem Elektro-Swing-Adsorptionsprozess

TECHNISCHE
UNIVERSITÄT
DARMSTADT

**vom Fachbereich Chemie**
**der Technischen Universität Darmstadt**

zur Erlangung des Grades
*Doktor-Ingenieur*
(Dr.-Ing.)

**Dissertation**
**von Hendryk Steldinger**

| | |
|---|---|
| Erstgutachter /in: | Prof. Dr.-Ing. Dipl-Kfm. Bastian J. M. Etzold |
| Zweitgutachter /in: | Prof. Dr. Annette Andrieu-Brunsen |

Darmstadt, 2020

Steldinger, Hendryk: 3D Printing of Activated Carbon and Exemplary Application as Adsorbent in the Electric Swing Adsorption

Darmstadt, Technische Universität Darmstadt

Jahr der Veröffentlichung auf TUprints: 2020

URN: urn:nbn:de:tuda-tuprints-117243

**Tag der Einreichung: 30. April 2020**

**Tag der mündlichen Prüfung: 13. Juli 2020**

Diese Arbeit ist das Ergebnis der wissenschaftlichen Arbeit von Hendryk Steldinger am Ernst-Berl-Institut für technische und makromolekulare Chemie unter der Betreuung von Prof. Bastian J.M. Etzold vom Mai 2016 bis zum Oktober 2019.

Der sensible Mensch leidet nicht aus diesem oder jenem Grunde, sondern ganz allein, weil nichts auf dieser Welt seine Sehnsucht stillen kann.

**Jean-Paul Sartre**

## Acknowledgments

Mein herzlicher Dank gilt allen, die durch ihre Unterstützung, ihren Rat und ihr Engagement direkt oder indirekt zum Gelingen dieser Arbeit beigetragen haben - darunter besonders:

**Prof. Bastian J.M. Etzold -** Dafür, dass du es mir ermöglicht hast, dieses Projekt durchzuführen, obwohl es am Anfang nicht klar war, wie es funktionieren wird. Darüber hinaus, hast du uns mit deinem unermüdlichen Einsatz für deine Doktoranden den Rücken gestärkt und so eine konstruktive und offene Atmosphäre geschaffen.

**Prof. Anette Andrieu-Brunsen -** Für die Übernahme des Koreferats.

**Jan Gläsel -** Für deine exzellente Leitung unserer Arbeitsgruppe und dein stets offenes Ohr.

**Prof. Alfons Drochner -** Für die Anregungen und interessanten Gespräche nach Feierabend.

Meinen Kollegen des V1 Büros, namentlich **Hauke Christians, Miriam Geissler, Michael George, Florian Knaus, Johannes Landwehr, Timothy Nowak, Nikolai Schmitt, Marco Schöpp und Sebastian Wöllner -** Ihr wart der Quell vieler Ideen und ein großartiges Team bei der Uniolympiade. Ohne euch wäre die Promotion nur halb so abwechslungsreich gewesen.

Den Studenten **Chandra Prabowo, Matthias Roth, Joe Addo-Mensah, Alessandro Esposito** und **Fabian Kauzner**, die von der Konzeptionierung bis zur Anwendung mit Ehrgeiz an dem Thema 3D Druck von Kohlenstoffen geforscht haben.

**Marianne -** Dafür, dass du immer ein offenes Ohr hattest.

All my friends at the Polytechnic Institute of Bragança, especially **Adriano Henrique** for giving me a warm welcome during my studies there and for working on a great application of the 3D printed carbon. I appreciate your openness. Your way of living really broadened my horizon.

**Allen Mitgliedern des Aikikai Darmstadt e.V. -** Alle Probleme eines stressigen Tages waren nach einem Training mit euch vergessen.

Meinen Eltern **Falk** und **Bianka** und meinen Geschwistern **Rebekka, Viktoria** und **Lennart -** Ihr standet mir bei persönlichen Fragen bei und habt mich herausgefordert, meine Forschung auch mal allgemeinverständlich zu erklären.

Meinen Homies **Ruben, Richard, Klemens, Peter, Benjamin** und **Arvid -** Obwohl ich mittlerweile weit weg wohne und es nicht oft nach Berlin schaffe, ist es mit euch, als wäre ich nie weg gewesen.

Meinem Freund **Sebastian Ponce**, denn durch deine Offenheit und Ehrgeiz bist du mir ein Vorbild gewesen. Und außerdem **Conrad Schalm** für deine Segelbegeisterung und **Rika Mimura** dafür, dass du mein Japanisch am Leben erhältst.

**Anne Happe -** Dafür, dass du mir beim Spinnenbestimmen geholfen hast und für die vielen Tage danach. Du unterstützt mich in dem, was gut für mich ist, und das bedeutet mir viel.

Teile dieser Arbeit wurden bereits in der folgenden Publikation, sowie in auf verschiedenen Konferenzen in Form von Postern und Vorträgen vorgestellt:

**Publikation:**

H. Steldinger, , A. Esposito, K. Brunnengräber, J. Gläsel, B.J.M. Etzold
**Activated Carbon in the Third Dimension - 3D Printing of a Tuned Porous Carbon**
Advanced Science 2019, *1901340*, DOI: 10.1002/advs.201901340

**Präsentationen:**

H. Steldinger, J. Gläsel, B.J.M. Etzold
**Monolith from 3D Printed Open Cell Polymer Structures**
31. Deutsche Zeolith Tagung, 2018, Dresden (Germany)

H. Steldinger, J. Gläsel, B.J.M. Etzold
**Monolith from 3D Printed Open Cell Polymer Structures**
Carbon, 2018, Madrid (Spain)

H. Steldinger, J. Gläsel, B.J.M. Etzold
**Hierarchically Structured Carbons**
Frühjahrstagung 2018 des Arbeitskreis Kohlenstoffs, 2018, Wetzlar (Germany)

**Poster:**

**3D Printed Carbon with Hierarchical Pore Structure from Polymer Precursors**
52. Jahrestreffen Deutscher Katalytiker, 2019, Weimar (Germany)

**3D Printed Carbon with Hierarchical Pore Structure from Polymer Precursors**
International Conference on Micro Reaction Technology – IMRET, 2018, Kahrlsruhe (Germany)

**3D Printed Carbon with Hierarchical Pore Structure from Polymer Precursors**
Jahrestreffen Reaktionstechnik, 2018, Würzburg (Germany)

# Erklärung zur Dissertation

Hiermit versichere ich, die vorliegende Dissertation ohne Hilfe Dritter nur mit den angegebenen Quellen und Hilfsmitteln angefertigt zu haben. Alle Stellen, die aus Quellen entnommen wurden, sind als solche kenntlich gemacht. Diese Arbeit hat in gleicher oder ähnlicher Form noch keiner Prüfungsbehörde vorgelegen.

## Abstract

Due to its tunable porosity and chemical versatility, activated carbon is one of the most widespread porous materials in industry used in applications such as adsorption and catalysis. Nevertheless, commercially available activated carbons suffer from low thermal and electric conductivity in the bulk, abrasion, and undefined bed porosity, since they are provided in the form of powders, pellets, or spherical particles. These obstacles could be overcome through the free design offered by 3D printing. However, present methods for the 3D printing of carbon either lack design freedom of the printed object or fail to introduce microporosity.

In this work, a novel method for the 3D printing of carbon was developed. The method is based on lithographic 3D printing of a porous polymer, which is then transformed into activated carbon by a thermal treatment. Through the implementation of porogen templating into the printing process, meso- and macropores were introduced in the polymer precursor. In an optimized oxidation and pyrolysis procedure, the macrostructure and templated pores were retained and an additional fraction of micropores was introduced. Using $CO_2$ activation the pore size was tailored and the specific surface area and pore volume increased to $2213\,m^2g^{-1}$ and $1.68\,ml\,g^{-1}$ (QSDFT), respectively. These values are similar to those presented for activated carbons. Mechanical stability was maintained throughout the process.

Through upscaling, activated carbon open-cellular monolithic structures of 40 mm in length and 20 mm in diameter were created. In an electric swing adsorption process, they exhibited a much better thermal and electric conductivity than a carbon pellet bed. Although the pelletized carbons showed a higher adsorption capacity because of a more densely packed bed, the monoliths could be regenerated much faster, due to their continuous macrostructure.

The unique design flexibility of 3D printed carbons in combination with their top-notch porous properties will contribute to the optimization of industrial processes that rely on the use of activated carbons in the fields of adsorption, catalysis and energy application.

## Zusammenfassung

In industriellen Adsorptionsverfahren ist Aktivkohle eines der am weitesten verbreiteten porösen Materialien. Es wird kommerziell hauptsächlich in Form von Pellets, Pulvers oder Kügelchen verkauft, weist daher jedoch einige Nachteile wie schlechte elektrische und Wärmeleitfähigkeit, Abrieb und verringerten Wandschüttdichten auf. Durch 3D Druck kann die Makrostruktur frei designt werden, um diese Nachteile zu überwinden. Jedoch mangelte es bisherigen 3D Druck Verfahren für Kohlenstoffen entweder an der mechanischen Stabilität, der erforderlichen Druckgenauigkeit, sodass nur rudimentäre Strukturen erzeugt wurden, oder es konnten keine Mikroporen erzeugt werden.

In dieser Arbeit wurde eine neue Methode für den 3D Druck von Kohlenstoff auf der Basis der Umwandlung von lithographisch gedruckten porösen Polymeren entwickelt. Dafür wurde erstmals die Porogentemplierung mit der Photopolymerization in einem 3D Drucker kombiniert, um Polymere mit Meso- und Makroporen erzeugen. Durch ein optimiertes thermisches Verfahren ließen sich nicht nur die Makrostruktur und die templierten Poren erhalten, es wurde auch eine neue Fraktion von Mikroporen erzeugt. Durch $CO_2$ Aktivierung konnte die Gesamtoberfläche auf $2213\,m^2g^{-1}$ und das Porenvolumen auf $1.68\,ml\,g^{-1}$ (QSDFT) unter Erhalt der mechanischen Stabilität erhöht werden.

Nach einem Upscaling war es möglich, offenzellige Monolithe bis zu einer Länge von 40 mm und einem Durchmessen von 20 mm zu drucken. Durch ihre kontinuierliche Struktur wiesen diese im Vergleich zu einer Kohlenstoffpelletschüttung eine deutlich erhöhte Wärmeleitfähigkeit auf. Auch wenn die Monolithe durch ihren höheren Hohlraumanteil in der Makrostruktur im Vergleich zur Pelletschüttung eine geringere Gesamtadsorptionskapazität aufwiesen, konnten sie deutlich schneller und zu einem höheren Grad in der Desorption regeneriert werden.

Diese Methode des 3D Druckes von Aktivkohle ist daher geeignet, um durch ein gezieltes Design der Makrostruktur, Prozessintensivierung in den Anwendungsgebieten von Aktivkohle insbesondere bei zyklischen Adsorptionsprozessen zu erreichen.

## Clarification of terminology

In the abstract, it was already mentioned that the method presented in this work does not directly print activated carbon. Instead, a porous polymer is printed at first and then converted to activated carbon by a thermal treatment.

Many additive manufacturing processes involve multiple steps. Stereolithography usually requires post-illumination or thermal curing for final mechanical properties. Some techniques, like fused deposition modeling, utilize support structures that have to be removed. Other materials such as graphite or prominently ceramics cannot be printed directly as well [1, 2]. They often contain a binder that needs to be eliminated and the ceramic sintered after printing. Still, these methods are usually referred to as 3D printing of ceramic, etc., since it is not possible to create these structures with traditional manufacturing methods.

Also, in this work, the whole process is termed as 3D printing of carbon and the product is called 3D printed carbon.

## Contents

## Nomenclature

| Symbol | Name | Unit or value |
|---|---|---|
| $a_{SSA}$ | Specific surface area | m$^2$ g$^{-1}$ |
| $A$ | Area | m$^2$ |
| $c$ | Concentration | mol cm$^{-1}$ |
| $d$ | Diameter or thickness | m |
| $E$ | Extinction | - |
| $h$ | Height | m |
| $\Delta H_{ads}$ | Adsorption enthalpy | J mol$^{-1}$ |
| $I$ | Intensity | - |
| $m$ | Mass | g |
| $\Delta m$ | Mass difference | g |
| $M$ | Molecular mass | g mol$^{-1}$ |
| $n$ | Total number of experiments | - |
| $N_A$ | Avogadro constant | 6.022 mol$^{-1}$ |
| $p$ | Pressure | Pa |
| $R$ | Gas constant | 8.314 J mol$^{-1}$ K$^{-1}$ |
| $t$ | Time | s |
| $T$ | Temperature | °C |
| $v_{PV}$ | Specific pore volume | cm$^3$ g$^{-1}$ |
| $\Delta V$ | Volume reduction | m$^3$ |
| $w$ | Velocity | m s$^{-1}$ |
| $X$ | Conversion | - |
| $delta_{Hex,app}$ | Apparent density of hexane | g cm$^{-1}$ |
| $\epsilon$ | Molar attenuation coefficient | m$^2$ mol$^{-1}$ |
| $sigma_i$ | Standard error of the variable i | *unit of i* |

## Abbreviations

| | |
|---|---|
| ABS | Acrylnitril-sutadien-styrol-copolymer |
| AC | Activated carbon |
| ACFC | Activated carbon fiber cloth |
| BAPO | Phenylbis(2,4,6-trimethylbenzoyl)phosphine oxide |
| BeButP | Benzyl butyl phthalate |
| BET | Brunaer-Emmet-Teller |
| Bis-GMA | Bisphenol A-glycidyl methacrylat |
| CAD | Computer automated design |
| CDC | Carbide derived carbon |
| CDLP | Continuous digital light projection |
| CLIP | Continuous liquid interface production |

| | |
|---|---|
| CMC | Carboxymethyl cellolose |
| CTAB | Cetyltrimethylammonium bromide |
| CVD | Chemical vapor deposition |
| CVDE | 1,4-Cyclohexanedimethanol divinyl ether |
| DButP | Dibutyl phthalate |
| DCPDA | Dicyclopentadienyl diacrylate |
| DCyP | Dicylclohexyl phthalate |
| DED | Direct energy deposition |
| DEP | Diethyl phthalate |
| DGEBA | Bisphenol-A-diglycidylether |
| DIP | Diisodecyl phthalate |
| DLP | Digital light processing |
| DMD | Direct material deposition |
| DMLS | Direct metal laser sintering |
| DOctP | Dioctyl phthalate |
| DSC | Differential scanning calorimetry |
| DVB | Divinyl benzene |
| EBAN | Electron beam additive manufacturing |
| EBM | Electron beam melting |
| ECC | 3,4-Epoxycyclohexylmethyl-3’,4’-epoxycyclohexane carboxylate |
| e.g. | exempli gratia |
| ESA | Electric swing adsorption |
| FDM | Fused deposition modeling |
| FFE | Fused filament extrusion |
| GNP | Graphene nanoplatelets |
| GO | Graphene oxide |
| Hex | Hexane |
| HPHg lamp | High pressure mercury lamp |
| i.e. | id est |
| IR | Infrared |
| IUPAC | International Union of Pure and Applied Chemistry |
| LCD | Liquid crystal display |
| LENS | Laser engineered net shape |
| MCM | Mobil Composition of Matter (mesoporous silica material) |
| NIR | Near infrared |
| OCS | Open-cell structure |
| OMC | Ordered mesoporous carbon |
| PAN | Polyacrylonitrile |
| PBF | Powder bed fusion |
| PE | Polyethylene |
| PEEK | Polyetheretherketon |

| | |
|---|---|
| PEGDA | Polyethylene glycole diacrylate |
| PEO | Poly(ethylene oxide) |
| PET | Polyethylenterephthalat |
| PETA | Pentaerythritol tetraacrylate |
| PIPS | Polymerization induced phase separation |
| PLA | Poly(lactic acid) |
| PPO | Poly(propylene oxide) |
| PSA | Pressure swing adsorption |
| QSDFT | Quenched solid state functional theory |
| SBA | Santa Barbara Amorphous type (mesoporous silica material) |
| SEM | Scanning electron microscope |
| SLA | Stereolithography |
| SLS | Selective laser sintering |
| SSA | Specific surface area |
| STP | Standard conditions for temperature and pressure |
| TCD | Thermal conductivity detector |
| TG | Thermogravimetry |
| TPO | Temperature programmed oxidation |
| TTT | 1,3,5-triallyl-1,3,5-triazine-2,4,6(1H,3H,5H)-trione |
| TTVE | Trimethyloylpropane trivinyl ether |
| UK | United Kingdom |
| UV | Ultraviolet |
| VdW | Van der Waals |
| Vis | Visible (blue to red light spectrum) |
| VOC | Volatile organic compound |

## 1 Introduction

Activated carbon (AC) is an amorphous, carbonaceous and highly porous solid substance that combines essential features, which enable a large variety of applications in industry and daily life: Due to its tunable porosity, AC can be tailored in terms of specific surface area (SSA), pore volume and pore size for pore confinement of catalyst particles, better adsorption capacity or higher speed of diffusion of a liquid or gaseous species. Through carbon chemistry, the surface can be modified, e.g., by the introduction of acidic or basic functional groups for catalysis or selective adsorption, as in the separation of $CO_2$ from $CH_4$ or $N_2$ [3]. Activated carbons are also chemically resistant against non-oxidizing acids and exhibit temperature and pressure stability in non-oxidizing conditions. Traditionally, activated carbons have been produced from a wide range of feedstocks: such feedstocks include biomaterials, polymers, or carbides, that in turn yield powders, pellets, or spheres. Although the carbon material itself is electrically and thermally conductive on the micro-scale, it lacks these attributes on the macro-scale owing to poor interconnectivity of single particles. Additionally, dust formation due to abrasion and large pressure drops have to be accounted for in the application.

To tackle this challenge, honeycomb monoliths have been produced through the extrusion of activated carbon powders and a binder [4]. Due to their continuous structure, honeycomb monoliths exhibit a better conductivity and a smaller pressure drop than particle beds. However, this manufacturing method yields only tubular structures, which limits the field of application.

The widespread advances in 3D printing have opened the possibility for the manufacture of more sophisticated geometries including open-cellular structures (OCS). Using these methods, it is possible to tailor the monolith shape for various purposes and optimize fluid mixing, yield a small pressure drop or create advanced reactor geometries [5]. To date, multiple methods of 3D printing of carbon materials have been tested. However, these technologies are still limited by simple geometries or a focus on graphene-based or other non-porous materials. In short, a 3D printing method that combines a high specific surface area, a tunable pore structure, mechanical stability and a high degree of design freedom has not yet been reported.

An instructive example for the application of 3D printed structured AC is the adsorption of volatile organic compounds (VOC) in electric swing adsorption (ESA). ESA is a particular form of cyclic temperature swing adsorption in which an increased temperature regenerates the adsorbate when it reaches full adsorption capacity. It uses electric resistive heating to introduce the energy in the carbon adsorbent rather than hot nitrogen gas or water vapor as for traditional temperature swing adsorption. Thus, ESA avoids the disadvantage of dilution in the sweep gas due to the low heat capacity of nitrogen, or water impurities in the recycled product. Instead, the energy input is independent of the gas influx. This allows for a higher adsorbate concentration and quicker desorption. Since it does not benefit from waste heat or steam, this method is an excellent alternative for smaller and independent units that cannot rely on the waste heat from other processes. Although ESA is feasible with activated carbon pellets, inhomogeneous temperature distribution can result, which is why it profits from high thermal and electric conductivity. Therefore, activated carbon monoliths were proposed as a promising alternative to traditional materials. However, to ensure optimal adsorption properties it is crucial to finely control the activated carbon properties at various scales.

# 2 State of the Art

In the following, the state of the art and theoretical background of 3D printed carbon adsorbers will be presented. The focus will be set on unique features of electric swing adsorption processes, templating mechanisms for carbon materials and the means of producing carbon materials by additive manufacturing.

## 2.1 Separation of gaseous compounds by adsorption

Adsorption describes a process in which gas molecules, the adsorptive agent or species, are bound to the surface of a solid material, the adsorbent. The adsorbed molecule is called adsorbate. The reverse process, which is the release of a gaseous component, is called desorption [6]. Figure 2.1 depicts the nomenclature.

When the adsorptive agent approaches the adsorbent, Van der Waals (VdW) interactions take place. The heat released in this exothermic process is called the heat of adsorption. Adsorption processes can be subdivided into two categories. If the adsorpt is bound by VdW forces, the process is called physisorption. If subsequently, a chemical bond establishes between the adsorbate and the adsorbent, it is called chemisorption. In contrast to physisorption, a larger heat of adsorption is typical for chemisorption.

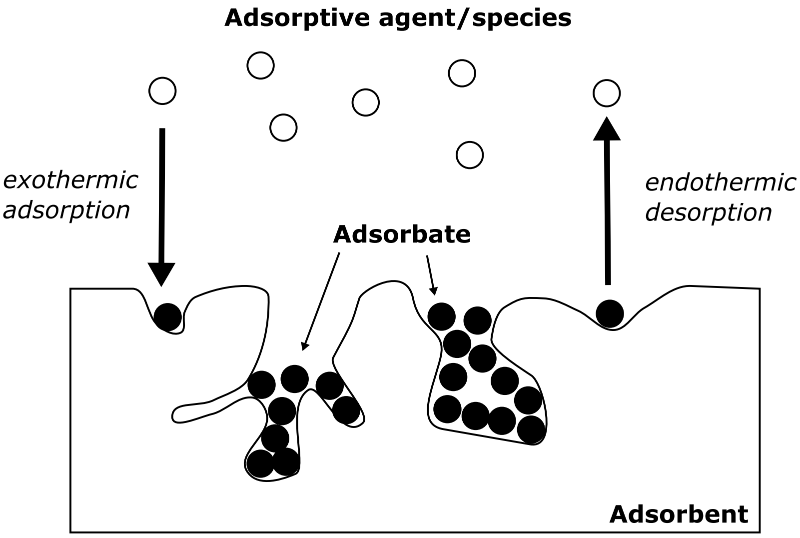

**Figure 2.1:** Scheme of adsorption and definition of terminology.

As adsorption processes take place on the surface of solid materials, a large specific surface area is of immanent importance for the creation of high-performance adsorbents. A wide range of porous materials, e.g., activated carbon, zeolites, metal-organic frameworks or porous polymers, are used in adsorption processes. However, pores do not only increase the SSA and thus the area at which they store the adsorbates. Furthermore, in narrow pores with a diameter similar to the size of the adsorptive molecule, the adsorbate establishes a stronger bond due to overlapping interaction with all pore walls. Thus, if the size of the adsorbate fits the pores, even substances with a high vapor pressure can be adsorbed [7]. The International Union of Pure and Applied Chemistry (IUPAC) divides pores into three categories, as shown in Table 2.1.

**Table 2.1:** IUPAC classification of pore sizes in porous materials [8].

| Naming | Pore size | Comments |
|---|---|---|
| Micropores | $< 2\,\mathrm{nm}$ | Only monolayer of the adsorbate |
| Mesopores | 2 to 50 nm | Pore condensation, adsorption-desorption hysteresis observed |
| Macropores | $> 50\,\mathrm{nm}$ | No hysteresis |

Porous materials do not only differ in terms of pore shapes and sizes but also their chemical makeup and surface functionalities. In combination with the adsorptive's chemical structure, all of these factors impact VdW interactions and, therefore, the heat of adsorption and vapor pressure of the adsorbate. Thus, a highly polar adsorbent surface can cause strong interactions with a likewise polar adsorptive species creating the same effect as small pores would do, they increase the heat of adsorption.

In analogy to condensation and evaporation, the vapor pressure of a substance describes the proportion of free to adsorbed gas molecules. However, the vapor pressure can change depending on adsorbent and temperature. The Clausius-Clapeyron equation expresses this relationship:

$$\frac{1}{p}dp = \frac{\Delta H_{ads}}{RT^2}dT \tag{2.1}$$

This equation describes the impact of the temperature change ($dT$) on the change in vapor pressure ($dp$). In the case of high heat of adsorption ($\Delta H_{ads}$), like for organic vapors on activated carbons, the temperature change has a tremendous impact. In the case of a small heat of adsorption, like for $CO_2$ on activated carbon, the vapor pressure cannot be impacted as much by a change in temperature.

### 2.1.1 Comparison of swing adsorption techniques

On the one hand, disposable adsorbents can be used in industrial processes in order to comply with emission guidelines. Biogenic activated carbons, for example, are commonly utilized for separating organic vapors from exhaust gases and are subsequently burned when they reach full capacity. On the other hand, regeneration of the adsorbent and recovery of the adsorped species can be financially beneficial, since the adsorbent and the adsorbate can be reused. In other applications, the adsorbate is the desired product, as for $CO_2$ capture from air. In all of these cases, swing adsorption processes are used [9]. Then, regeneration follows when it reaches full adsorption capacity or a critical outlet concentration. Therefore, two to three adsorbers are used parallelly. In this setup, some of the adsorbers undergo desorption, while the others can be used for adsorption.
There are two major types, namely temperature and pressure swing adsorption, which are both used in the industry. Figure 2.2 illustrates their operation.

#### Pressure swing adsorption

Pressure swing adsorption (PSA) processes are used mainly for weakly adsorbing species. High overall pressure during adsorption increases the partial pressure and compensates the low affinity of the

adsorptive species to the adsorbent, which is why the heat of adsorption is usually small. Therefore, a temperature increase would not impact the vapor pressure of the adsorbate much. Instead, after reaching full capacity, the pressure is reduced and the adsorbed species released into the gas phase. In addition, inert gas flushes the adsorbent bed for further desorption. PSA is commonly employed for the separation of $CO_2$ in the process of natural gas reforming [10], biogas production [11] or coal gasification [12].
A particular case of PSA is vacuum swing adsorption, in which the pressure is decreased below 1 bar for the desorption. This method is used alternatively to temperature swing adsorption if one of the species is temperature-sensitive or to clean the adsorption column if high purity is needed. Thus, vacuum swing adsorption has been proposed as an alternative to distillation in propylene/propane separation [13]. In general, compression and the creation of a vacuum, in particular, require electric energy, which makes pressure swing adsorption expensive to operate. It is therefore employed in case of a high concentration of the adsorptive agent in the feed.

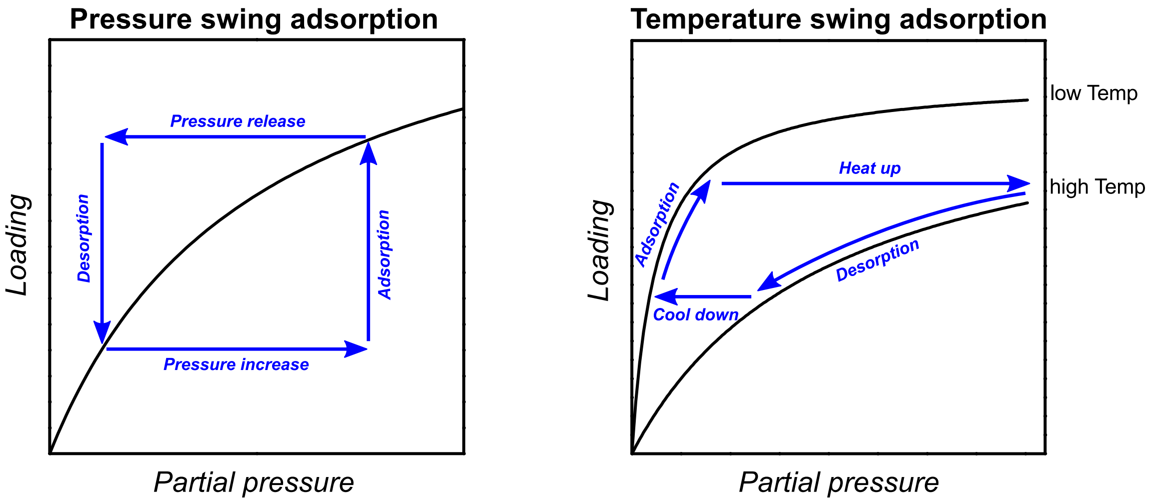

**Figure 2.2:** Vapor pressure and loading of a solid substrate over the course of a full cycle in a pressure and temperature swing adsorption process.

### Temperature swing adsorption

In contrast to PSA, the temperature swing adsorption (TSA) utilizes elevation of temperature to increase the vapor pressure of the adsorbed species and thus the driving force for the desorption. The adsorption takes place at ambient pressure due to the low vapor pressures of the adsorptive. Adsorbents, which are suitable for TSA, exhibit a large heat of adsorption. Therefore, a small temperature increase causes a substantial increase in vapor pressure, as described in Equation 2.1. As an alternative to PSA, adsorption of $CO_2$ can also be facilitated using a temperature swing adsorption process. Then the carbon adsorbent needs to contain many surface functionalities like alkaline amine or other nitrogen sites to increase the heat of adsorption [14, 15]. These significantly increase binding forces of the adsorbent to $CO_2$, which enables adsorption at ambient pressure. In order to carry out desorption, the temperature has to reach values around 100 to 200 °C [14, 16].
Another widespread use case of TSA is the adsorption of volatile organic compounds. Many solvents such as dichloromethane, diethyl ether, hexane or toluene have to be recovered from the exhaust air before

the release into the atmosphere [17, 18]. In contrast to other techniques of solvent removal such as PSA, catalytic combustion, condensation or membrane separation, TSA requires energy only for the regeneration and not the adsorption [19]. Thus, TSA is most suited for small concentrations of the adsorptive species.

Traditionally, there are two methods for introducing heat to increase the temperature for adsorption. Firstly, the adsorber can be heated through the reactor walls. Secondly, the inlet gas stream can be warmed prior to the inlet, which requires either hot inert gas or steam. However, all methods have a series of shortcomings, amplified by the vast amounts of heat necessary due to the high heat of adsorption typical for TSA. Firstly, the heat conductivity of the commonly used granular adsorbent is relatively small. Secondly, the heat capacity of nitrogen is small. If alternatively steam is used, pores of the adsorbent can be blocked and the desorbed stream is contaminated with water.

In order to increase the performance of TSA processes, new methods for heating the adsorbate were investigated. These are direct electrical heating [20], induction heating [21, 22] and microwave heating [23, 24]. Microwave and induced heating inhere the limitation of inhomogeneity, as their intensity declines from the outside to the center of the adsorption column. Direct resistive heating requires a partly conductive substrate. In contrast to microwave or induced heating, the adsorbent homogeneously heats up if its resistivity is homogeneous as well. In the past, electrical heating was seen as a disadvantage. In the course of electrification of industry for use of sustainable electric power, the possibility of electrical heating can be an advantage.

### 2.1.2 Electric swing adsorption

A TSA process, in which the Joule effect provides the energy for the desorption, is called electric swing adsorption (ESA). The Joule effect, also called Joule, Ohmic or resistive heating, describes the loss of electric power owing to the resistance of a conductive material. Compared to traditional TSA processes, ESA has several advantages:

- Heat energy is directly provided at the adsorbent without the limitations of heat transfer between heat source and adsorbent.
- Heating is provided throughout the adsorbent bed homogeneously in case of uniform resistivity.
- The heating rate is decoupled from the heat capacity and the amount of carrier gas, and thus, high heating rates can be realized.
- Higher concentrations of the adsorbate are reached through these high degrees of freedom.

This method of resistive heating in adsorption columns was patented in 1971 already [25]. It describes an apparatus and process for desorption of particulate carbon beds with the use of electric heating. Due to its sufficient conductivity, tunable sorption capacity and excellent commercial availability, activated carbon has been widely studied as an adsorbent in electric swing adsorption in the form of traditional shapes, e.g., powder, beads or pellet [26, 27, 28, 29]. Throughout technical adsorption, often particulate adsorbents are used since they are easy to handle and widely commercially available. Nevertheless, in the application, they suffer from a series of drawbacks, such as bad thermal and electric conductivity, decreased bed density at the reactor wall, high pressure drop and attrition. Electric current

can only flow through tiny interconnections at the point of contact of individual particles. This limitation can result in an inhomogeneity in resistivity and temperature profile during the desorption. When using particulate carbons, the pressure of the bed compression is crucial for its resistivity [28].
In adsorption and ESA in particular, also other carbon adsorbent morphologies have been used, e.g., activated carbon fibers [30, 31], activated honeycomb monoliths [32, 33, 34], and 3D printed monoliths [35].

### Electric swing adsorption in VOC & $CO_2$ removal

Removal of volatile organic compounds from off-gas streams has become an increasingly important issue as environmental restrictions tighten and measures are taken against global warming and ozone layer destruction. Organic vapors and volatile fluorinated or chlorinated compounds have multiple greenhouse potential compared to $CO_2$. Chlorinated solvents that are not restricted by the Montreal Protocol due to their short-lived nature and low ozone diminishing effect can still have a detrimental potential on the ozone layer if their concentration keeps rising. Thus, the removal of volatile organic compounds has been a significant focus in research and application of electric swing adsorption.

VOC removal by ESA has employed activated carbon for several organic substances with a low boiling point like methyl bromide [29] or isobutane [36] or solvents with high boiling point such as toluene [37] or methyl propyl ketone [30]. The research proved that the organic vapors could be obtained in high concentrations upon desorption [37].
In the case of a low boiling point, cryogenic condensation is crucial for sufficient recovery. These systems work very inefficiently if vapor concentrations are low since the carrier gas is cooled down as well [30, 36]. However, in combination with ESA, the VOC partial pressure can be increased, while the flow rate of carrier gas is decreased since the energy input is independent of its flow.

The most widely studied adsorbent for ESA is activated carbon fiber cloth (ACFC). It is industrially produced in large quantities at high purity in a standardized way and thus widely available with different features. Subrenat et al. [38, 39] examined the temperature distribution of ACFC in air when affixed in two copper clamps. The non-activated fiber cloth with a dimension of 15 x 25 cm in between exhibited a uniform temperature distribution when heated up to 100 °C. The activated sample, however, could not be evenly heated up because of inhomogeneities in its degree of activation. At places with low specific surface area ($1100\,m^2g^{-1}$) it remained colder, while at spots with high SSA ($1500\,m^2g^{-1}$) it became hotter due to a variation in the carbon density and conductivity. Besides, they found that the specific resistivity was increased by activation compared to the pristine carbon fiber cloth. Furthermore, activation with $H_2O$ vapor at 850 °C led to a stronger increase in the resistivity than activation using $CO_2$ despite similar specific weights of the carbon. They explained the difference through a higher degree of oxygen functionalities in the $CO_2$ activated carbon.
Synder and Leesch [29] examined the cyclic behavior by employing coconut-derived carbon for the adsorption of methyl bromide in an ESA process. Throughout 12 cycles, they found a 97 - 100 % retention of the adsorption capacity.
The industrial use of ESA was proven by Subrenat et al. [40]. They installed a system of two activated carbon fiber cloth adsorbers in a plant for the adsorption of methylene chloride from the off-gas, as

shown in Figure 2.3. Each of the adsorbers contained 1.6 kg of the activated fiber with a specific pore volume of 0.435 ml $g^{-1}$ and a specific surface area of 873 $m^2 g^{-1}$. The adsorbers were used alternatingly in an adsorption-desorption cycle with downstream cryogenic condensation and recycling of the solvent. In the 24/7 operation, the system handled a flow of 100 $m^3 h^{-1}$ loaded with 100 to 700 g $m^{-3}$ of methylene chloride. In operation, the outlet flow of the VOC was lowered to 15 g $h^{-1}$ well below the regulatory value of a maximum of 100 g $h^{-1}$.

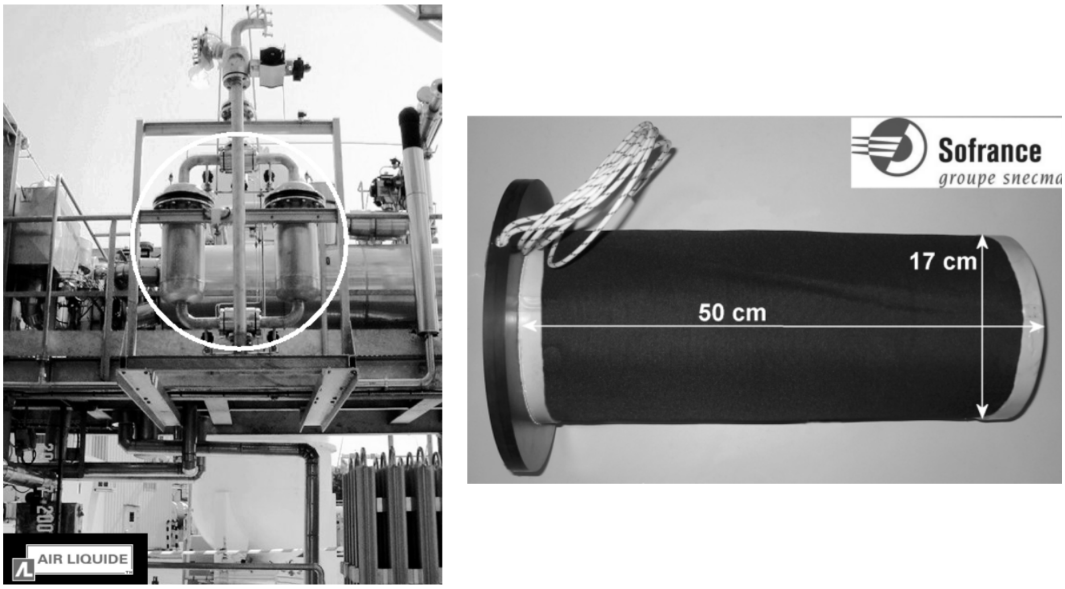

**Figure 2.3:** Industrial implementation of an electric swing adsorption process; left: two ESA adsorption units; right: activated carbon fiber cloth adsorber unit with electrodes (white). Reprinted with permission of [40].

On the one hand, activated carbon fiber cloths are industrially manufactured and electrically conductive owing to their continuous structure. On the other hand, the means of their macroscopic arrangement is limited, which leads to a non-optimal distribution of airflow and electric current.
In contrast, the shape of monolithic adsorbers can be designed more freely, allowing for high control of the macrostructure. Their shape can be tailored for low pressure drop or high adsorption capacity. Traditionally, honeycomb monoliths have been produced out of many materials such as zeolite or activated carbon and tested in adsorption. Honeycomb structures are usually manufactured by extrusion of the active material with a binder [41].

Lee et al. [32] separated $CO_2$ from indoor air at a concentration of 3000 ppm using a commercially manufactured activated carbon monolith from Carbotech. The $CO_2$ concentration was lowered to 2756 ppm, which is a 8.1 % reduction. The regeneration was conducted by resistive heating with maximum concentrations of 11000 ppm at a temperature of 60 °C. Although the activated carbon was not characterized in terms of porosity or $CO_2$ capacity, it can be suspected to be rather low in contrast to amine functionalized carbons that adsorb $CO_2$ also at lower concentrations [42]. In case of a low capacity, the carbon material needs to be regenerated more often. Thus, in the publication from Lee et al., the energy requirement amounted to 57.8 kJ per cubic meter of air. 64 % of the heat was spent to increase the temperature of the adsorbent alone. Since, the electric energy used for the regeneration is more expensive than steam, at least in an industrial environment, the amount of cycles needs to be reduced as

much as possible to reduce the costs of operation. This can be achieved by tailoring the carbon materials to their purpose in adsorption.
Yu et al. [43, 33] utilized a carbon honeycomb monolith for the separation of $5\,\mathrm{g\,m^{-3}}$ toluene from nitrogen gas. In the desorption, which employed resistive heating up to a temperature of 200 °C, a high toluene concentration of $250\,\mathrm{g\,m^{-3}}$ was reached.
Ribeiro et al. [44] prepared a hybrid adsorbent by filling the channels of a commercial activated carbon honeycomb monolith (Mast Carbon, UK) with zeolite 13X. While the zeolite showed a high capacity for $CO_2$ adsorption, the continuous carbon monolith was used for resistive heating. Thus, they were able to concentrate the $CO_2$ from 7.6 % by a factor of 6 to 46.6 % while capturing 81.4 % of the $CO_2$. It was proposed that a higher purity requires a higher zeolite content.
Zhao et al. [45] compared an activated carbon monolith (Mast Carbon, UK) with the zeolite 13X (18 wt%) or NaUSY (70 wt%) as additional filler in terms of their performance in an ESA process. The zeolite additives, and the NaUSY, in particular, due to its higher mass content, significantly improved the sorption capacity of the adsorbent. Therefore, the energy usage for the separation of $CO_2$ was considered to be much more efficient.

The literature review shows that the research of electric swing adsorption processes has been focused mainly on applying industrially available materials like carbon fibers or honeycomb monoliths. Due to a lack of suitable porous properties for adsorption of $CO_2$, zeolites were employed to enhance the uptake. Although zeolites might be suitable for $CO_2$ adsorption in dry environments, they are not applicable for organic vapors.

## 2.2 Porous carbons

Porous carbons are a class of porous materials with unique properties. Consisting of an amorphous carbon framework, they are produced from a wide variety of organic (e.g., coal, straw, wood, kraft lignin, Polystyrene or cigarette buds) or inorganic materials (e.g., TiC, SiC). Their unique porous properties that can be tailored in terms of pores size and specific surface area makes activated carbon suitable for many applications in catalysis and adsorption. Activated carbons also exhibit high thermal and chemical stability. Its organic carbon framework allows for functionalization of the surface with, e.g., oxygen, sulfur, phosphorus or nitrogen-containing groups.

### 2.2.1 Types of activated carbon

Porous carbons are industrially produced from a wide variety of feedstocks. The most common type is **bioderived activated carbon**. Biogenic sources include organic resources like wood, straw or cellulose, but also waste materials like coconut shells, stones of fruits, kraft lignin, cigarette buds or sewage sludge. The upgrading of waste streams into the valuable product activated carbon is an alternative to the usage of first-generation biomass. In the categorization of natural raw materials in terms of the H/C and O/C ratio, these materials are located in the top right corner due to their large amount of oxygen functionalities and high water content (see Figure 2.4). Therefore, during processing, large amounts of heat are

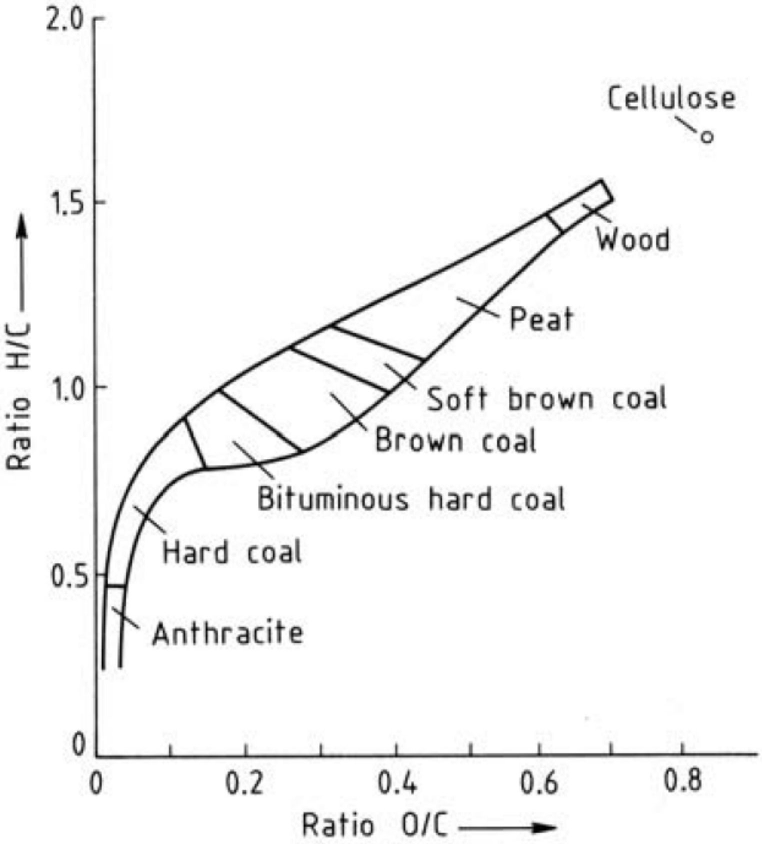

**Figure 2.4:** Categorization of natural raw materials in terms of H/C and O/C ratio. Reprinted with permission of [46].

needed to evaporate residual water. Furthermore, a significant amount of carbon in the feedstock is usually volatilized in the form of $CO_2$.
Alternatively, also brown or hard coal can be used as feedstock. These materials underwent a natural carbonization process and are less functionalized as a consequence. Therefore, upon further pyrolysis and activation, a lower percentage is volatilized into the atmosphere [47].
In general, activated carbon from biomaterials is inexpensive and thus widely used in the industry. However, this origin inheres also disadvantages. Plants contain many inorganic substances, e.g., phosphates, sulfates, sodium or potassium. These are non-volatile and although they occur in low concentrations in living matter, their content increases up to 20 % of the carbon material due to the usually high mass losses. The amount of these residuals is called ash content. After carbonization, if accessible, these ashes can be dissolved by acids depending on the use case [48].
Moreover, biomaterials are usually inhomogeneous in terms of their water content. Its distribution can be utilized in order to create a hierarchical carbon material [49], but it also leads to a non-homogeneous distribution of the carbon's properties. Furthermore, these parameters change from year to year as the growing conditions are dependent on weather.

Another method is the production of **carbide-derived carbons** (CDC). In this process, the metal atoms of a carbide are reactively extracted by halides, e.g., chlorine at temperatures of 300 to 1900 °C [50] in a gas phase process. In a typical example (see Equation 2.2), chlorine reacts with the titanium from titanium carbide to form titanium tetrachloride, which is gaseous at reaction conditions and can be separated from the residual chlorine downstream.

$$2Cl_2 + TiC \longrightarrow TiCl_4(\uparrow) + C \tag{2.2}$$

In contrast to bioderived activated carbons, which are produced in a kinetically controlled process, meaning their properties depend on heating ramps, etc., the properties of CDCs mainly depend on the synthesis temperature. During the reaction, carbon atoms liberated from the metal binding partner, establish new bonds with surrounding carbon atoms. With higher temperatures, the carbon lattice becomes more graphitic and the pore sizes increase. Since it is a thermodynamically controlled process, carbons with a more controlled pore size and even core-shell particles can be produced by this method [51]. Although CDCs can exhibit high specific surface areas without any post-treatment, pore-clogging can occur at low production temperatures due to the presence of high boiling compounds. In these cases, activation can increase the porosity further [52, 53].
In carbides, the only relevant impurities are other metal atoms such as iron, which can is contained in a substantial amount in titanium carbide. However, all metals that form chlorides are extracted from the carbide, which is why CDCs have negligible ash content. Due to the absence of oxygen during the production, they also exhibit low amounts of oxygen surface groups if not functionalized [54].

The third commercial process is the production of **polymer-derived activated carbons**. Since the composition of the polymer precursor is designed in manufacturing, the carbon properties can be controlled as well. In contrast to bioderived carbons, they contain little to no ash. Furthermore, there are few deviations in the precursor materials and thus a more constant product properties. Also, polymer derived carbons can be designed in a way to retain the polymer structure. Since the precursor is usually uniform, the carbon particles exhibit a high uniformity without structural defects, which results in exceptional crushing strength.

Processes for the production divide into two groups: i) direct pyrolysis of highly crosslinked polymers; ii) curing and pyrolysis of little to not crosslinked polymers.

Direct pyrolysis can be conducted exclusively if the polymer precursor exhibits a high degree of crosslinking. These are usually phenoplasts like resols, benzoxazines or otherwise cured novolac polymers. Upon pyrolysis, these precursors retain their shape when transformed into carbon [55, 56]. Additional crosslinking of the polymer structure is facilitated by reactive groups inside the polymer as in the case of resol (hydroxymethylene) or by thermal decomposition of functional groups and the creation of radicals, therefore. These processes suppresses depolymerization and less polymer building blocks leave through the gas phase [57]. After pyrolysis, specific surface areas up to 1500 $m^2g^{-1}$ [58] but more commonly in the range of 500 to 1000 $m^2g^{-1}$ [59] are observed.

In contrast to these highly crosslinked polymers, pyrolysis of thermoplastics and even some duroplasts results in depolymerization, the release of monomers and thus a high mass loss. Furthermore, their macrostructure lacks stability. These polymers are not sufficiently crosslinked or self-curing and need to be pretreated before pyrolysis. In literature, numerous methods can be found, e.g., oxidation in air, sulfonation with sulfuric acid, vulcanization with sulfur or hypercrosslinking via Friedel–Crafts reaction. This crosslinking is also called stabilization.

Sulfonation of poly(styrene-divinylbenzene) copolymers can be facilitated via electrophilic substitution of the benzene ring and was used as a pretreatment for pyrolysis in a number of publications. The reaction is carried out in the liquid phase using concentrated sulfuric acid [60, 61, 62], fuming sulfuric acid [63], gaseous $SO_3$ [64], chlorosulfonic acid [65] or acetyl sulfate [66, 62]. Upon subsequent pyrolysis, the sulfonic acid groups decompose at a temperature of 200 to 300 °C. They are either liberated into the gas phase as $SO_2$ and $H_2O$ or form sulfonyl bridges in the polymer framework. With further heating to 300 to 400 °C, reduction to sulfide bridges takes place. Importantly, these crosslinking reactions take place before polymer decomposition at 400 °C, thus reducing the mass loss in the pyrolysis [57]. Polymer beads used for the sulfonation are commonly below 1 mm in size and macroporous. The reason for that is the diffusion limitation of the sulfonation agents in the non-polar polymer. Since the diffusion of sulfonic acid is increased by sulfonation of the polymer, the reaction follows a shrinking core mechanism resulting in an uneven degree of functionalization [67]. Furthermore, swelling can damage the macrostructure [66].

Instead of sulfonyl, also carbon crosslinks can be introduced via Friedel–Crafts reactions. These stabilized polymers are called hypercrosslinked. Woodward et al. [68] studied the effect of hypercrosslinking as a stabilization method on the microporosity and carbon yield after pyrolysis. They carried out the reaction by swelling a macroporous styrene-divinylbenzene copolymer (2 g) in 1,2-dichloroethane (80 ml). Under argon, the crosslinking agent dimethoxymethane (6.92 ml) and subsequently $FeCl_3$ (12.44 g) as catalyst were added. The reaction was conducted for 24 hours at 75 °C. After the pyrolysis of the hypercrosslinked polymers, they achieved a carbon yield of 29 to 44 %. The yield increased with decreasing divinylbenzene (DVB) content, contrary to the specific surface area, which peaked at 417 $m^2g^{-1}$ for 100 % DVB.

Hypercrosslinking is a very resource-intensive method. In contrast, oxidation of the polymer under air is more facile to conduct. Li et al. [69] examined air oxidation as a pretreatment to increase carbon yield. In the study, the oxidation time of styrene-divinylbenzene copolymer (50:50%) beads of 640 $\mu$m size was varied from 0 to 4 hours. Despite the small mass loss of 5 % over 4 hours, the carbon yield in subsequent pyrolysis at 950 °C increased from 13 wt% for the non-oxidized to 41 wt% for the 4 hours oxidized sample. After pyrolysis, a specific surface area of 110 $m^2g^{-1}$ was achieved. $CO_2$ activation further increased this value to 778 $m^2g^{-1}$ at a burn-off of 46.8 %.

Oxidation of polyacrylonitrile (PAN) is another often used stabilization method. PAN is a thermoplastic polymer. At a temperature of 200 to 300 °C, the nitrile group is oxidized in air and undergoes cyclization in a series of reactions. Malik et al. [70] utilized oxidation for stabilizing acrylonitrile-divinylbenzene copolymer beads. The polymerization was conducted in the presence of a 1:9 mixture of nonane and toluene as the diluent in the organic phase of the emulsion polymerization. The acrylonitrile content was increased from 30 to 70 wt%, while the oxidation was carried out at a temperature of 250, 300 or 350 °C. The carbon yield of the pristine polymer was only 10 %, whereas it was raised to 30 to 50 % depending on the oxidation temperature. The highest specific surface area was achieved employing oxidation at 350 °C and using a large amount of diluent, so the high porosity in the polymer can facilitate diffusion of the oxygen.

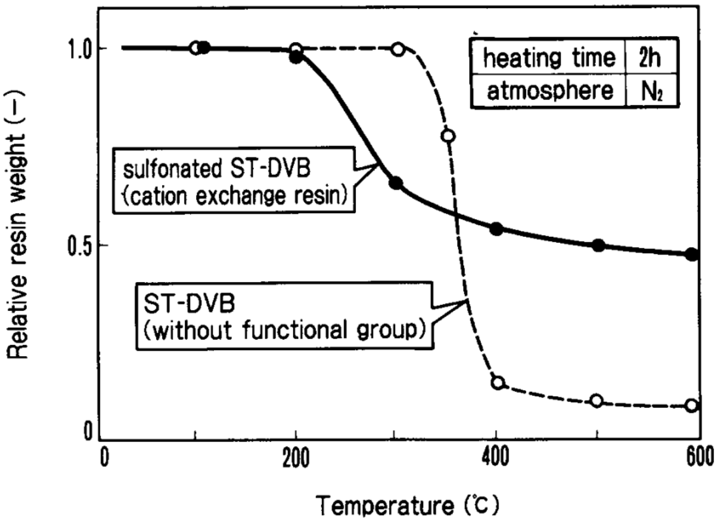

**Figure 2.5:** Influence of the functional sulfonic group on styrene-divinylbenzene copolymer pyrolysis. Reprinted with permission of [57].

### 2.2.2 Activation methods for the development of micropores

In adsorption and catalysis, the pore size distribution and pore morphology are crucial for the performance. As the pore diameter decreases towards the size of the adsorptive species, the adsorption enthalpy increases and the vapor pressure is reduced. Thus, organic substances can be separated from air by porous carbons, as they contain micropores. However, the diffusion coefficient decreases drastically with smaller pores. If the pore size is similar to the diameter of the gaseous or liquid species, surface diffusion takes place which drastically lowers the rate [73]. Thus, substances with different kinetic diameters can be separated by their speed of diffusion in the porous solid. In this way, undesired side products of chemical reactions within a porous media can be retained [74]. Furthermore, metal nanoparticles utilized in catalysis can be confined within the pores. Thus, their size can be controlled and stabilized throughout the application [75]. These examples illustrate the importance of pore size control and the increase in the specific surface area of porous carbons.

The methods subdivide into physical and chemical activation. Physical activation describes a reaction with oxidants such as $CO_2$ [76, 77], $H_2O$ [78, 79] or air [80] at elevated temperatures in the gas phase. During this process, the carbon partly gasifies, increasing the specific pore volume and pore size [81]. Carbon consists of areas with a different degree of reactivity originating from the composition of the precursor material or the pore size. Thus, the activation opens clogged or creates new pores. With a higher degree of activation, which refers to the mass loss of the carbon during the reaction, pores sizes increases and the pore size distribution generally broadens.

The activation method also impacts the surface chemistry of the carbon. Oxidation in air is conducted at a temperature of 250 to 400 °C. In this range, many functional groups like lactones, ethers and phenols are stable on the carbon surface and do not decompose during this process [82]. Therefore, the carbon surface remains highly polar and contains many oxygen functionalities. In contrast, $CO_2$ and $H_2O$ activation is conducted at 750 to 850 °C ($H_2O$) or 750 to 900 °C ($CO_2$). It is believed that only carbonyls are stable at these high temperatures, while other oxygen functional groups decompose [82]. Therefore, $CO_2$ or $H_2O$ activated carbons contain little oxygen groups and have a less polar surface.

In chemical activation methods, liquid or solid agents are used during or after the pyrolysis. In the case of the simultaneous method, the raw material is firstly impregnated by the activation agent, which can be a base, acid or salt, e.g., KOH [83], $H_3PO_4$ [84, 85] or $ZnCl_2$ [86, 87, 88]. Then the sample is heated up to a temperature of 550 to 900 °C for carbonization.

Many substances, such as KOH, function as oxidants. In a series of individual reactions, the KOH oxidizes the carbon to potassium carbonate starting at 400 °C (see Equation 2.3), which later decomposes into $K_2O$ and $CO_2$ at temperatures higher than 700 °C (see Equation 2.4). The potassium oxide also further etches into the carbon material as shown in Equation 2.5. This method is an excellent example that during chemical activation, additionally physical activation by water or $CO_2$, which are released in the processes, takes place.

$$6KOH + 2C \longrightarrow 2K + 3H_2 + 2K_2CO_3 \tag{2.3}$$

$$K_2CO_3 \longrightarrow K_2O + CO_2 \tag{2.4}$$

$$C + K_2O_2 \longrightarrow 2K + CO \tag{2.5}$$

Zinc chloride and phosphoric acid dehydrate the precursor framework and facilitate crosslinking reactions at lower temperatures than decomposition and thus increase the carbon yield [88]. It is also believed that $H_3PO_4$ forms durable phosphocarbonaceous esters at low temperatures. These condensates stabilize the carbon framework and inhibit the formation of spacious polyaromatic structures. Since they start to decompose at 430 °C, phosphoric acid activated carbons are usually produced at a low temperature of 400 - 500 °C [84, 85]. In addition, the physical stabilization effect prevents the size reduction of the carbonaceous material by polyphosphate bridges in the pores [81].

In summary, the processes involved in chemical activation are usually employed for the transformation of biomass precursors. Depending on the activation method, manifold processes take place like physical stabilization, oxidation, dissolution and precipitation. In contrast to that, physical activation is a post-treatment after pyrolysis that employs only oxidation of the carbon framework. Since chemical activation is facilitated at a lower temperature, depending on the method, the activated carbon contains more and a wider variety of oxygen surface groups and is, therefore, more polar than physically activated carbons.

### 2.2.3 Templating methods for the introduction of pores into carbon

Micropores are crucial for achieving high specific surface area carbons. However, their small diameter limits pore diffusion, since it is in the range of the kinetic diameter of gases such as nitrogen or $CO_2$. Bioderived carbons often incorporate meso- or macropores due to the inhomogeneity of their precursors [90]. Pelletized carbon contains macropores in the form of interparticle voids. With the primary particle size being mostly lower than 40 $\mu$m in the case of commercial products, intraparticle diffusion is less of an issue. However, in case of larger primary particles as for polymer derived carbons, larger pores are required to facilitate rapid mass transport. While micropores are yielded through the gasification of a part of the polymer precursor, meso- or macropores need to be incorporated by other means.

Templating methods promise a structural approach to the pore size and morphology on different length scales ranging from micro- to macropores. **Hard templating** employs a solid phase material that can survive the high temperatures of pyrolysis and is eliminated afterward. Thus, the space that was occupied by the solid material transforms into pore volume. For the creation of micropores, zeolites can be used. Micropores can be introduced during the pyrolysis in the production of conventional carbon material. Therefore, this templating approach aims for morphological control that cannot be achieved otherwise. Zeolites are nanoporous aluminosilicate crystals with thin pore walls below 2 nm in size. As a precursor, firstly, polymerization in the pores of NaY and USY zeolites can be conducted, as shown by Kyotani et al. [91]. They successfully carbonized poly(acrylonitrile) and poly(furfuryl alcohol) inside the zeolite and achieved specific surface areas (BET) of 580 to 700 $m^2g^{-1}$. Secondly, they introduced carbon directly through chemical vapor deposition (CVD) of propylene gas at a temperature of 700 to 800 °C achieving up to 2260 $m^2g^{-1}$ (BET). Later work showed that through CVD, even higher SSAs of up to 3600 $m^2g^{-1}$ (BET) are possible [92]. The method can be applied to various zeolites in order to yield differently structured microporous carbon with pores of high regularity [93]. However, for the removal of zeolites, aggressive chemical leaching, which employs hydrofluoric acid or strong bases, needs to be conducted, which makes the commercial synthesis of zeolite templated carbon expensive.

In contrast to zeolites, hard templating with porous silica yields mesoporous carbons. Since the carbons replicate the structure of the silica pores, they are referred to as ordered mesoporous carbon (OMC). The synthesis includes: i) production of the silica template, ii) infiltration of the template with a polymeric carbon precursor and crosslinking if needed, iii) pyrolysis of the polymeric precursor, iv)

removal of the template with an ethanolic solution of NaOH.
Ryoo et al. synthesized the first self-supporting OMC from silica MCM-48 with mesopores originating from the template (3 nm) and additional micropores (0.5 to 0.8 nm) [94]. Since the cylindrical silica pores were not interconnected, the produced carbon consisted of singular rods. In a later work, Ryoo et al. [95] used a calcined SBA-15 that possessed interconnected pores in order to create carbon bridges that stabilize the mesopore structure, as shown in Figure 2.6. Since then, a wide range of mesoporous silica materials has been used for the synthesis of OMC. Cubical structured mesoporous carbon was created by impregnating MCM-48 with cubic aluminosilicate [96, 97]. SBA-15, with its hexagonal structure, yielded a hexagonal structured carbon [98, 99, 100]. With the use of MSU-H as a template, OMC with a mesopore size of approximately 4 nm was synthesized [101]. The introduction of aluminum onto the surface of SBA-15 allowed for polymerization of furfuryl alcohol selectively at the pore wall. The resulting carbon incorporated not only the around 4.2 nm large pores originating from the silica template but also up to 5.9 nm large pores inside the carbon cylinder originating from the selective polymerization and hollowness of the polymer precursor respectively [102].

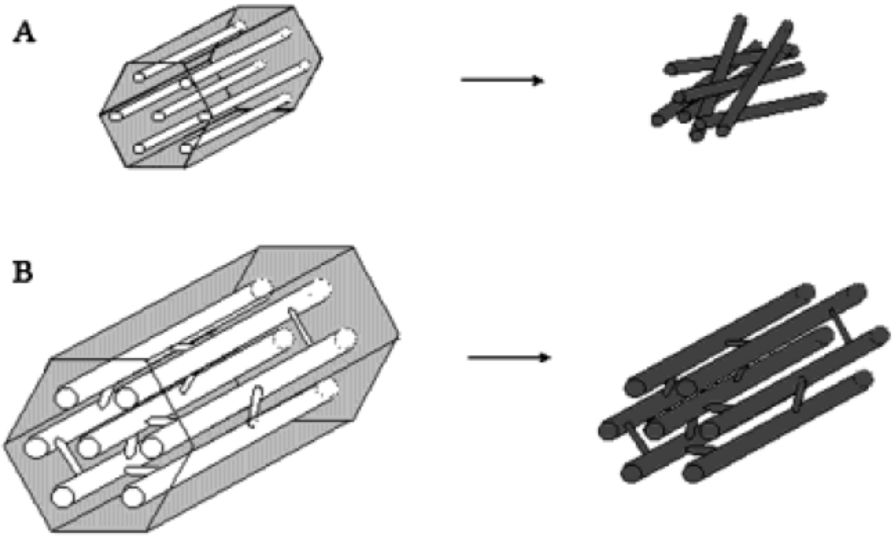

**Figure 2.6:** Schematic illustration of the formation of A) disordered carbon using a template with disconnected pores (MCM-41, or SBA-15 calcined at temperatures of about 1243 K), and B) ordered CMK-3 carbon using a template with an interconnected pore system (for instance SBA-15 calcined at temperatures below about 1173 K). Reprinted with permission of [95].

As a template, also spherical silica particles can be employed in order to produce macroporous carbons in a core-shell or hollow structure type. In these hollow structures, the pores have a high degree of regularity as the silica spheres arrange in close packing. Processing of these structures follows the same steps as porous silica templating, including polymerization, pyrolysis and etching of the template. In contrast to the cylindrical pores of OMCs, particle templated carbons exhibit pore bottlenecks at the point of contact of the silica spheres [103, 104].
As an alternative to silica, also other materials like nickel foams or alumina nanoparticles can be used for templating [105, 106].

In hard templating, the solid material survives the high temperatures during pyrolysis and can be removed subsequently. **Soft templating** uses another approach. Through different methods, the polymer precursor is shaped and pores are introduced, which need to survive the pyrolysis. In the literature, four critical requirements for a successful soft templating method have been stated: i) There has to be a driving force for self-assembly of the template and the carbon precursor. ii) The system has to consist of at least one carbon forming and one pore-forming species. iii) The template needs to be stable enough for sustaining crosslinking conditions for thermal or chemical curing of the carbon source but can be decomposed during the carbonization. iv) The carbon source needs to be highly crosslinked and morphologically stable enough to sustain the templated pore structure.

One method of soft templating is to use amphiphilic molecules. Moriguchi et al. [55] first introduced this method. Using cetyltrimethylammonium bromide (CTAB) as a surfactant, they successfully formed micelles as mesophase in a phenolic resin. The driving force for the microphase arrangement was the attraction of the ammonium ion at the outside of the micelle to the negatively charged ionized hydroxyl group of the phenols. After crosslinking with formaldehyde, they yielded a porous polymer. By varying the ratio of phenol to CTAB from 1:1 to 6:1, they created different polymer structures, such as lamella, hexagonal or disordered mesophases. The size was varied through the alkyl chain length of the template from tetradecyl (C14), which yielded 2.9 nm, to octadecyl (C18), which yielded 3.7 nm. However, they were not able to produce a porous carbon, since the structure collapsed at 200 °C. The synthesis of a porous carbon using CTAB was reported by Li et al. [107], who used pitch with negatively charged terminal groups that form a mesostructure with the polarized surfactant molecules. In general, it is believed that the long alkyl chains of the template also contribute to the carbon formation and often cannot be wholly volatilized. Thus, they occupy the mesospace and make it challenging to obtain mesoporous carbon.

As an alternative, amphiphilic block copolymers can be utilized. With their tunable properties, they can self-assemble into various architectures. As such, polystyrene-b-poly(4-vinylpyridine) (PS-b-P4VP) was utilized by several workgroups [108, 109]. Liang et al. [108] illustrated the basic working principle, as shown in Figure 2.7. In the first step, both the block copolymer and the resorcinol were dissolved and cast as a film. Hydrogen bonding between the pyridine nitrogen and the resorcinol's hydroxyl group then causes self-assembly upon evaporation of the solvent. The polymerization of resorcinol is conducted upon the addition of formaldehyde, in order to yield the carbon precursor. After pyrolysis at 800 °C, the template was nearly completely volatilized and mesopores of 33.7 nm remained in the carbon.

As another template, Pluronic triblock copolymers with the structure poly(ethylene oxide)-b-poly(propyleneoxide)-b-poly(ethylene oxide) can be used. It employs the difference in polarity of the blocks in order to attract the polymer precursor selectively. Tanaka et al. [110] used Pluronic F127 as a template in combination with a resorcinol/formaldehyde copolymer. After heating to 400 °C under an inert atmosphere, the template decomposed, but the chemical composition of the phenolic polymer did not change. This finding fits to the decomposition temperature of polyethylene glycol, which has a similar molecular structure like the block copolymers and starts at 160 °C [111]. Upon pyrolysis at 600 and 800 °C, the phenolic resin was successfully converted to carbon. In this process, the mesopore size decreased from 7.4 to 5.9 nm. In several publications, it was shown that the mesopore size could be tailored through the size of the block copolymer. By variation of the template to carbon source ratio or PPO to PEO ratio, also the pore morphology can be changed [112, 113].

**Figure 2.7:** Schematic representation of the synthesis protocol for the preparation of mesoporous carbon films and SEM images thereof with pores of 33.7±2.5 nm, as presented by Liang et al. Reprinted with permission of [108].

These soft templating can be viewed as a well-controlled method for shaping the polymer before carbonization since the templates are usually volatilized prior to the decomposition temperature of the carbon precursor. Besides using micelles, also foaming or high internal phase emulsion can be employed for creating porous polymers and then carbons. The drawback of these methods is that the polymer precursor is usually highly porous $> 70\,\%$ in combination with large pore diameters [62, 68].

Another way is the so-called **polymerization induced phase separation (PIPS)** or **liquid porogen method**. Usually, monomers and an initiator suffice for a polymerization reaction. For creating a porous polymer, the porogen, which is an inert liquid substance, is added to this reaction mixture. Upon polymer chain growth and crosslinking, the solubility of this porogen decreases until phase separation occurs. Then, a porogen-rich liquid phase separates from the liquid, gel-like or solid oligomer/polymer phase. Subsequently, the liquid porogen can be extracted from the polymer with the use of a suitable solvent.
Liquid porogen templating is well-examined for the creation of porous polymer beads, monoliths or membranes and a wide variety of polymers. For the adjustment of the pore sizes introduced by this method, it is crucial to choose a porogen with a suitable solubility. In case a good solvent is used, phase separation occurs at a point of time with a large degree of crosslinking during the polymerization, usually after gelation. Then, the speed of diffusion is low and only small domains of the porogen phase can form. After extraction, this polymer is micro- to mesoporous and possesses a large specific surface area. A good solvent is characterized by Hansen solubility parameters close to the ones of the polymer. In this model, the solubility can be estimated by a combination of disperse, dipolar and hydrogen bond interactions [114]. Among others, Hao et al. [115] give a good example. In an emulsion polymerization process for the production of PDVB spheres, they introduced heptane and toluene. Toluene could be introduced in large amounts until five times of the weight of the monomer and yield a micro- and mesoporous polymer with an SSA of 481 $m^2g^{-1}$ and an average pore diameter of 4.6 nm. When heptane was used as a porogen instead, the average pore diameter was around 14 nm.
The achieved pore diameter strongly depends on the solubility of the polymer chains in the porogen. If it decreases, phase separation occurs earlier during the polymerization, usually before the gelation.

In this case, the polymer chains are not or only to a small degree crosslinked. Therefore, the porogen is highly mobile and can form large domains. As a result, the extracted polymer is macroporous and exhibits a small specific surface area. Non-solvating porogens differ from the polymer in terms of Hansen parameters, as was shown by Dubinsky et al. [116]. They used diethyl-, dibutyl-, dioctyl-, and didecyl phthalate as porogen for poly(glycidyl methacrylate-co-ethylene glycol dimethacrylate) spheres from emulsion polymerization. With longer aliphatic chains of the porogen, the templated pore sizes increased from 100 nm to the range of a few micrometers, as shown by images, while the solubility parameter decreased. Additionally, phase separation can also occur if the monomers do not dissolve their polymers, as in the case of vinyl chloride and acrylonitrile and therefore yield macroporous polymers. This is called the self-porogen effect [117].

As an extreme case, also oligo- or polymers such as polystyrene, poly(ethylen oxide) or poly(methyl methacrylate) can be used as porogen. Then, phase separation occurs even earlier and macropores larger than 1 $\mu$m result, if the polymeric porogen can be successfully extracted [118].

Figure 2.8 depicts examples of porous polymers caused by solvating, non-solvating and polymeric porogens. A particular case of porogen is supercritical $CO_2$. Its solvation properties can be adjusted by pressure. Thus, it can be solvating or non-solvating depending on the process conditions [119, 120, 121].

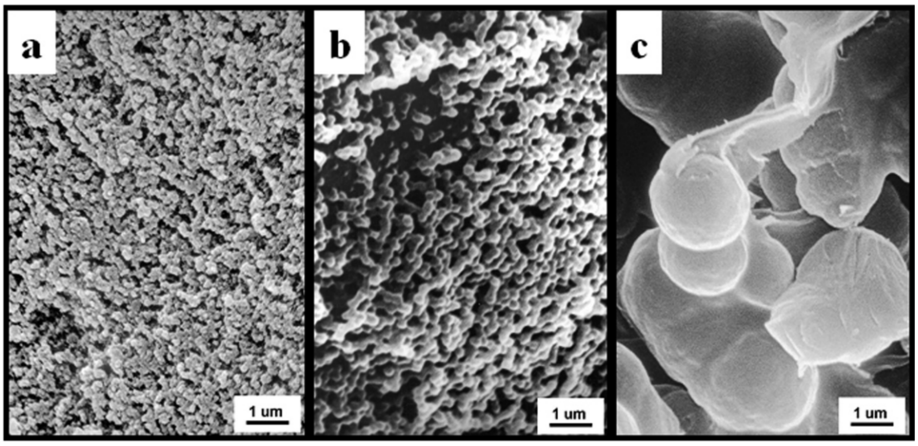

**Figure 2.8:** Scanning electron micrographs of poly(Glycidyl methacrylate-co-Ethylene glycol dimethacrylate) beads prepared in the presence of various porogens. Polymerization mixture: 60% porogen (a –toluene, b – dodecanol, c – polystyrene solution in toluene (15%, MW 50000)),24 % Ethylene glycol dimethacrylate, 16 % Glycidyl methacrylate. Reprinted with permission of [118].

In addition to the solubility of the polymer in the porogen monomer mixture, various other factors are impacting the resulting porosity. The most important one is the volume fraction of the porogen. In the case of a large amount of porogen, larger domains form and the SSA can even decrease compared to lower amounts. Vise Versa, also non-solvating porogens can be kept dissolved during gelation if they are contained to a small degree only in the monomer phase. Furthermore, a small amount of crosslinker can enable the formation of larger porogen domains even after gelation of the polymer, since it decreases the rigidity of the polymer network. However, usually a high content of crosslinker is wanted to retain the porous structure after extraction. Also, the speed of polymerization plays a factor. When the concentration exceeds the solvation limit, phase separation does not occur instantly, as it requires a certain degree of over-saturation. Therefore, the pore size decreases with a larger speed of polymerization. Lastly, it has to be noted that temperature impacts many factors in porogen templating and needs to be accounted for.

Although the liquid porogen method is mostly used for the synthesis of porous polymers, there are a few examples that study the further processing to porous carbons. The reason is that other soft templating methods can yield more well-defined pore structures, while phase separation yields hard to control geometries.

Porogen templating for the creation of carbons divides into three subgroups. The most widely used porogen are glycols or polyethylene glycols [122, 123, 124, 125, 126]. Kaneda et al. used ethylene glycol as a porogen in combination with phenol-formaldehyde resin. The template volatilized during the carbonization process. Due to the morphological stability of phenol-formaldehyde thermosets, the morphology was retained upon pyrolysis at 1000 °C in nitrogen. The pore size was varied in a range of 0.5 to 11 $\mu$m through the curing temperature.

Secondly, common organic solvents are employed. Malik et al. [70] used a nonan:toluol 1:9 mixture as porogen and varied the acrylonitrile to DVB ratio from 30:70 to 70:30. By extraction, they yielded micro- and mesoporous polymers with an SSA of up to 720 $m^2g^{-1}$. Upon oxidation at 300 °C and subsequent pyrolysis at 850 °C, the SSA, as well as the pore volume, decreased by more than 50 %. Only in the case of the least porous polymer, the SSA increased from 34 $m^2g^{-1}$ to 212 $m^2g^{-1}$. These observations show that small micropores introduced by porogen templating are not stable during pyrolysis even if post-cured by oxidation, a method that stabilizes the macrostructure of the polymer. Shi et al. [127] used dodecyl alcohol for porogen templating a styrene-divinylbenzene copolymer. Upon carbonization at 900 °C (0.5 $K\,min^{-1}$) without prior stabilization, macropores in the range of 1 $\mu$m in combination with an SSA of 624 $m^2g^{-1}$ were achieved.

Thirdly, also ionic liquids were utilized as porogen in combination with resorcinol formaldehyde resins [128, 129]. After the reaction, the ionic liquid was extracted with water and the thermoset carbonized at 800°C. The yielded macropores in the carbon material had a diameter of 1 to 10 $\mu$m [129].

In contrast to porous polymers, which are usually porogen templated with regards to high specific surface areas, in case of carbons, the micropores are introduced by pyrolysis and non-solvating porogens are utilized to introduce macropores.

Hard templating enables the production of numerous morphologies in a well-controlled manner. However, due to the template synthesis and removal, which requires harsh chemicals, this method is time and material consuming. Thus, it is not suitable for industrial-scale production. Many soft templating methods also provide well-controlled mesopore geometries. Since the template can be removed during the pyrolysis, a large scale production is more viable to accomplish and the environmental impact is smaller. So far, the research has been mostly focused on methods that give the best control over the pore geometry. Although there is plentiful of research about using polymerization induced phase separation for the production of polymers, there are few papers that use it for the synthesis of porous carbons. While this method does not provide ordered pores, it controlled the pore size and volume over a wide range.

## 2.3 Additive manufacturing

Traditionally, many fabrication methods in industry relied on subtractive processes like machining, milling or drilling. In these cases, the sheared-off material is wasted and the freedom of design is limited. As a new approach, many additive fabrication methods and apparatuses have been invented during the last decades. In additive manufacturing, 3D printing or rapid prototyping, as it is also called, the desired product is created in a bottom-up approach often in a layer-wise manner. This method greatly reduces the amount of waste and previously impossible designs, such as a honeycomb structure inside a wall, can be printed as one part (see Figure 2.9). With these advantages, 3D printing methods have been established and applied in the field of rapid prototyping, in piece production or low production volumes.

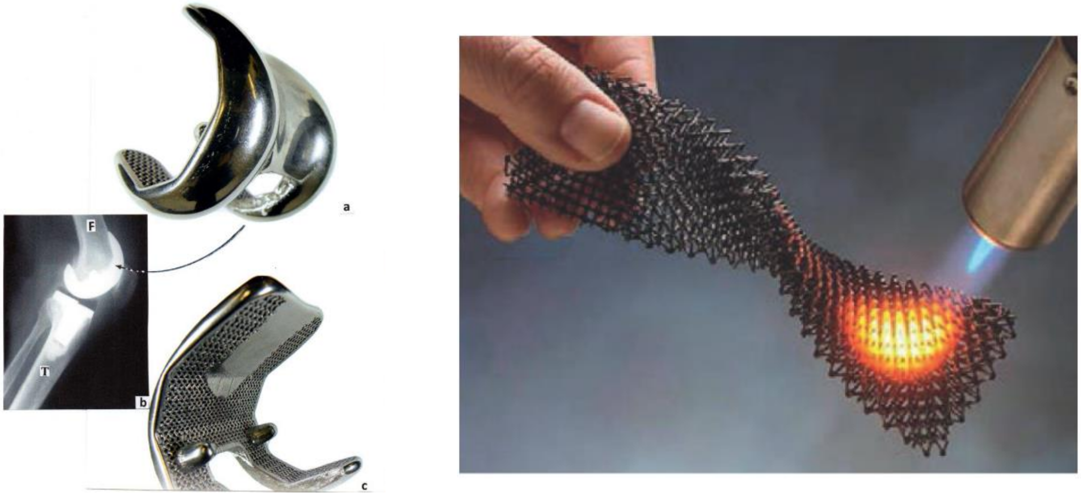

**Figure 2.9:** Left: Co-Cr-Mo total knee replacement printed via electron beam melting [130]; Right: Polymer derived ceramic open-cell structure printed via stereolithography [131]. Reprinted with permission of [130, 131]

### 2.3.1 3D printing methods

Despite a recently risen interest, the idea of 3D printing has been introduced in the 1970s. In the year 1977, Swainson [132] filed a patent for a machine that stereoselectively polymerized a photopolymer at the intersection of two beams of light, thus building up a continuous structure. This method is nowadays known as stereolithography (SLA). An SLA apparatus, as we know it, was introduced in 1984 [133]. In general, 3D printing processes divide into 3 phases:

1. Computer-aided design of a 3D model
2. 3D print
3. Post-processing

For the 3D modeling, various software like Solid Edge, OpenSCAD or the Windows 10 integrated 3D builder exists as proprietary or open-source solutions. The rendered 3D file is then converted into machine code and executed by the 3D printing device. For the printing of different materials, including metals, polymer or concrete, a wide variety of different additive manufacturing techniques have been invented. In the following, 3D printing methods for the most relevant material classes are presented. Figure 2.10 displays schemes of the essential 3D printing methods for polymers.

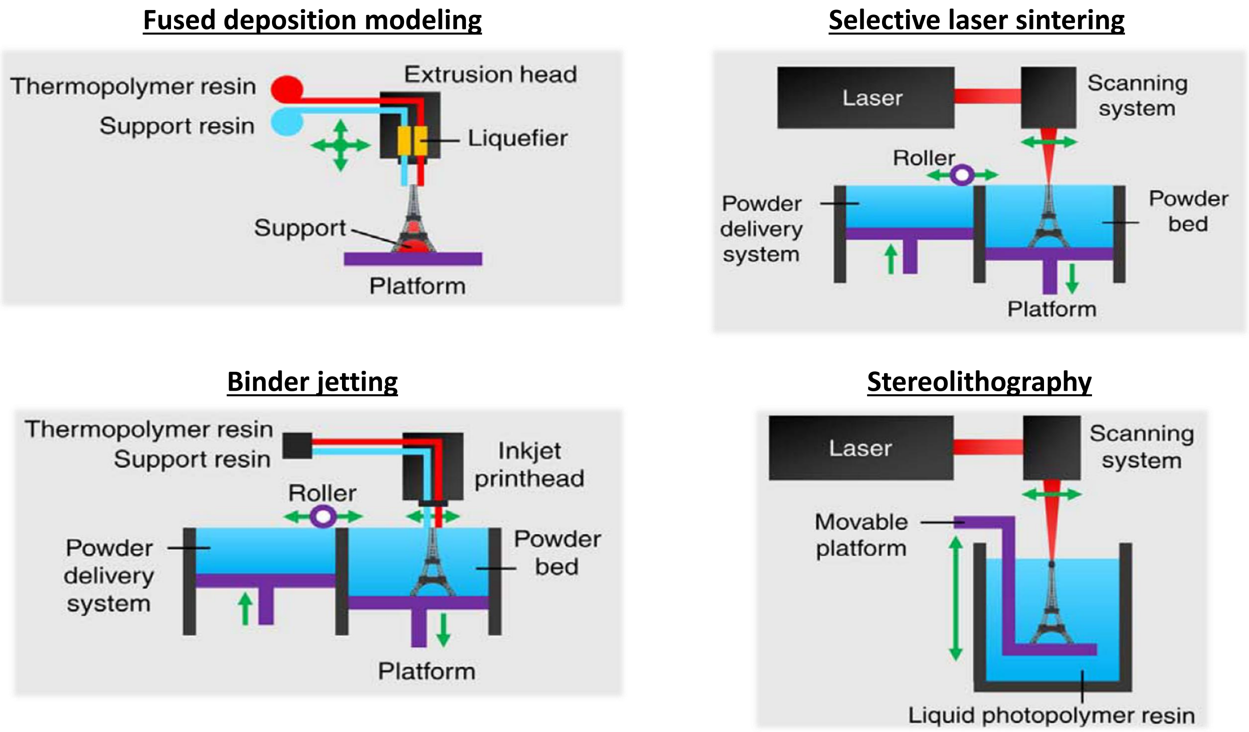

**Figure 2.10:** Most essential methods for the 3D printing of polymers or polymer composites. Reprinted with permission of [134].

In **direct energy deposition (DED)** or **direct metal deposition (DMD)**, metal powder or wire is molten and deposited directly on the substrate. The laser engineered net shape (LENS) method uses a laser beam that heats the substrate and the metal particles that are jetted out a nozzle by the inert gas flow. Through inertia forces, the heated metal particles deposit on the substrate.
Electron beam additive manufacturing (EBAM) works with metal powder or electric wire. Instead of a laser, an electron beam welds the additional material to the substrate under vacuum. With DMD, either complete parts can be created or additional material can be deposited onto classically printed parts. It also functions in combination with machining. As materials, titanium, stainless steel or aluminum have been used [135].

**Powder bed fusion (PBF)** is a technology that also uses an energy source to melt a metal or thermoplastic powder located in a powder bed. In the process of printing, layer-by-layer fresh powder is added and selectively molten. The unutilized material can be reused to a large extent. Several methods differ in terms of energy source and material. Electron beam melting (EBM) utilizes a high energy electron beam to heat up and melt metal powders in a small localized area. Importantly, the process requires an electrically conductive material and a vacuum [135]. In direct metal laser sintering (DMLS), a laser is used for selectively liquifying metal powder on the surface of a powder bed. The method has been proven to be compatible with many alloys such as Inconel or Ti-6Al-4V. Although originating from powdered material, EBM or DMLS printed parts can be manufactured with nearly zero porosity, which gives them similar mechanical properties as if conventionally produced [136]. Although the working principle is similar, selective laser sintering (SLS) (see Figure 2.10) uses powders of thermoplastics as raw material. It was proven to work with a range of plastics such as polyamide, PEEK or particle-reinforced with glass or carbon fiber. As the powder bed supports the printed parts, with PBF also overhanging elements can be printed that would otherwise need a support structure [134].

**Binder jetting** (see Figure 2.10) works via bonding together layers of powder. In contrast to PBF, not the powder is molten but glued together by a binder, introduced via inkjet printing. Thus, a large variety of materials, including plastics, metals, ceramics and graphite can be processed. As the bed carries the weight of the printed parts, no support structures are needed. The binder can be directly illuminated and polymerized or thermally treated afterward for an increase in mechanical properties [134].

In **material jetting**, a liquid photopolymerizable resin is deposited onto the substrate in an inkjet like manner and subsequently cured by UV irradiation. Layer-by-layer, this process fabricates a polymeric structure. Different materials can be printed simultaneously to create a composite or add support structures needed for overhanging elements. These support structures are often water-soluble and can be removed afterward. Material jetting is especially interesting for applications that require different materials or colors as it is needed in design for realistic prototyping [134].

**Fused filament extrusion (FFE)** or **fused deposition modeling (FDM)** (see Figure 2.10) is the most widely known additive manufacturing method in the public awareness since it experienced a tremendous price drop down to 150€ for a single printer. In this method, a thermoplastic is molten and extruded through a nozzle onto the substrate, at which it leaves a layer of the resolidified material. This process is very cost-effective, as raw material filaments are produced from commodity thermoplastics like ABS, PE or PLA industrially or waste PET bottles by oneself. Apart from that, FDM has also been used for thixotropic materials like concrete or some resins [137, 138]. FDM is the method that has found its way into people's homes the most, although it is also applied industrially. FDM produced parts can be used without further post-processing after potential support structures have been removed [134].

**Vat polymerization** or **lithographic 3D print** is a group of techniques that photopolymerize a liquid resin from a vat (see Figure 2.10). The methods differ in terms of their light source and mode of operation. Stereolithography (SLA) employs a UV laser that induces the photopolymerization. For each layer of polymer, the laser rasterizes the whole area at which solidification is required. In contrast to that, in digital light processing (DLP), a photo projector illuminates the whole area at once. In both methods, the light source can be located above the resin vat or below. After the polymerization of a layer with a distinct height, the building platform is lowered or elevated in order to make space for a new layer of liquid photoresin to be illuminated. This process is continued until the whole model is built [134].
Continuous DLP (CDLP), which is also known as continuous liquid interface production (CLIP), utilizes a DLP projector as a light source from below the resin vat. Instead of working in distinct layers, the build platform moves up continuously. To prevent the polymer from sticking to the vat's bottom, oxygen can permeate through a membrane from below into the resin. This process inhibits polymerization in the first micrometers above. Thus, CLIP allows for much higher printing speeds, which enabled more widespread commercialization [134].

Instead of using one UV or blue light photons to activate the photoinitiator, the 2-photon-lithography employs two IR photons. Only at the intersection of two IR lasers, the intensity is large enough to solidify the resin. As the chance of activating the photoinitiator in 2-photon-lithography is much more dependent on the light intensity, much finer resolutions in the range of 50 nm can be realized [139].
Lithographically printed polymers often require additional post-treatment. After printing, they are not entirely polymerized and have not reached their final state and mechanical properties. Therefore, additional UV-curing at room or elevated temperatures is commonly conducted [134].

In summary, a large variety of materials have been 3D printed. Most methods employ the melting of the raw materials as a way to bring it into a new shape and build up a larger structure. Also, carbons in the form of graphitic particles or carbon fibers have been introduced into thermoplastics to create composite materials. These undertakings aim for improvement of mechanical properties and not for creating a porous material, as will be discussed in subsection 2.4.

### 2.3.2 Lithographic 3D printing of polymers

There are numerous applications for 3D printed polymers, such as in design, making models in dentistry, replacement parts, scaffolds for cells or casts. The tailored design of the photoresin can meet the requirements of these applications in lithographic 3D printing.

3D printing resins are categorized into radical and cationic systems. Since normal air, including oxygen and moisture, usually surrounds the resin vat, anionic polymerization is not suitable due to its high sensitivity toward these factors. The monomer mixture is determining for the properties of the printed part and needs to fulfill several requirements, such as fast polymerization, low degree of shrinking, suitable viscosity and mechanical properties of the resulting polymer. Generally, the photoresin requires the following ingredients:

- Monomers and oligomers
- Photoinitiator
- Inhibitor
- Dye

Photoresins for **radical polymerization** usually employ acrylates, since they exhibit a rapid reaction rate. Figure 2.11 displays several commonly used monomers and photoinitiators for radical polymerization. Due to their multiple acrylate functionalities, the monomers create a crosslinked network that helps to increase mechanical properties and reduce shrinkage compared to monofunctional ones. They also require a lower conversion for solidification compared to monofunctional monomers [140]. During polymerization, the density usually increases gradually as the molecules have less freedom of movement. The size reduction due to polymerization can amount up to 12 % and it needs to be accounted for in the prior design [141]. Furthermore, cracks can create in the final structure upon post-polymerization or small features curl due to an uneven prior crosslink density, as the light intensity decreases further into the resin during the print of a single layer [142]. Using a monomer (e.g., PETA) that has a high liquid density through hydrogen bonds of the monomer molecules can reduce shrinking. Also, monomers with cycloaliphatic parts like DCPDA or aromatic parts like bis-GMA were claimed to mitigate this effect [141] and help to tailor mechanical properties or biocompatibility through additional functionalities [143]. Since the printed part often has to be detached from the bottom of the resin vat, the viscosity of the acrylate monomer mixture is usually too high and needs to be decreased for reduced detachment force. For this purpose, high reaction rate small molecular weight monomers like n-vinylpyrrolidone are employed [144].

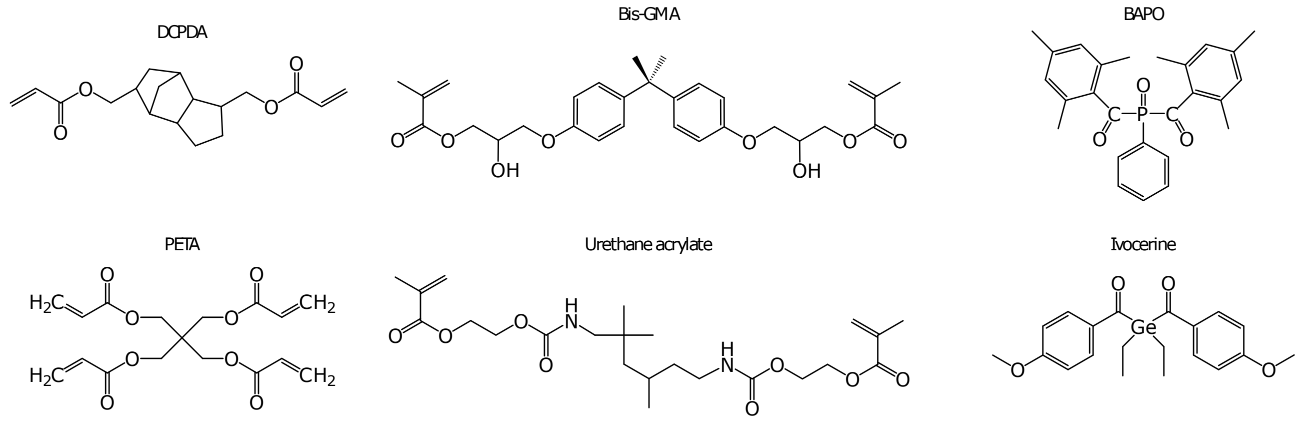

**Figure 2.11:** Monomers and initiators of radical photoresins: DCPDA: Dicyclopentadienyl diacrylate; PETA: Pentaerythritol tetraacrylate; Bis-GMA: Bisphenol A-glycidyl methacrylate; Urethane acrylate; BAPO: Phenylbis(2,4,6-trimethylbenzoyl)phosphine oxide; Ivocerine: bis(cyclo- pentadienyl) bis[2,6-difluoro-3-(1-pyrryl)phenyl]titanium.

The light source of the 3D printer determines the choice of photoinitiator. The popular stereolithographic printers from formlabs utilize a laser of 405 nm wavelength, while others have a shorter wavelength at 385 or 355 nm. DLP based printer, however, utilize longer wavelengths starting from 410 to 420 nm as they incorporate an IR and UV filter for safety reasons. UV active initiators such as benzil ketals (up to 360 nm), which were first used in combination with UV lasers [144], are therefore not compatible with nowadays light sources for non-industrial applications. As a consequence, a couple of blue light photoinitiators have been developed. Most prominently, phosphine oxide derivatives such as BAPO are used due to their absorption until 420 nm and high reaction rate [145]. Germanium based photoinitiators express an even broader spectrum of absorption up to 470 nm [146]. These are all type 1 photoinitiators that undergo direct cleavage upon photon absorption. Apart from this, there are also type 2 systems, which work via hydrogen abstraction from a co-initiator. In 3D printing, camphorquinone can be utilized together with amines as it works in wavelengths until 500 nm. Despite the broad absorption, it suffers from low reactivity [147, 32]. So far, there are various attempts to find suitable visible light photoinitiators, but there is more research needed in this field [148].

Furthermore, photoresins require an inhibitor such as monoethyl ether hydroquinone or tert-butylcatechol to prolong shelf-life during storage and to avoid unwanted polymerization at non-illuminated areas during the 3D print [149]. Also, a dye limits the light penetration depth into the photoresin. Thus, in each cycle, only a layer of distinct thickness is polymerized.

In lithographic 3D printing, also **cationic polymerization** is used. As monomers (see Figure 2.12), firstly, epoxides such as DGEBA or ECC are used. Due to their ring-opening reaction, they tend to have very low shrinkage of 2 to 3 % [150, 151]. However, their reaction rate is much lower than radically polymerized acrylates [152]. Therefore, secondly, epoxides are also used in combination with vinyl ethers like TTVE or CDVE, which can also be polymerized cationically and provide a much faster reaction rate. In this case, the vinyl ethers create a solid network and the epoxides can be post-cured through thermal treatment. Thirdly, oxetanes can be used, as they polymerize faster than epoxides but exhibit similar shrinkages [153, 154]. For cationic photopolymerization, photoacids function as initiators. They were introduced in the 1970s in the form of aryl iodonium salts ($Ar_2I^+X^-$) with fluoride anions ($BF_4^-$, $AsF_6^-$ or $SbF_6^-$) [155]. In a series of reactions after photolysis, these form superacids (e.g., $HBF_4$ or $HSbF_6$) as products, which can initiate polymerization. Since then, triarylsulfonium as cations increased the photosensitivity to beyond 400 nm. Also, visible light cationic photoinitiators such as titanocene salts (up to 500 nm) have been developed [156]. For cationic 3D print, amines function as inhibitors.

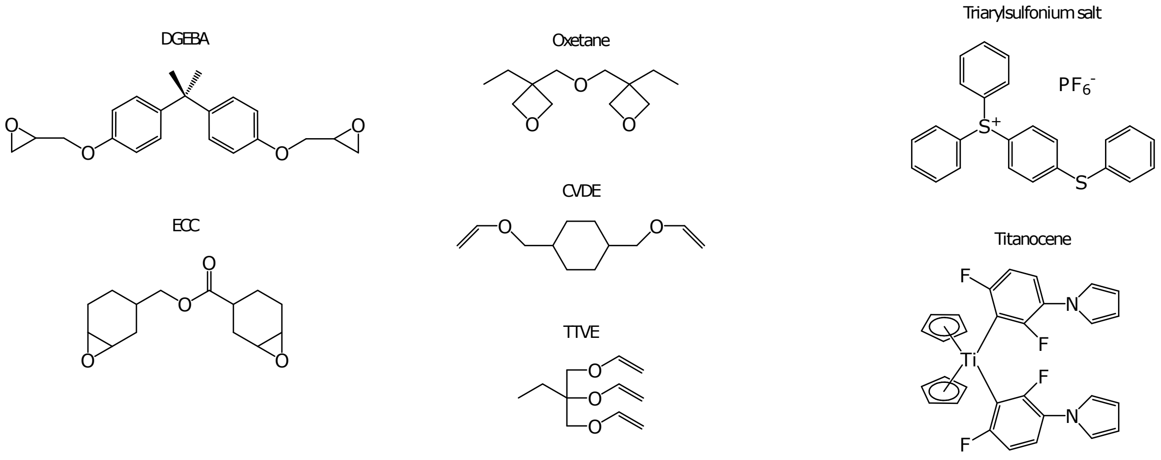

**Figure 2.12:** Monomers and initiators of cationic photoresins; DGEBA: Bisphenol-A-diglycidylether; ECC: 3,4-Epoxycyclohexylmethyl-3′,4′-epoxycyclohexane carboxylate; Oxetane: Bis(3-ethyl-3-oxetanylmethyl)ether; CVDE: 1,4-Cyclohexanedimethanol divinyl ether; TTVE: Trimethyloylpropane trivinyl ether; Triarylsulfonium salt: (4-Phenylthiophenyl)diphenylsulfonium hexafluorophosphate; Titanocene: bis(cyclopentadienyl) bis[2,6-difluoro-3-(1-pyrryl)phenyl]titanium.

## 2.4 3D printing of carbon

Carbon does not melt at reasonable temperatures and pressures. Therefore, it can not be extruded as a single material. Also, polymerization to a macromolecule is not feasible on a larger scale. One approach to realize 3D printing of carbon is to use carbon polymer composites. A 2017 patent of SGL carbon [1] utilizes binder jetting with graphitic carbon particles to produce graphite polymer composites. However, the polymer part limits the thermal and mechanical properties and replacement of this phase by annealing could damage the shape. Furthermore, the manufacturing of a porous carbon of similar kind inheres the problem of pore-clogging by the binder [157].

Also, extrusion-based techniques of composites have been employed. They are also called direct ink writing if the mixture has a low viscosity. In this method, the carbon material is extruded through a nozzle and either freeze-dried [158, 159] or held in position by thixotropic rheology [160]. After printing, they are thermally treated to remove the leftover binder. Figure 2.13 shows examples of extruded carbon structures. Due to its performance in electrochemistry and sheet-like structure, direct ink writing usually employ graphene oxide (GO) and graphene nanoplatelets (GNP). As a result, carbon structures of interesting mechanical properties [160], good conductivity [160, 158] or high specific surface area ($> 500\,\mathrm{m^2 g^{-1}}$) [158] were presented in several publications. Nevertheless, all these structures are based on single particles. Though they are interconnected by cross-linking reactions in some publications, it is evident that they do not exhibit the mechanical strength and electric or thermal conductivity of the raw material.

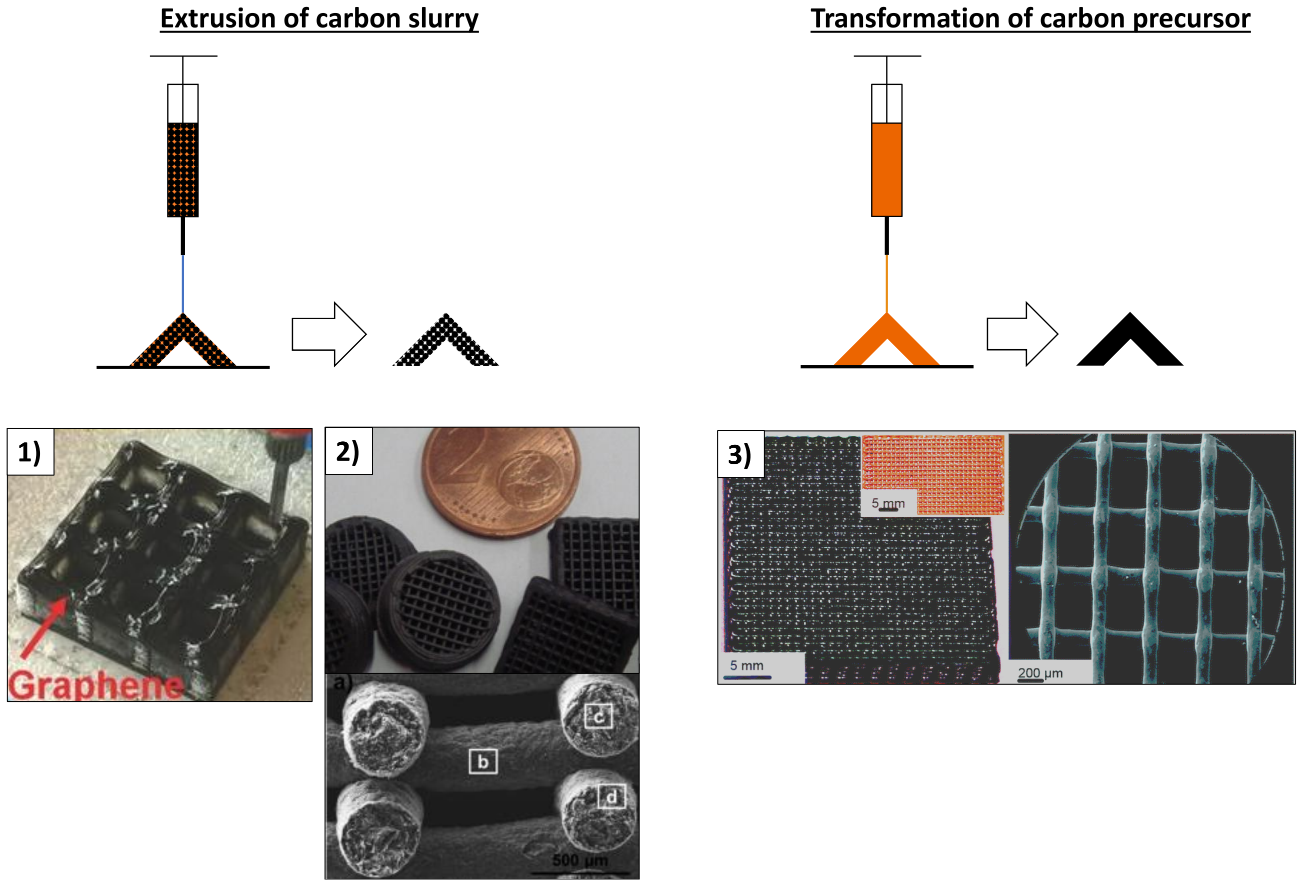

**Figure 2.13:** Examples of 3D printed carbon by extrusion of a carbon material or carbon precursor; (1): freeze dried graphene oxide structures [159], (2): annhealed graphene nanoplatelet structures [160], (3): pyrolyzed and activated carbon from resorcinol formaldehyde [138]. Reprinted with permission of [159, 160, 138].

Chandrasekaran et al. [138] presented the conversion of the extruded polymer into carbon. They used a resorcinol formaldehyde resin comprised of 3.2 g of 20 % formaldehyde solution, 1.23 g of resorcinol, 0.192 g of hydroxypropyl methylcellulose, 44 $\mu$l of glacial acetic acid and additional 9 wt% of fumed silica for the thixotropic properties. After 3D printing by extrusion, they cured the samples at 80 °C for 72 hours and supercritically dried them, followed by pyrolysis at 1050 °C ($2\,^{\circ}\mathrm{C\,min^{-1}}$). The carbonized samples did not exhibit open micro- but macroporosity. This issue was not addressed in the publication but likely originated from internal phase separation templating during curing. Upon $CO_2$ activation at

950 °C until a mass loss of 60 %, the specific surface area rose to 1894 $m^2 g^{-1}$. The researchers showed that upon shrinking of the solid feature size from 400 to 100 $\mu$m, the capacitive retention increased from 42 to 70 % (1 to 10 $A g^{-1}$). However, using rheology dependent direct ink writing or extrusion, only simple-structured geometries are possible. The smooth transition sheer resistance also causes sagging of the material. Therefore, most research groups limit their design to stacked horizontal cylinders.

Other than extrusion, also stereolithography can be used to create 3D printed structures that can be transformed into carbon, as was shown by Bian et al. [161] (see Figure 2.14). They utilized an acrylate-based commercial photoresin ("Clear 2005T" from Miicraft) in combination with a DLP lithography printer to produce polymer scaffolds. Pyrolysis of the scaffolds was conducted at 800 °C with a heating rate of 0.4 °C $min^{-1}$ between 350 and 450 °C, the zone of the highest rate of decomposition. Thus, the samples' mass decreased by 91 %, accompanied by a shrinking of 70 % in each dimension, which amounts to a volume reduction of 97 %. Still, the shape of the cubic lattice macrostructure was retained, yielding rectangular holes of 100 to 500 $\mu$m in diameter. With a lower ohmic resistance compared to carbon felt, the 3D printed carbon proved to be a suitable electrode material for microbial fuel cells. However, the researchers did not manage to create a porous carbon by this technique.

A view on the lithographically printed carbon showed a microstructure that can be precisely designed and printed, while extruded parts suffered from the limits of rheology. In contrast, extrusion-based techniques already presented specimen with a large specific surface area, when they were converted from a printed carbon precursor and sufficiently activated.

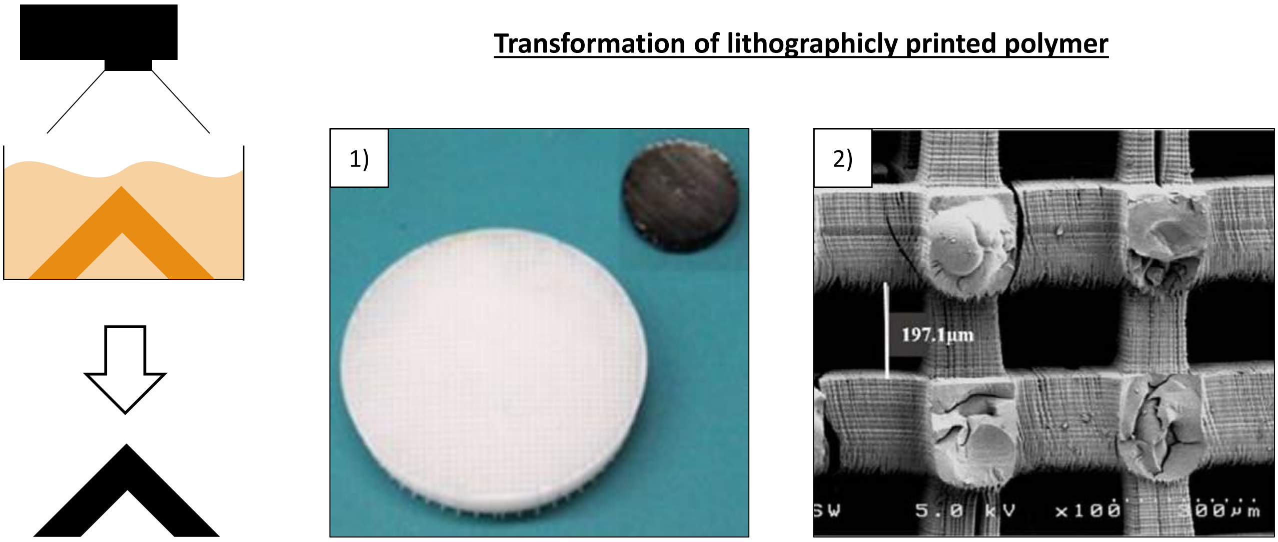

**Figure 2.14:** 3D printed carbon by lithographic printing of a carbon precursor and pyrolysis; (1): 3D printed polymer before and carbon after pyrolysis, (2): Microstructure of the carbon scaffold. Reprinted with permission of [161].

## 3 Goal and Scope of this Work

The examples from the literature about extrusion-based 3D printed polymers and their conversion into activated carbon illustrate that there is a good understanding of how to transform polymers into carbon. Some publications also show the advantages of lithographic 3D printing in terms of resolution and freedom of design. Nevertheless, there is no process for the production of 3D structured activated carbons that fulfills the following requirements:

1. Scalability of the method from the micrometer to the centimeter range
2. Complexity of the 3D printed structure (e.g. open cell structures)
3. Mechanical stability of the 3D printed structure
4. Tunable micro- and mesoporosity of the activated carbon

Therefore, it is the aim of this work to develop a 3D printing method that keeps up with traditional production methods in terms of the porous structure while exceeding the freedom of design and resolution of extrusion-based 3D printed carbons. The whole manufacturing process is displayed in Figure 3.1. It starts with the stereolithographic 3D printing of the CAD file with the photoresin. The extraction of the porogen from the polymer then yields the porous polymer monolith that is then converted to activated carbon with a thermal treatment in oxidative and inert environments.

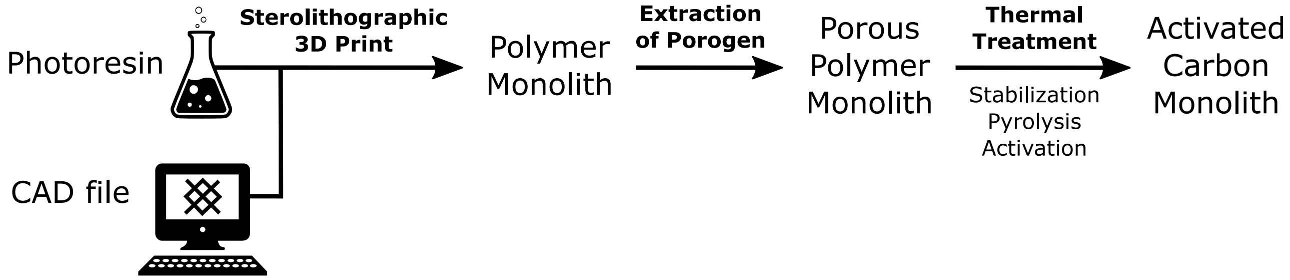

**Figure 3.1:** Schematic illustration of the 3D printing process.

At first, the composition of a suitable photoresin will be examined. Different monomers have to be screened and evaluated based on their carbon yield and speed of polymerization, as examined by IR spectroscopy. For the templating of meso- and macropores, the porogen method will be employed and combined with lithographic 3D printing. Both, type and amount of porogen shall be varied and their impact on the pore sizes investigated by using Hg porosimetry and $N_2$ adsorption analysis.

Secondly, based on the synthesis of 3D printed porous polymers, the transformation into activated carbon will be examined. The carbonization process is required to maintain the macrostructure and templated pores of the polymer precursor and needs to create a new fraction of micropores through the volatilization of a part of the material. For this, the impact of the temperature of oxidation in air as a pretreatment shall be investigated by temperature-programmed oxidation and thermogravimetry, Hg porosimetry and

$N_2$ sorption. In order to tailor the porosity, the carbon will be $CO_2$ activated and the impact on the micro- and macrostructure measured.
Lastly, the printing parameters should be adjusted for the production of larger monoliths.

The larger 3D printed monoliths will be utilized in an electric swing adsorption process, which constitutes the second part of this work. In the literature, particulate activated carbon, activated carbon fibers or felts, extruded activated carbon monoliths or carbon-zeolite-composites were used. In this work, an activated and non-activated carbon monolith will be compared with commercial activated carbon pellets in terms of their performance in the cyclic ESA process. Their temperature distribution shall be measured by thermographic imaging and measurements with thermocouples. The overall performance in adsorption and desorption will be evaluated based on the used carbon's mass, their porous properties and macrostructure.

# 4 Experimental Methods

## 4.1 Polymer prepration

As a precursor material for the production of activated carbons, porous polymers were prepared. Photopolymerizations were conducted either in a simplified setup or in the 3D printer. The non-reactive porogen was subsequently extracted by soxhlet extraction, finally yielding a porous polymer upon drying.

### 4.1.1 Photopolymerization using a simplified pellet geometry

For conducting photopolymerizations without the use of a 3D printer, a simplified setup was utilized. Transparent polyethylene snap-on caps of glass vials with an inner diameter of 11 mm were used as a vessel for the photoresin. For a photopolymerization, 150 $\mu$l of the photoresin containing the monomer, porogen and 10 mg ml$^{-1}$ BAPO were placed inside the cap and illuminated from the top. In the case of a copolymerization, equal volumes of each monomer were used. As a light source, a 300 W high-pressure mercury (HPHg) lamp (Ultra-Vitalux from Osram) was utilized.

### 4.1.2 3D printing of polymers

For 3D printing, the Kudo 3D “Titan 2 HR”, a DLP-projector based stereolithography printer, was employed. The distance from the top ring of the projector above the lens to the supportive acrylic plate holding the resin vat was set to 76 mm and the focus adjusted. This resulted in a maximum projected rectangular area of 67 mm x 40 mm. In the beam of the projector, a 50 mm x 50 mm and 3 mm thick blue glass filter was implemented covering the whole beam in order to filter out a fraction of light that is not utilized by the photoinitiator.
The custom-made resin vat consisted of an aluminum frame with outer dimensions of 180 mm x 220 mm and a height of 30 mm, leaving an inner space of 140 mm x 180 mm. On this frame, a 125 $\mu$m thick FEP foil was fixed with adhesive tape. The whole resin vat was supported by a 3 mm thick acrylic glass plate. The resin vat, together with the build platform superstructure, was covered by a red acrylic glass containment in order to exclude blue and UV light.

At the beginning of the 3D printing process, the building plate was homed by lowering it down (via the software) until it reached the bottom of the resin vat. Before adding the photoresin, the build platform was elevated by 3 mm.
In a typical 3D printing process, 100 ml of the resin were prepared. At first, the three liquid components PETA, DVB and the porogen were mixed. Then the color agent sudan1 was added and shook until fully dissolved. Afterward, 10 mg ml$^{-1}$ BAPO were added to the resin. In order to not to start the photopolymerization prematurely, the bottle was enwrapped with aluminum foil. Then, the mixture was placed in a shaker until the initiator dissolved entirely.

After pouring the photoresin into the resin vat, the build platform was lowered down to the bottom of the vat. While covering its lens, the projector was turned on and given 5 minutes to heat up. After removing the cover, using the desired settings, the 3D printing process can be started.

The 3D printing consists of the sequential illumination and stereoselective polymerization of single layers, and elevation of the build platform to detach the printed part from the FEP foil. The operational parameters for each layer can be defined individually. The illumination time for the first layer was set to 240 s, assuring a tight grip to the build platform and preventing detachment during the print. If not stated otherwise, the following parameters, shown in Table 4.1, were used.

**Table 4.1:** Parameters for 3D printing of polymers using the Titan 2 HR from Kudo 3D.

| From layer | To layer | Exposure time | Lift speed | Lift height | Down speed | Delay |
|---|---|---|---|---|---|---|
| 1 | 2 | 240 s | $2\,\mathrm{mm\,min^{-1}}$ | 4 mm | $10\,\mathrm{mm\,min^{-1}}$ | 0,5 mm |
| 2 | 780 | 75 s | $4\,\mathrm{mm\,min^{-1}}$ | 2 mm | $50\,\mathrm{mm\,min^{-1}}$ | 0,5 mm |

In contrast to the high-pressure mercury (HPHg) lamp, the UV spectrum of commercially available 3D printer projectors is filtered out for safety reasons. The UV-Vis emission spectra and the absorption spectrum of the photoinitiator phenylbis(2,4,6-trimethylbenzoyl)phosphine oxide (BAPO) are displayed in the appendix in Figure 7.2 (p. 78).

### 4.1.3 3D modeling of open-cell structures

For the use in the 3D printer, a 3D model has to be created and subsequently sliced, which yielded a ZIP file containing a numbered png-file for each slice. For the modeling, the programming based compiler SCAD was used. The source code for the tetragonal open-cell structures is provided in subsection 7.1 in the appendix (p.77).
Nevertheless, the printed part should not be printed solely. In this case, it would be directly attached to the base plate and might be detached during the print due to an overly small area of adhesion to the baseplate or it could not be detached after the print without breaking the structure due to strong adhesion. As a solution, firstly, a one-millimeter thick rectangular layer at least as large as the main part was added to the structure. This structure was first to be printed and provided a strong force of adhesion to the base plate. Secondly, vertical cylinders ($d = 1.5\,\mathrm{mm}$) were added connecting the main part and these first layers. These cylinders can be broken in order to detach the main printed part. The whole assembly is illustrated in Figure 4.1.

Subsequently, the 3D model was exported as an STL file and further processed with a slicing program. For this, the java script application SLAcer (found under http://lautr3k.github.io/SLAcer.js/) was utilized. The slicing process yielded a zip-file containing the single images and a parameter file and was directly uploaded to the 3D printing software and thus used for the printing.

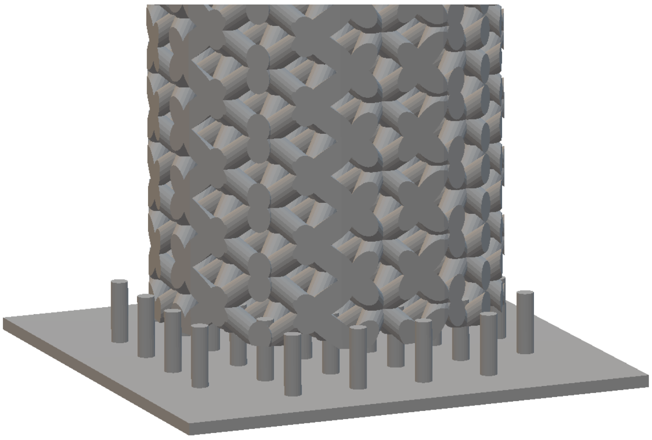

**Figure 4.1:** Support structure of a model of an open-cell structure consisting of the open-cell structure itself, vertical cylinders and a base plate.

### 4.1.4 Soxhlet extraction

After the 3D printing process, the polymer part was detached from the building plate and directly processed in the soxhlet extraction, if not stated otherwise. For this, 300 ml of acetone in a 500 ml round flask and a 100 ml soxhlet extractor (without thimble) were used. After extraction for 24 hours, the specimen was first dried at ambient temperature for 1 hour and then at 60 °C in a drying oven for another 24 hours.

### 4.1.5 Measurement of the thickness of a single layer in the 3D printing process

The thickness of a single layer can be assessed using the 3D printer. For this experiment, the desired shape was illuminated as usual in the printer with a smaller 70 x 70 mm resin vat and not using the building plate. After the light exposure, the resin was washed away with acetone and the thickness was measured.

## 4.2 Thermal treatments of polymers and carbons in a tubular furnace

For the conversion into activated carbon, the extracted polymer structures underwent a thermal treatment at different temperatures and atmospheres. These were conducted in a tubular quartz glass furnace. Before each treatment, the glass furnace was evacuated and refilled with nitrogen.

For the oxidation and $CO_2$ activation, the furnace was heated up under nitrogen ($10\,\mathrm{Nl\,h^{-1}}$) to the desired temperature with a rate of $10\,\mathrm{K\,min^{-1}}$ and held for 30 min, so that a thermal equilibrium can be reached. Thereafter, the gas supply was switched to synthetic air or $CO_2$ in the case of oxidation or activation, respectively. For small samples, a flow of $10\,\mathrm{Nl\,h^{-1}}$ and for larger monoliths and flow of $30\,\mathrm{Nl\,h^{-1}}$ was set.

The pyrolyzes were conducted in a nitrogen atmosphere at 900 °C for 15 min with a heating ramp of $3.3\,\mathrm{K\,min^{-1}}$. Regardless of the size of the specimen, a gas flow of $10\,\mathrm{Nl\,h^{-1}}$ was set.

## 4.3 Electric swing adsorption

For the testing of porous carbon adsorbents in the adsorption of hexane and the regeneration via electric heat-up, a small laboratory plant was constructed. Its flow chart is displayed in Figure 4.2.

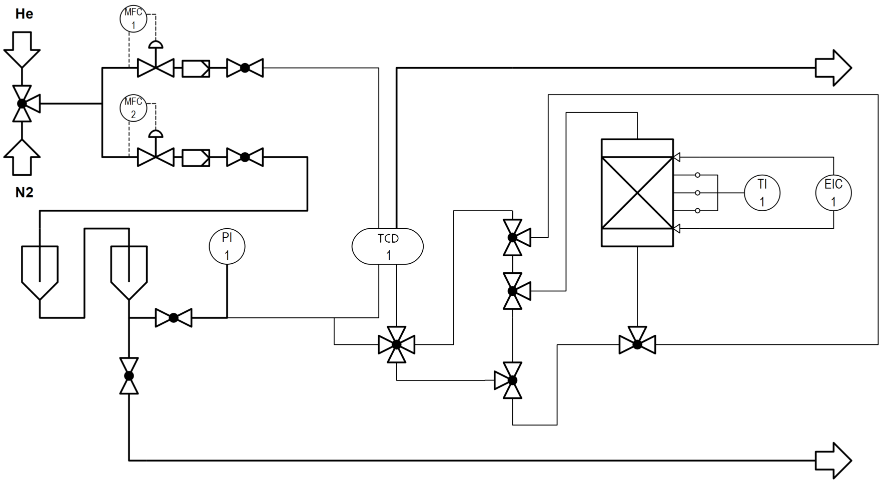

**Figure 4.2:** Folw chart of the electric swing adsorption laboratory plant.

The feed gas stream is saturated by two saturators connected in series. This gas stream is mixed with a dry gas stream in a t-junction, which allows for a broader window of operation of hexane concentrations. This feed is distributed by a four-way valve either directly or first through the adsorption cell and then to the thermal conductivity detector (TCD). Via a double jacket construction, the adsorption cell is tempered to 30 °C. The temperature can be measured at three different heights by thermocouples with a distance of 15 mm to each other. Furthermore, there are two inlets for electric wiring used for the resistive heating.

With the use of the valves H7 to H10, the flow direction in the adsorption cell can be changed. The ways of the gas stream, as shown in Figure 4.3.

The TCD signal, which is used for the evaluation,is calculated as the difference between the dry gas and the wet gas signal. Thus, it can account for small variations in the environmental temperature that impact the baseline threshold.

Adsorption experiments were conducted top-down, while the desorption was carried out countercurrently in a bottom-up manner.
In a typical series of subsequent adsorption and desorption experiments, the carbon material was placed in the adsorption cell and flushed with 10 ml min$^{-1}$ of nitrogen. In order to desorp water from the specimen, the material was heated up to 300 °C for 22 hours under a constant nitrogen gas flow of as well 10 ml min$^{-1}$. After switching off the electric heating and cooling down the adsorptive material, the feed gas was set to the desired hexane gas concentration. The vapor gas flow typically amounted to 10 ml min$^{-1}$. The TCD signal was left to stabilize for at least two hours, with the feed gas bypassing the adsorption cell. By turning the four-way valve, the hexane vapor was directed to the adsorption cell, starting the breakthrough experiment.

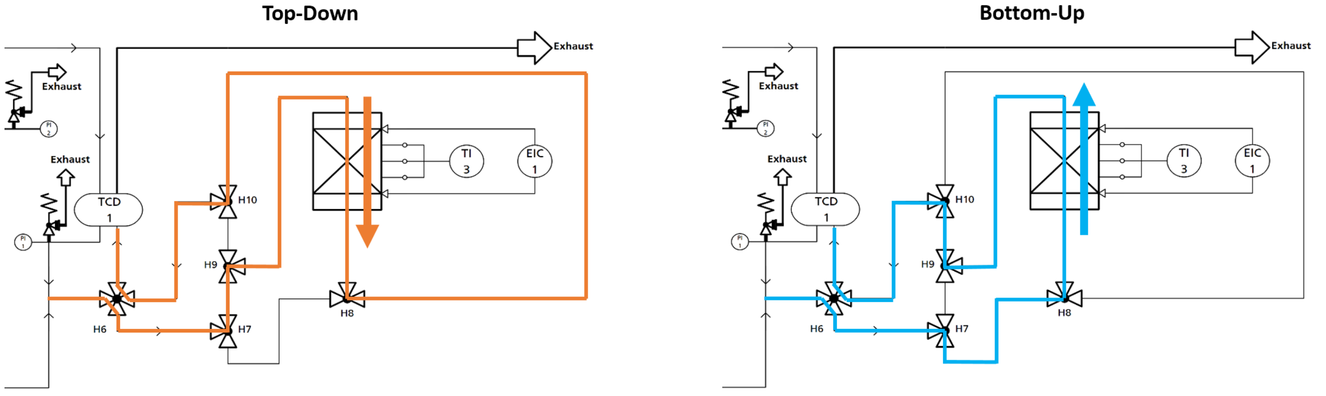

(a) (b)

**Figure 4.3:** Path of the gas flow in a top-down and bottom-up mode of operation.

Desorption was carried out with a constant nitrogen flow of 10 ml min$^{-1}$. After measuring the baseline signal of the dry gas bypassing the adsorption cell for one hour, the desorption started by a turn of the four-way valve. After five minutes, resistive heating was switched on and increased the temperature of the adsorptive material to 300 °C. The desorption was carried out for 22 hours, after which the heating was turned off.

From the breakthrough curves, several values were derived. The breakthrough time was defined as the time at which the measured mass flow of hexane exceeded 0.021 mg min$^{-1}$, which equals 1 % of the inlet value of the adsorption.

Before the adsorption, the gas concentration was measured by bypassing the saturated nitrogen gas through the TCD. From the difference of this value and the breakthrough curve, the adsorbed mass was calculated by integration. In order to get a better insight into the performance and pore structure of the carbon materials, two values were calculated. The apparent hexane density $\delta_{Hex,app}$ was calculated as the quotient of the adsorped hexane mass $m_{Hex}$ and the total pore volume of the adsorbent.

$$\delta_{Hex,app} = \frac{m_{Hex}}{v_{PV} \cdot m_{Carbon}} \tag{4.1}$$

The apparent hexane molecule's surface area $A_{Hex,app}$ was calculated from the adsorped mass and the total surface area of the adsorbent and converted to the value per molecule by using the molecular mass $M_{Hex}$ and the Avogadro constant $N_A$.

$$A_{Hex,app} = \frac{m_{Carbon} \cdot a_{SSA}}{m_{Hex}} \cdot \frac{M_{Hex}}{N_A} \tag{4.2}$$

### Infrared Spectroscopy

For the measurement of the conversion of vinyl groups, IR spectroscopy can be employed. A typical photoresin mixture, examined with this method, contained 50 vol% of the monomer either as a single substance or as a mixture of equal volumes of the monomers in the copolymerization. Additionally, 50 vol% of the porogen containing 10 mg $ml^{-1}_{total}$ BAPO was added to the monomer. For analysis, a layer of 10 $\mu$m of the liquid analyte was placed between two NaCl windows with a diameter of 3 cm. In order to evaluate the kinetics of the reaction, the crystal window - photoresin - assembly is alternatingly analyzed by IR spectroscopy and illuminated with the 3D printer for a given time.
For an IR measurement, the assembly is placed in the Bruker SuperIRMaster3000 and centered perpendicular to the light beam. Since the two crystal windows are not entirely parallel and the light beam is never perfectly in the center of the discs, four measurements in total, with a 90° rotation in between, were conducted in the wavenumber range of 500 to 4000 $cm^{-1}$.

For the accurate evaluation of the reaction, the frequency for quantitative measurement has to be carefully selected. The vinyl group vibrations can be observed at different wavenumber. A selection is shown in Figure 4.4. However, a suitable wavenumber has to fulfill the following requirements:

1. High peak intensity
2. No overlay with neighboring peaks or peaks from the other monomer or porogens
3. Vinyl peak should exhibit a reduction upon curing / Peak of the internal standard should not exhibit reduction upon curing

Since the thickness of the photoresin varies along the NaCl window, an internal standard was used to keep the standard deviation of the method low. As such, an adsorption peak of the porogens should be used, as this substance presumably does not participate in the polymerization. Around 744 $cm^{-1}$, both porogens, DEP and DIP, exhibit an absorption peak due to the ortho-substituted benzene ring. Therefore, the maximum between 720 and 770 $cm^{-1}$ was used as an internal standard.
For the choice of a suitable vinyl group absorption band, a decrease in adsorption after the curing needs to be observed. Between 3050 and 3100 $cm^{-1}$ $CH_2$ stretching occurs. Upon curing, a reduction in absorption can be observed. While this signal is moderate for DVB (3088 $cm^{-1}$), it is very week for PETA. Another frequency range often used is around 1630 $cm^{-1}$, at which C=C stretching can be observed. Upon curing, a substantial reduction in absorption occurred for both monomers. While DVB shows one peak at 1629 $cm^{-1}$, PETA exhibits two absorption peaks at 1635 and 1619 $cm^{-1}$. Due to this peak overlay, this frequency spectrum was not chosen for the quantitative evaluation. However, PETA exhibits a strong absorption at 1408 $cm^{-1}$, caused by $CH_2$ wagging of the acrylic vinyl group. Although for DVB, a small absorption peak at 1400 $cm^{-1}$ can be observed, there is no peak overlay. In contrast, the aromatic vinyl groups of DVB strongly absorb at 907 $cm^{-1}$ caused by $CH_2$ wagging. Neither PETA nor the porogens exhibit a peak at this frequency. In summary, the maximum between 1403 and 1420 $cm^{-1}$ subtracted by the minimum between 1410 and 1440 $cm^{-1}$ was used to calculate the concentration of acrylic vinyl group,

while the maximum intensity between 900 and 920 $\mathrm{cm}^{-1}$ accounts for the concentration of aromatic vinyl groups without further baseline correction [162].

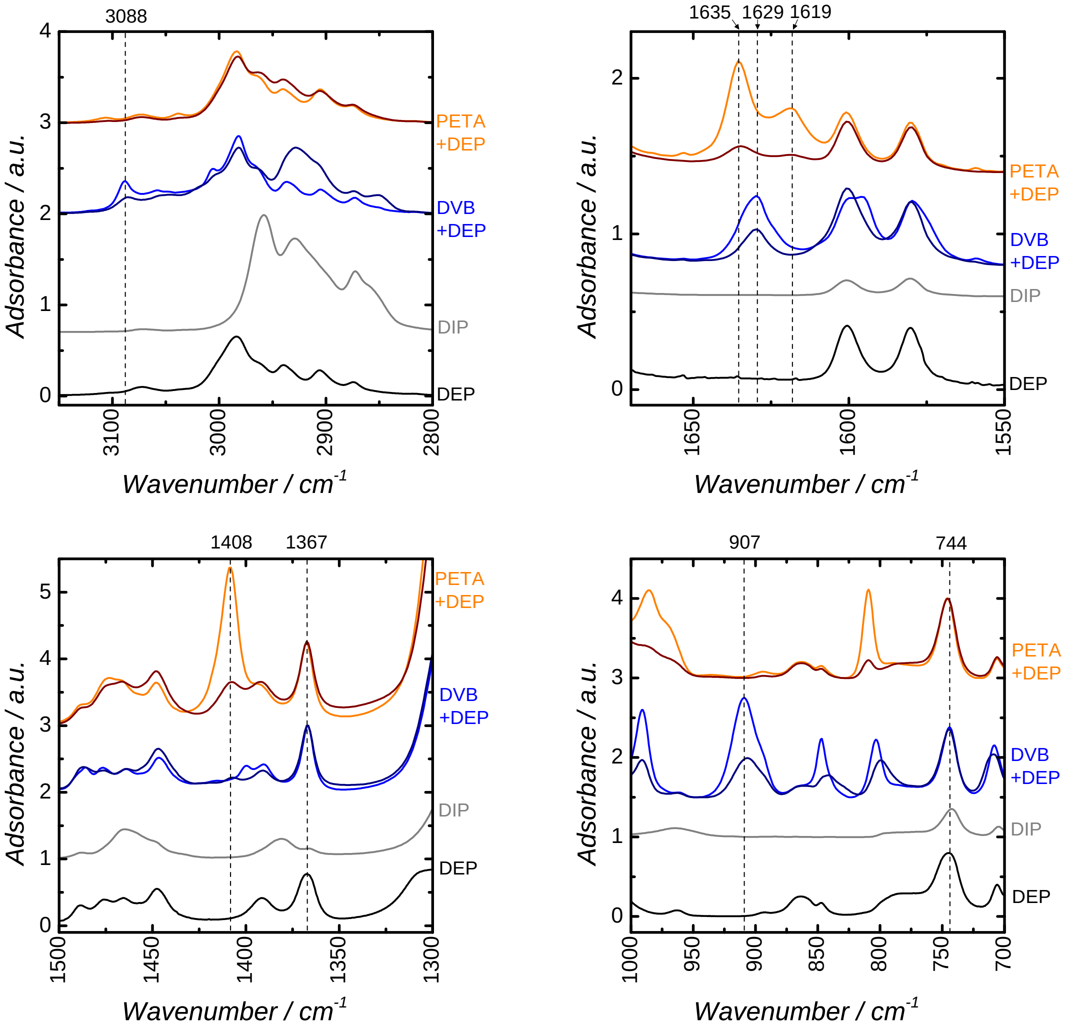

**Figure 4.4:** IR spectra of the porogens DEP and DIP, and 50 - 50 vol% mixtures of PETA or DVB with DEP and 10 mg $\mathrm{ml}^{-1}$ BAPO as photoinitiator before (bright orange or blue) and after curing for 50 min in the 3D printer (dark orange or blue).

It has to be noted that no actual numbers for the concentration were calculated, as the thickness of the layer of photoresin can hardly be measured accurately. Instead, the conversion $X$ was determined using the relative intensities $I$ for each time $t$ as shown in Equation 4.4.

$$\overline{I_{DVB,t}} = \frac{1}{4}\sum_{i=1}^{n=4} I_{DVB,t,i} \tag{4.3}$$

$$X_t = \frac{\overline{I_{DVB,t=0}} \cdot \overline{I_{DVB,t}}}{\overline{I_{DVB,t=0}}} \tag{4.4}$$

The standard error $\sigma$ for the conversion was calculated from the standard error for a normal distribution of the average intensity as follows.

$$\sigma_{I_t} = \frac{1}{\sqrt{n \cdot (n-1)}} \sum_{i=1}^{n=4} \left( I_{DVB,t,i} - \overline{I_{DVB,t}} \right) \tag{4.5}$$

$$\sigma_{X_t} = 1.96 \cdot X_t \cdot \left( \frac{\sigma_{I_t} - \sigma_{I_{t=0}}}{I_t - I_{t=0}} - \frac{\sigma_{t=0}}{I_{t=0}} \right) \tag{4.6}$$

### Thermogravimetry

Thermogravimetric analysis was conducted using a Netzsch „STA 409 PC Luxx” The analysis was carried out with a gas flow of 10 ml min$^{-1}$ of synthetic air or nitrogen in case of the TPO and TPD respectively. If not indicated otherwise, the samples were heated with a ramp of 5 K min$^{-1}$.

### Differential scanning calorimetry

The differential scanning calorimetry measurements were performed in a Mettler Toledo DSC-1 in a window of -80 to 240 °C using a heating ramp of 10 K min$^{-1}$. One measurement consisted of two consecutive cycles of heating with an intermediate cooling step.

### Scanning electron microscopy

Field-emission scanning electron microscopy images were taken using a Philips XL30 FEG with an acceleration potential of 30 kV.

### UV-Vis spectroscopy

Emission spectra were recorded using a Spectro 320 (D) R5 from Instrument Systems in a wavelength range of 350 to 800 nm. The light was collected with a standard optical fiber (OFG-322, Instrument systems) at a distance of 76 mm.

The transmission spectra were measured using a Perkin Elmer Lambda 900 UV/VIS/NIR spectrometer in a wavelength range of 200 to 600 nm. Ethanol served as a solvent.

### Mercury intrusion porosimetry

Mercury porosimetry was performed using a combined Pascal 140 and Pascal 440 from Thermo Scientific measuring in a range of 0.0125 to 400 MPa. Pore sizes were calculated using a cylindrical and slit pore model. In order to quantify the maximum pore size, the $d_{90}$ value was used. At this value, only 10 % of the pores are filled with mercury. For this evaluation method, pores in the range from 0 to 1500 nm were included, since larger pores are believed to be caused by interparticular space. The only exception from this was the polymer sample 30 vol% DButP, which exhibited many cracks in the surface and for which the included range was extended to 30000 nm in order to account for this.

### Nitrogen sorption analysis

Nitrogen sorption was conducted at the evaporation temperature of nitrogen of around 77 K using a Quantachrome Quadrasorp apparatus. The samples were outgassed for 20 hours at a temperature of 150 °C in case of the polymers or 350 °C in case of the carbons at a pressure of 14 mTorr. The polymer samples were analyzed by the BET method. The carbon samples were evaluated using a QSDFT model (slit/cylindric pore, QSDFT adsorption branch) instead. The micropore diameter was calculated for the microporous pressure range of 0 to 0.4 only.
In the $CO_2$ activation, the development of the specific surface area $a$ was extrapolated based on just the influence of the burn-off $\Delta m/m_0$.

$$a = a_0 \cdot \frac{1}{1 - \frac{\Delta m}{m_0}} \qquad (4.7)$$

### Thermographic measurements

Thermographic analysis was conducted using a FLIR ThermaCAMTM S65 measuring in a spectral range of 7.5 to 13 $\mu$m. From the infrared spectral data, the temperature was directly calculated by the camera.

# 5 Results and Discussions

## 5.1 Development of a suitable photoresin

A successful 3D printing process requires a photoresin that is firstly suitable for the stereolithographic 3D print and secondly yields polymers that can be converted into carbon while maintaining their macrostructure. In this chapter, different monomers will be examined in order to find a suitable combination that meets these demands.

### 5.1.1 Variation of the monomer composition using a simplified geometry

For the initial investigation of the solidification time, a pellet-shaped simplified geometry was chosen. In Figure 5.1, the solidification times of the four monomers, namely pentaerythritol tetraacrylate (PETA), 1,3,5-triallyl-1,3,5-triazine-2,4,6(1H,3H,5H)-trione (TTT), polyethylene glycol diacrylate (PEGDA) and divinylbenzene (DVB), in the homopolymerization as well as in the copolymerization with DVB, are shown. The pictures of the polymerized and extracted pellets are shown in the appendix in Figure 7.1 (p. 78).

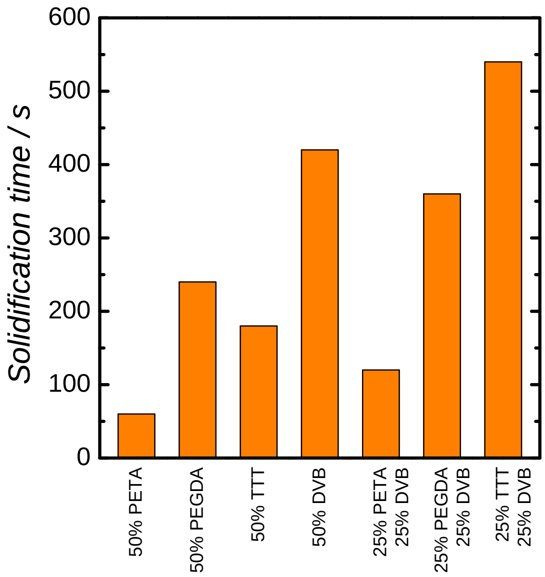

**Figure 5.1:** Solidification time of PETA, TTT, PEGDA and DVB in the homopolymerization and copolymerization with DVB using a simplified pellet geometry and a HPHg lamp for illumination, 10mg ml$^{-1}$ BAPO as initiator and 50 vol% DEP as porogen; (b) Pellet with 50 vol% PETA and 50 vol% DEP after polymerization and extraction of the porogen.

In the homopolymerization, PETA exhibited the quickest solidification time of 60 seconds. This is much faster than the other acrylate monomer PEGDA, which required 240 s for hardening. Due to the larger amount of acrylic functional groups of each monomer molecule (four instead of two), PETA needs a smaller degree of conversion for establishing a solid polymer network [148]. While TTT required 180 s for solidification, DVB took 420 s, which was by far the longest. The sluggish polymerization kinetics of DVB is due to the radical stabilization in the entire sp$^2$ hybridized system of the molecule. Using this duration for stereolithographic printing with a layer thickness of 40 $\mu$m, a lifting height of 4 mm, a platform speed of 4 mm $\text{min}^{-1}$ up and 50 mm $\text{min}^{-1}$ down, a single centimeter of vertical printing would need around 200 min as the following calculation shows. Thus, DVB alone is not suitable for high-resolution stereolithographic printing.

$$w_{Print} = \frac{1}{l} \cdot \frac{l}{h_{Layer}} \cdot \left( t_{Polymerization} + \frac{h_{Lift}}{w_{up}} + \frac{h_{Lift}}{w_{down}} \right) \tag{5.1}$$

$$w_{Print} = \frac{1}{1\,cm} \cdot \frac{1\,cm}{40\,\mu m} \cdot \left( 420\,s + \frac{4\,mm}{4\,mm\,min^{-1}} + \frac{4\,mm}{50\,mm\,min^{-1}} \right) = 202\,min\,cm^{-1} \tag{5.2}$$

In the case of the copolymerizations, the addition of an equivolumetric amount of DVB increased the solidification time of the other monomers. Similar to the homopolymerizations, PETA provided the shortest solidification times in the copolymerization as well. Like PETA, also the copolymerization with PEGDA allowed for a reduction of solidification time in comparison to the homopolymerization of DVB. However, the combination of DVB and TTT needed a longer time to solidify than each monomer in their homopolymerization. All experiments were conducted with the presence of 50 vol% DEP as a porogen in the resin mixture. Therefore, it is essential to note that the porogen could be extracted entirely by acetone in every experiment.

In order to examine the polymer's thermal stability, they were pyrolyzed in a nitrogen atmosphere with and without a prior stabilization in air. Figure 5.2 depicts the corresponding mass losses in these treatments.

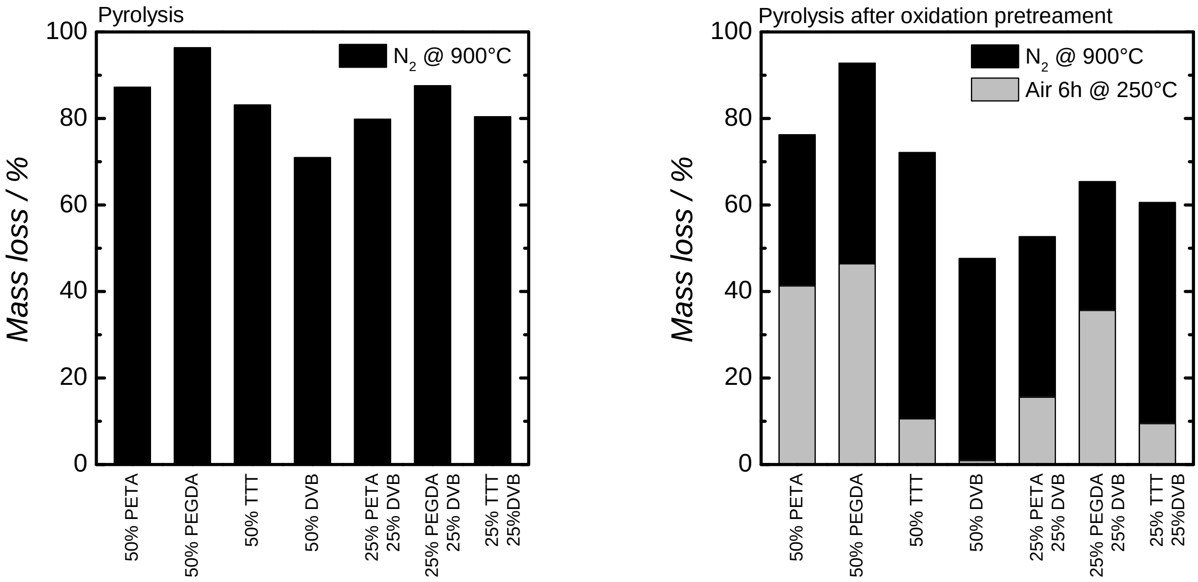

(a) (b)

**Figure 5.2:** Mass loss of polymerized PETA, TTT, PEGDA and DVB as homopolymer and copolymer with DVB upon different thermal treatments; (a): pyrolysis in $N_2$ at 900°C; (b): oxidation in synthetic air at 300°C for 6h and subsequent pyrolysis in $N_2$ at 900°C.

At first, the results of the pyrolysis without prior oxidation will be discussed. In the homopolymerizations, polyDVB exhibited the lowest mass loss of 71 %. PolyPETA and polyTTT have a similar mass loss of around 85 %, while polyPEGDA is nearly completely volatilized, with only 3.5 % of the mass left as carbon. The polyethylene glycol backbone exhibits a low thermal stability, which explains this observation [163]. The same instability has also been observed in the literature together with high degrees of shrinking and mass loss, and in combination with an undefined porosity without micropores of the carbon [161]. Through the addition of DVB, the mass loss of all copolymers decreased by 5 to 10 percentage points.
Among the many methods reported in the literature and summarized in chapter 2.2.1, oxidation in air was chosen as pretreatment. It readily combines with pyrolysis, does not include harmful chemicals and pore transport limitation is less likely to occur, since the speed of diffusion of gaseous oxygen is faster than for liquids such as molten sulfur or sulfuric acid. The acrylic homopolymers polyPETA and polyPEGDA both exhibited a high mass loss in the oxidation of 41 and 46 %, respectively. While the overall mass loss after the subsequent pyrolysis for polyPETA decreased by 10 percentage points, polyPEGDA experienced a reduction of 4 percentage points. This decrease can be explained by the low stability of the polyethylene backbone in air reported in the literature [163]. Although the mass loss of polyTTT in the oxidation was only 10 %, like polyPETA, its overall mass loss reduced by about 10 percentage points. In contrast, polyDVB was not affected by the oxidation in terms of its mass. However, a color change from white to brown, as observed for every other oxidized specimen, indicates the establishment of additional crosslinks and oxygen functionalities in the polymer. Through this treatment, the overall mass loss upon pyrolysis reduced to 48 %. The mass loss of the copolymers with DVB decreased in every case of oxidation, as well as for the overall values. Among them, poly(DVB-co-PETA) exhibited the highest thermal stability with a mass loss of 53 %.

The moderate solidification time of 120 seconds in combination with the high thermal stability of the polymer in the heat treatment, combines the distinct advantages of the acrylic PETA with the aromatic DVB and renders it as a promising candidate for a stereolithographicly printed polymer that can be transformed into carbon.

### 5.1.2 Copolymerization of DVB & PETA in a stereolithography printer setup

In order to investigate the speed of polymerization further and observe the influence of porogens, the photoresin was analyzed by IR spectroscopy during photopolymerization using the 3D printer setup.

In the investigation of the speed of polymerization, the conversion of vinyl groups of both monomers, DVB and PETA, was observed. Like in the 3D printing process, different phthalates were used as porogens. In Figure 5.3, the IR absorption spectra of the monomers and the two phthalates, namely diisodecyl phthalate and diethyl phthalate, are displayed. In order to calculate the vinyl group conversion, a suitable range of wavenumbers was carefully selected, as described in the methods in section 4.4.

Due to the difference of the aromatic vinyl groups of DVB compared to the acrylic vinyl groups of PETA, it was possible to observe their concentration at different wavenumbers at 907 and 1408 $\text{cm}^{-1}$ respectively. In Figure 5.4, the vinyl group absorption peaks during the homopolymerization of DVB and

PETA, as well as during copolymerization, are shown as a function of the illumination time in the 3D printer.

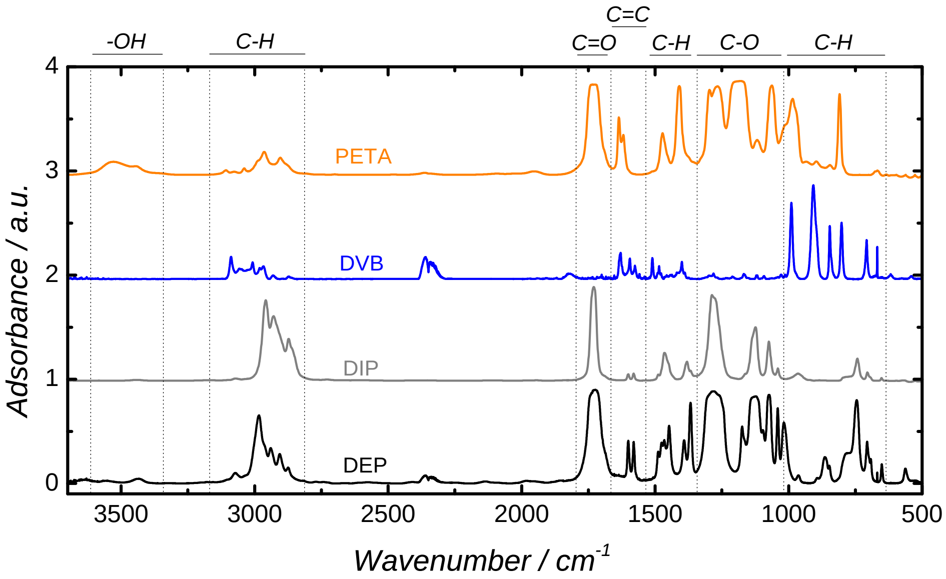

**Figure 5.3:** IR absorption spectra of the monomers divinylbenzene (DVB) pentaerythritol tetraacrylate (PETA), diethyl phthalate (DEP) and diisodecylphthalate (DIP).

For DVB, $CH_2$ wagging of the aromatic vinyl group resulted in strong absorption at 907 $cm^{-1}$. In contrast to DVB, which showed only a small absorption peak at 1400 $cm^{-1}$, PETA exhibited a high absorption peak around 1408 $cm^{-1}$ due to $CH_2$ scissoring that can be separated. In copolymerization, both peaks at 907 $cm^{-1}$ and 1408 $cm^{-1}$ can be evaluated and used for calculation of the conversion of both monomers' vinyl groups independently. Figure 5.5a displays the time-dependent progress of the conversion in homo- and copolymerizations. In the homopolymerization of DVB, after 12 min, only 20 % of conversion was achieved.

Similarly to the previous experiments with the HPHg lamp, the homopolymerization of PETA progressed much faster. A large fraction of its acrylic vinyl groups reacted after 15 s of illumination in the 3D printer. This measurement is more accurate than measuring the solidification time in the previous chapter by tabbing, which gave a value of 60 s. Unlike previously, in the newer experiment, oxygen was excluded from the reaction, since the two NaCl discs enclosed the photoresin. In copolymerization, both aromatic and acrylic vinyl groups reacted with a similar rate. The degree of conversion plateaued at 70 and 65 %, respectively.

In this series of experiments, also the influence of the porogen was evaluated, since it is required to introduce porosity. The results are shown in Figure 5.5b. Changing from 50 % DEP to 50 % DIP did not impact the initial reaction rate. Nevertheless, the reaction rate dropped already after 20 %, rather than after 50 % as for DEP. The final conversion after 300 s amounted to 57 % for aromatic and 52 % for acrylic vinyl groups.

DVB and PETA showed vastly different reaction rates in the homopolymerization. In contrast, during the copolymerization, they exhibit a similar rate of consumtion of their vinyl groups. This is a strong hint that a true copolymerization takes place. Although there is no investigation for DVB and PETA in the literature, the copolymerization of styrene and tert-butyl acrylate is randomly copolymerized [164]. This observation supports the finding of a drastic increase in thermal stability observed in the previous chapter 5.1.1. Therefore, an equivolumetric combination of DVB and PETA was used for further experiments.

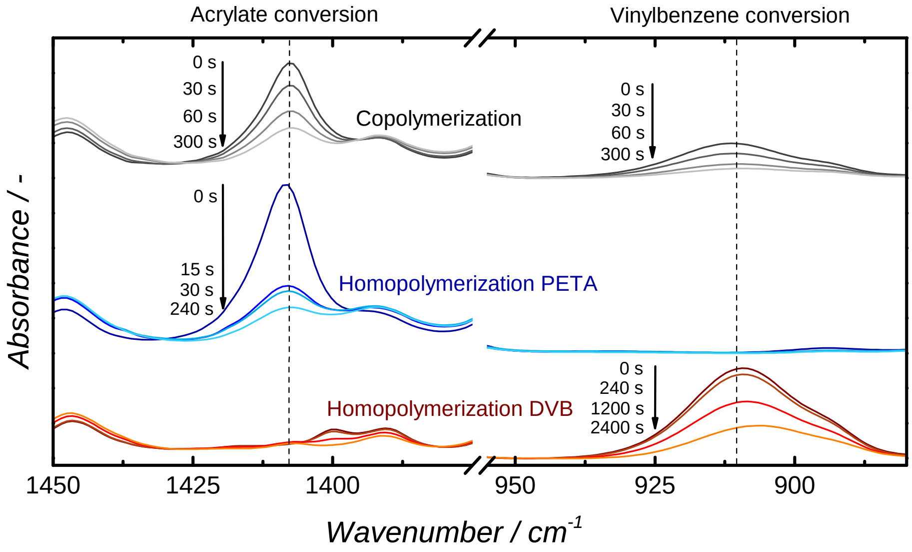

**Figure 5.4:** IR absorption of the co- and homopolymerization of DVB and PETA containing 50 vol% monomer (equal volumina in case of the copolymerization), 50 vol% DEP and 10 mg ml$^{-1}$ BAPO after different times in the 3D printer and after additional 30 min illumination under a HPHg lamp.

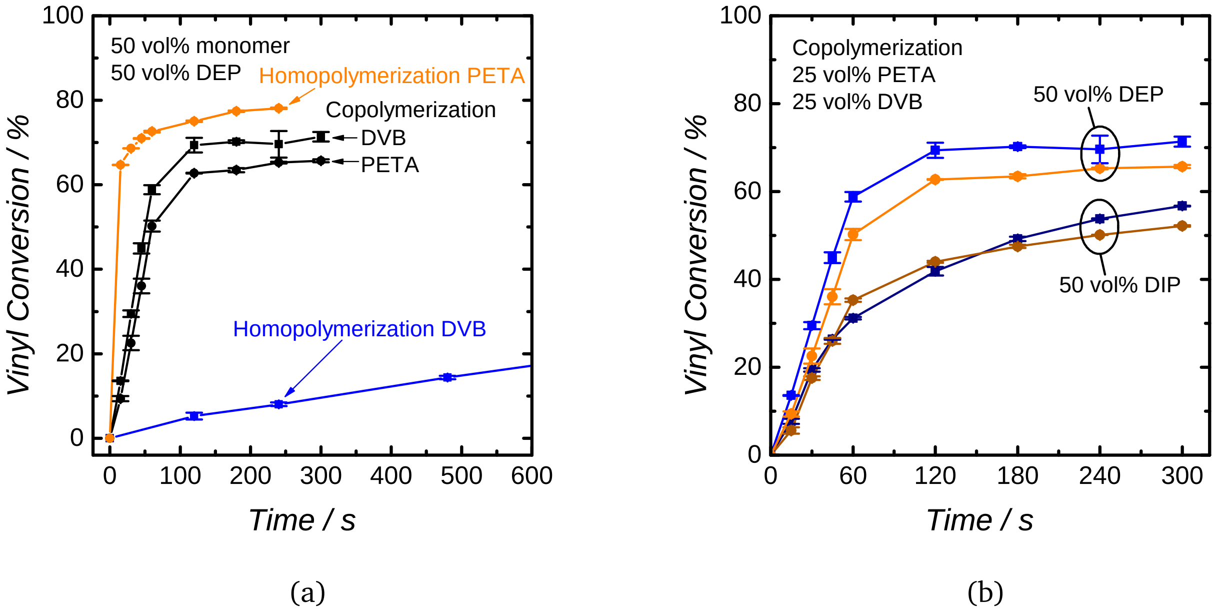

**Figure 5.5:** Conversion of aromatic (squares) and acrylic (circles) vinyl groups as a function of illumination time in the 3D printer; (a): homopolymerizations of DVB and PETA, and copolymerization of DVB together with an equal volume of PETA; (b): Variation of the porogen in the copolymerization of DVB and PETA.

## 5.2 Tailoring the meso- and macrostructure

From the literature, it is known that a porogen can be used to incorporate a second continuous phase during photopolymerization, which yields pores upon extraction. These pore are crucial for facilitating mass transfer during oxidative stabilization and CO2 activation on the one hand and for the application of a microporous carbon on the other hand. The suitable size and volume fraction of these pores depend on the respective application. Therefore, it is crucial to tailor these pore sizes and content via a systematic approach.

### 5.2.1 Influence of the porogen on additional meso- and macroporosity

In the literature, many different porogens, such as solvents like hexane or acetone, or higher molecular weight compounds such as phthalates or adipinates, were utilized as porogens. Phthalates are used as a softener for plastics and are therefore commercially available with different alcoholic substituents. In these experiments, the following linear or cyclic aliphatic, as well as aromatic substituents, were used:

- Diisodecyl phthalate (DIP)
- Dioctyl phthalate (DOctP)
- Dibutyl phthalate (DButP)
- Dicylclohexyl phthalate (DCyP)
- Benzyl butyl phthalate (BeButP)

In this series of experiments, a simple open-cell structure comprised of a 2x2x2 array of cubic body-centered unit cells served as a test structure for the 3D printing. Cylinders on the top of this structure connect them to the base plate and provide an easy detachment without destroying the specimen by functioning as predetermined breaking points. Figure 5.6 displays the 3D structure of the unit cell, the array, and the prepared specimen for each porogen.

Open-cell structures manufactured using the phthalates with cyclic substituents like DCyP or BeButP, or with a short linear substituent like DButP, suffered from low macroscopic accuracy in printing and occasional structural collapse upon extraction or subsequent drying. Their surface looked chippy and cracks traversed the solid material. Furthermore, the mechanical stability was poor, so these specimen had to be handled with great care in order not to break pieces off from the sample. In contrast, using 20 - 30 % DIP or 30 % DOctP as porogen delivered solid macrostructures. 20 % DIP and 30 % DOctP exhibited a slight yellow tone, which indicates that the soxhlet extraction did not remove all of the dye despite the 24 hours long operation. At the top of these specimens, which are displayed in the pictures in the same orientation as they were printed, small splinters emerged upon drying after extraction. These splinters are likely to originate from an incompletely polymerized gelly phase at the top of the printed layers. Through a gradient in crosslinking, these parts experienced size reduction upon drying, which resulted in bending and detachment. Using 30 % DIP instead, the extracted and dried specimen had a white color, which indicates a complete extraction of the dye. Furthermore, splinters on the surface appeared only at the very top and to a smaller extent compared to 30 vol% DOctP or 20 vol% DIP. However, after drying, some layers of the printed part separated from each other, which indicates an incompletely photopolymerized phase between the layers.

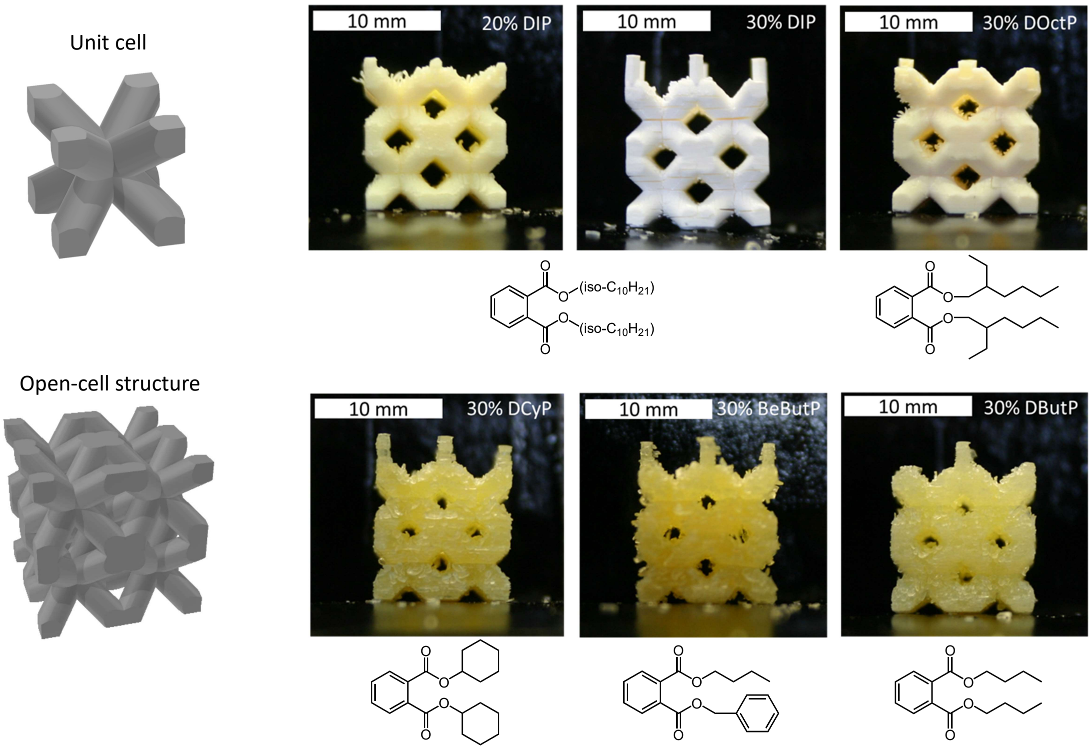

**Figure 5.6:** Left: Cubic body-centered unit cell and the from this derived 2x2x2 open-cell structure; right: 3D printed specimen using different phthalates as porogen made from a resin containing equal volumes of PETA and DVB, and the displayed content of porogen together with 0.4 mg ml$^{-1}$ sudan1 as a dye and 10 mg ml$^{-1}$ as initiator.

Apart from these successfully printed specimens, not all resin formulations proved suitable. When increasing the porogen content further to 50 % DIP, the layer separation occurred even during 3D printing. This effect results when the adhering force of two consecutive polymer layers is weaker than the force of detachment of the just printed layer from the resin vat. Although a proof cannot be delivered, this might be due to the formation of a monomer scarce porogen film between the polymer layers. Because of early phase separation, the porogen might migrate to the surface and act as a separator to the next printed layer

When using phthalates with very short alkyl chains like 50 vol% DEP, the structure broke apart upon drying after extraction of the porogen. This negative outcome is believed to be caused by the too high surface tension of micropores in the material. In the literature, it is known that this can be circumvented by an extraction using supercritical $CO_2$, a method that decreases the mechanical stress on the material during the drying procedure, as the $CO_2$ gradually turns from the supercritical to the gaseous state upon pressure release [165].

In order to quantify the pore structure of the printed parts, mercury intrusion porosimetry and nitrogen sorption analysis were conducted. The results of the variation of the phthalate's alkyl chain length are shown in Figure 5.7 and the results of the phthalate concentration variation are displayed in Figure 5.8. Table 5.1 lists the values of the specific surface area and maximum pore diameter.

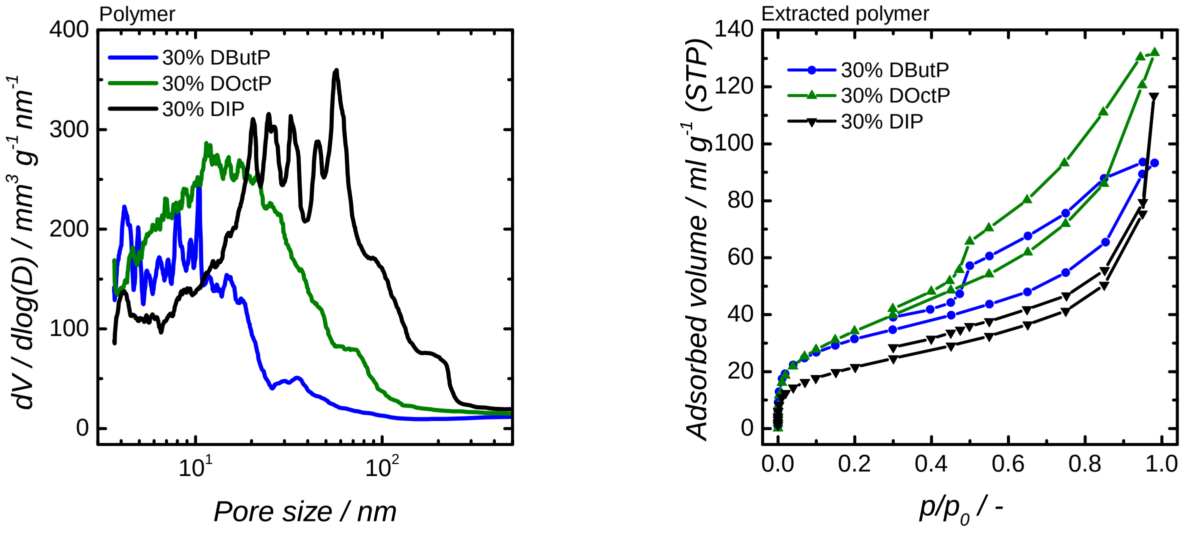

(a)

(b)

**Figure 5.7:** Pore analysis of extracted 3D printed polymers produced with different porogens; (a): Differential volume distribution from mercury intrusion porosimetry; (b): $N_2$ sorption isotherms.

**Table 5.1:** BET calculated specific surface area (SSA) and maximum pore diameter (10 % Hg intrusion) of extracted 3D printed polymers printed using different phthalates as porogen.

| Porogen | $N_2$ adsorption | Hg porosimetry |
|---|---|---|
| | $a_{SSA,BET}$ /$m^2g^{-1}$ | $d_{90\%}$ /nm |
| 20 vol% DIP | 64 | 30 |
| 30 vol% DIP | 77 | 156 |
| 30 vol% DOctP | 125 | 81 |
| 30 vol% DButP | 112 | 52 |

At first, it needs to be stated that although the $N_2$ sorption analysis parameters such as equilibrium time, etc. were optimized, it was not possible to fully close the hysteresis between ad- and desorption in the analysis of the polymers. This phenomenon is believed to be caused by pore mouths in the size of moleculare sieves in the analyte that can be penetrated by the $N_2$ molecule only at higher pressures. Therefore, the adsorption isotherm in the micropore region underrepresents the actual equilibrium values. Due to the narrowness of these pore mouths, the desorption takes place at very low pressures that are reached only during the evacuation at the beginning of each measurement and not during the desorption measurement [166].

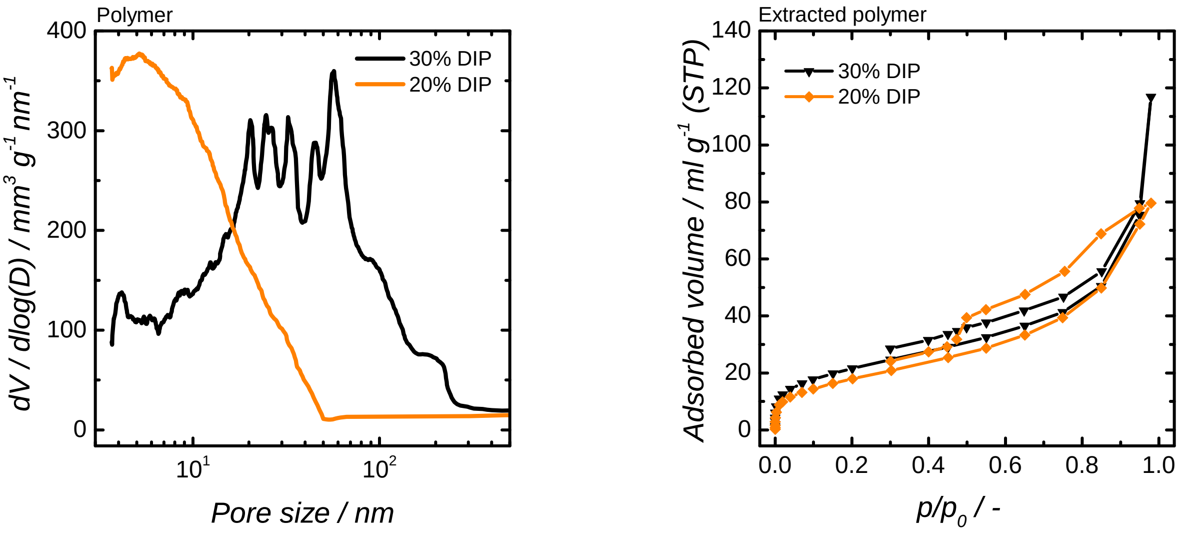

(a) (b)

**Figure 5.8:** Pore analysis of extracted 3D printed polymers produced with different concentrations of DIP; (a): Differential volume distribution from mercury intrusion porosimetry; (b): $N_2$ adsorption isotherms.

At first, the impact of the variation of the alkyl chain length on the pore structure will be discussed. Regarding the results from the Hg porosimetry, using 30 vol% DIP as a porogen caused the formation of the largest pores. Its maximum (90 %) pore diameter was 156 nm instead of 81 nm as for 30 vol% DOctP or 52 nm as for 30 vol% DButP. In the $N_2$ sorption, the 30 vol% DIP specimen exhibited mostly macropores, which cause a sharp increase of the adsorption towards the ambient pressure ($p/p_0 = 1$) and the absence of a hysteresis in the $N_2$ sorption analysis. On the contrary, the polymers templated with DOctP or DButP showed a hysteresis loop that prooved the presence of mesopores. Thus, these samples exhibited a specific surface area of 125 and 112 $m^2g^{-1}$, respectively. Using 30 vol% DIP resulted in a smaller SSA of 77 $m^2g^{-1}$. Altogether, the increase of the chain length of the parent alcohol of the phthalate caused the formation of pores with a larger diameter and a smaller specific surface area.

In an application, not only the size but also the volume fraction of pores might need to be adjusted. In this series of tests, the DIP volume fraction in the photoresin was varied from 20 to 30 %. The Hg porosimetry analysis showed much smaller pores with a maximum diameter of 30 nm in case of 20 vol% DIP as a porogen, which is even smaller than for 30 vol% DButP. The presence of mesopores was also confirmed through $N_2$ sorption, in which a clear hysteresis loop is visible. Due to the overall smaller volume content of pores, the specific surface area is the lowest of all the polymer specimens measured. In summary, it can be concluded that a more substantial volume content of the porogen leads towards larger pores being formed through liquid porogen templating. Although, the DIP content could not be raised from 30 to 50 vol% and still successfully printed, an increase of the pore volume might be possible using a different porogen with a shorter substituent like DOctP or DButP.

In porogen templating, the point of time at which the phase separation occurs defines the size of the porogen domains in the polymer and, therefore, the pores size distribution after extraction as was described in chapter 2.2.3. In the case of late phase separation, due to a low porogen content or a high solubility, only small porogen domains are formed as the diffusivity is limited by the large degree of crosslinks. In the case of a high porogen content or a less soluble porogen, the porogen is more mobile as the degree of crosslinks is smaller.
The conducted experiments confirm these causal relationships also in lithographic 3D printing. A lower content of DIP resulted in smaller pores. Although the solubility of the porogen was not measured in this work, the measured pore sizes conclude that the solubility decreases with a longer alkyl chain. This observation is according to findings in the literature in which the longer chain phthalates resulted in larger pores in a glycidyl methacrylate - ethylene glycol dimethacrylate - copolymer [167].

### 5.2.2 3D print resolution in z-direction

Lithographic 3D printing relies on the sequential photopolymerization of single layers of photoresin. Since the projector's light penetrates the resin vat from below, the light could traverse the whole liquid holdup from bottom to the top, causing it to polymerize. The photoinitiator's absorption capacity is not sufficient to decrease the intensity. Instead, another dye, solely for the purpose to limit the light penetration depth, has to be added to the photoresin. Sudan1, a well-known color agent in 3D printing, can adsorb all light that is utilized for the photopolymerization, which is mainly at wavelengths between 400 and 420 nm. Figure 5.9a displays the absorption spectra of the initiator and the dye, as well as the emission spectra of the projector.

Due to an ultraviolet and infrared filter that is used to protect the end-user outside and the DLP chip inside the projector, the emission spectrum is limited to a range of 400 to 730 nm. During the printing, a heat-up of the resin occurred, stemming from the high light intensity and the large absorbed fraction. The heat energy penetrated the resin at the bottom of the vat, as a significant fraction of the light is absorbed in the first few hundred micrometers by the dye. The change in temperature caused the convection of the photoresin at the illuminated spots during the print that distort the shape of single polymerized layers (see appendix Figure 7.3 for the images). Therefore, a blue light glass filter (Schott BG-25) was introduced in the light path between projector and resin vat, which effectively limited the distortion caused by the convection, especially for larger illuminated areas. The filter also reduced the speed of polymerization, which is either due to the overall lower light intensity or due to the lower temperature (see appendix 7.4 for the vinyl conversion graph). The final conversion, however, remained unaffected.

As there is a high concentration of radical inhibitors in the photoresin (350 ppm p-tert-butylcatechol and 100 ppm monomethyl ether hydroquinone), a distinct amount of radiation is needed for polymerization. This dosage is called $E_{Poly}$. Since the dye absorbs the projector's light in the resin, its intensity decreases according to the Beer-Lambert law (see Equation 5.3). After a certain pathlength $d_{Layer}$, ideally, there should not be a sufficient intensity for the given polymerization time (see Equation 5.4). Thus, a layer of a distinct thickness polymerizes.

$$E_{Poly} = d_{Layer} \cdot (\epsilon_{Sudan1} \cdot c_{Sudan1} \cdot \epsilon_{BAPO} \cdot c_{BAPO}) \tag{5.3}$$

$$d_{Layer} = \frac{\frac{E_{Poly}}{\epsilon_{Sudan1}}}{c_{Sudan1} + \frac{\epsilon_{Sudan1}}{\epsilon_{BAPO}} \cdot c_{BAPO}} \tag{5.4}$$

In stereolithography, the platform is elevated after each polymerization by a particular value called step height. Thus, in the 3D printing process, the layer thickness and the step height have to be matched. Is the step height entered in the software too large, the interconnection between the layers will be too weak and they will detach from each other during the print. If the step height is too small, the printing takes longer than needed and resolution for the printing of voids is lost. Furthermore, resin aging is too fast. Therefore, the dye concentration has to be adjusted to the layer height or vice versa.

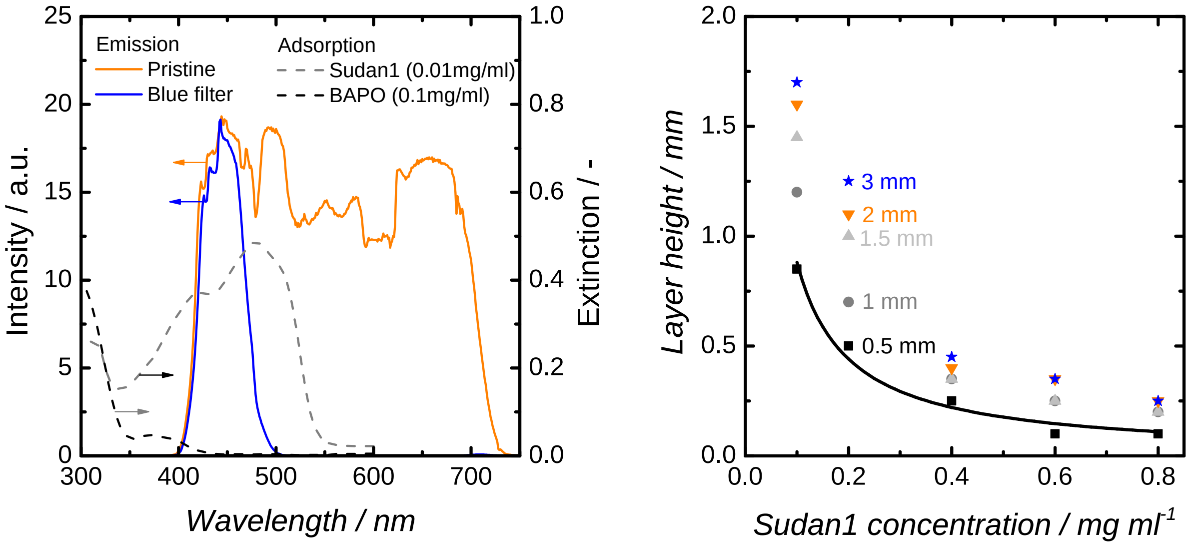

(a)

(b)

**Figure 5.9:** (a): Emission spectrum of the 3D printers projector in pristine condition and after the installation of a blue light filter and absorption spectrum of the photoinitiator BAPO and the color agent sudan1; (b): Measured height of a polymer layer created by illumination of the photoresin for 120 s using a blue light filter varying the dye sudan1 concentration and the width of the illuminated rectangle of 20 mm length.

In Figure 5.9b, the single-layer height as a function of the sudan1 concentration and the width of the illuminated area in the form of a rectangle with a length of 20 mm is shown. In the case of the smallest width of 0.5 mm, the height followed the Beer-Lambert law. With an increased size of the illuminated area, firstly, the thickness of the layers increased, while the dye concentration was not changed. Secondly, the Beer-Lambert law did not fit the data points anymore. This discrepancy is due to many factors of non-ideal behavior, impacting the results of this experiment. In the case of larger illuminated areas, heat builds up and will cause oligomers and radicals to ascend. In the case of small illuminated areas, diffusion can take place and causes radicals and oligomers to dissipate, so a crosslinked polymer cannot form in the given time. Nevertheless, in the final printing process, after multiple layers, also other factors have to be considered. Then, there is already the building plate or the previously polymerized layer above the illuminated photoresin hindering convection. Furthermore, in the middle of a larger structure, the temperature might be elevated, which causes the layers to be thicker.

Figure 5.10 displays polymer spirals of different thread diameters. They were printed using a step height of 40 $\mu$m in combination with a dye concentration of 0.8 mg ml$^{-1}$, which is much less than the 100 $\mu$m measured in the single-layer experiment. In the case of a larger step height of 60 $\mu$m, the smallest spiral with a thread diameter of only 200 $\mu$m could not be printed. The reason is that especially with regard to small diameters, diffusion takes place and the little heat introduced by the light cannot raise the temperature causing the polymerization reaction to accelerate like for a larger illuminated area. The needed step height is also smaller since a certain amount of overlap is necessary with regards to the solidity of the printed layer.

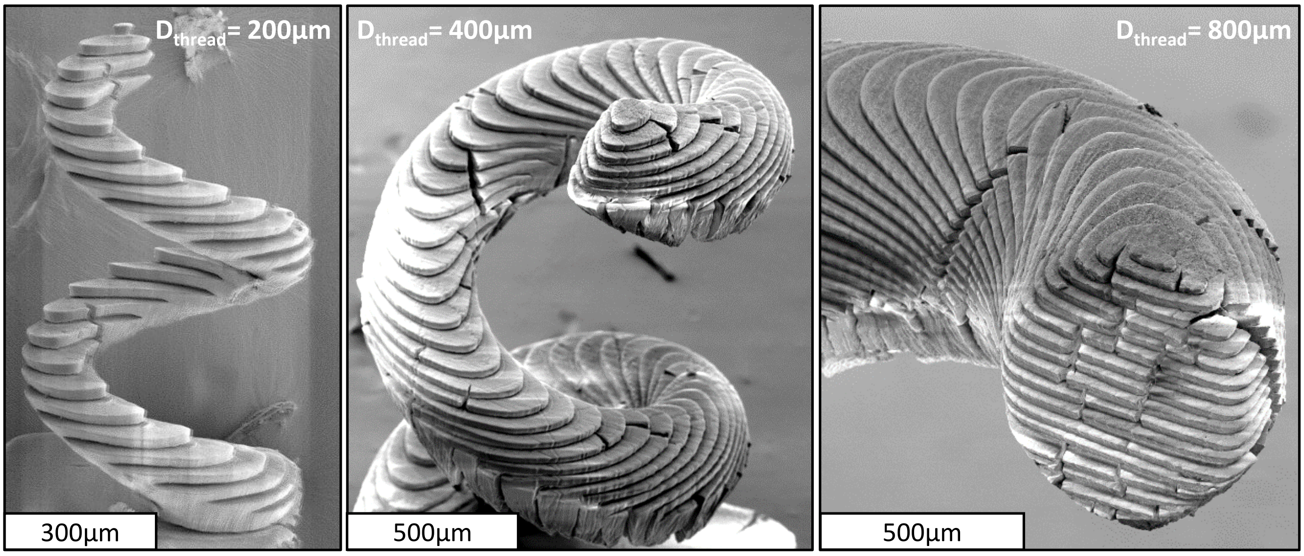

**Figure 5.10:** SEM images of 3D printed spirals using a photoresin comprised of 30 vol% DOctP, 35 vol% DVB, 35 vol% PETA, 10 mg ml$^{-1}$ BAPO and a dye concentration of 0.8 mg ml$^{-1}$ at a layer height of 40 $\mu$m and an illumination time of 120 s.

The thread diameter written in the pictures represents the dimension in the CAD file. However, after extraction of the porogen and drying, the diameter of the spirals changed. The spirals' diameter of 200, 400 and 800 $\mu$m decreased to 140, 336 and 707 $\mu$m respectively. This deviation is percent wise most prominent in the case of the smallest spiral. As a smaller spiral with a thread diameter of 100 $\mu$m was not successfully printed, likely, the oligomers and radicals dissipate away from the illuminated area. Thus, the area of each solidified layer is smaller than the illuminated area. Furthermore, it is known that lithographically printed polymers decrease in size upon post-curing, which might be conducted through the elevated temperatures during the soxhlet extraction. Although there were cracks in the polymer spirals as the SEM images show, the structures were sound, supported their weight and could be handled without special care. The printing time amounted to 77 min cm$^{-1}$.

Figure 5.11 displays polymer spirals of different thread diameters that were printed using a step height of 500 $\mu$m and a low dye concentration of 0.1 mg ml$^{-1}$. In the single-layer experiment, a thickness of 1.7 mm (in case of 3 mm projection width) was measured for this condition. With an increased layer height of 750 $\mu$m, the smallest spiral (d = 2 mm) could not be printed. It was observed, that on the side facing the building plate, at which the platform at the lower end of the spiral attached, the surface of the polymer became chippy upon drying after the extraction. This behavior was already observed in the case of the open-cell structures for the porogen variation (0.4 mg ml$^{-1}$ sudan1) but to a much smaller degree. Due to the more considerable layer height, the printing time reduced to 6.16 min cm$^{-1}$.

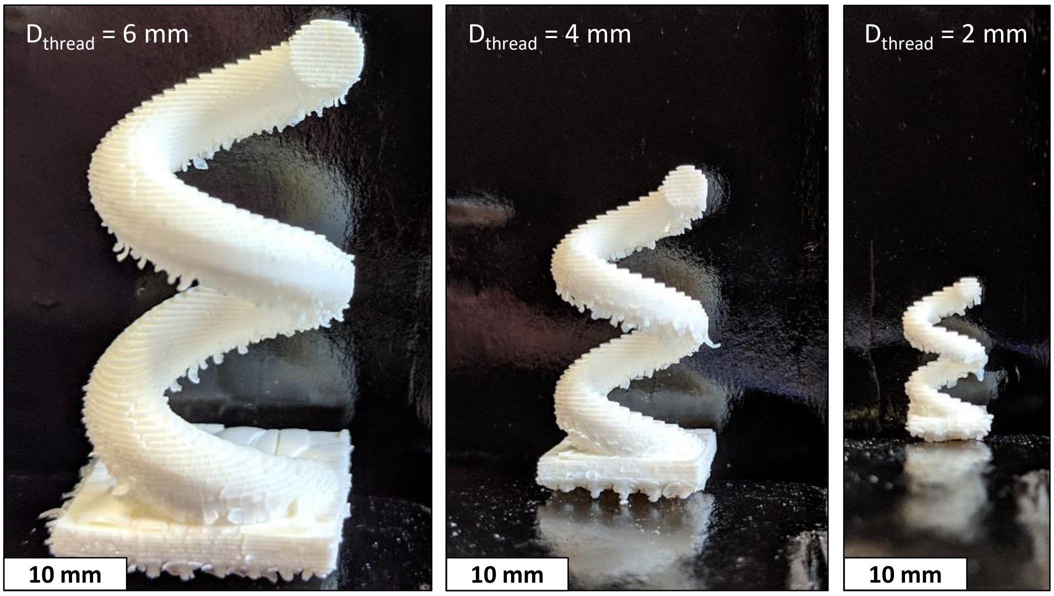

**Figure 5.11:** 3D printed spirals using a photoresin comprised of 30 vol% DOctP, 35 vol% DVB, 35 vol% PETA, 10 mg ml$^{-1}$ BAPO and a dye concentration of 0.1 mg ml$^{-1}$ at a layer height of 500 $\mu$m.

In summary, these experiments show how to tailor the 3D printed polymer in terms of their meso- and macrostructure. By variation of the dye concentration, the accuracy and printing speed of the process can be changed. Using a high dye concentration, on the one hand, the printing of very detailed parts with a high resolution was possible expressing single features down to 20 $\mu$m. Utilizing a low dye concentration, on the other hand, made it possible to rapid prototype large structures at a high printing speed. The variation of the porogen type and its volume content in the photo resin allowed the introduction of pores in the meso- and macroporous regime. This new way opens a wide range of possibilities like porous functional polymers or post-functionalization for catalysis or adsorption.

Chapter 5.1.1 showed that stabilization in air before the pyrolysis, can reduce the mass loss during the pyrolysis. Here, the impact of the conditions on the carbon properties will be examined further.

### 5.3.1 Oxidation for stabilization of the macrostructure

Figure 5.12a displays the TPO curves of the polymers that illustrate the underlying processes in their oxidation. When using a constant heating ramp of 5 K $\text{min}^{-1}$, the extracted and dried polymer underwent different stages. Between 130 and 200 °C, the mass increased by 2 %. In this range, oxygen adds to the polymer into stable surface groups. With increasing temperature, the mass of the polymer reduced due to further oxidation and partial release into the gas phase. However, the rate of this mass loss decreased until a temperature of around 350 °C and a corresponding mass loss of 55 %. Only by a further increase in temperature (onset at 396 °C) the residual is oxidized at a higher rate.

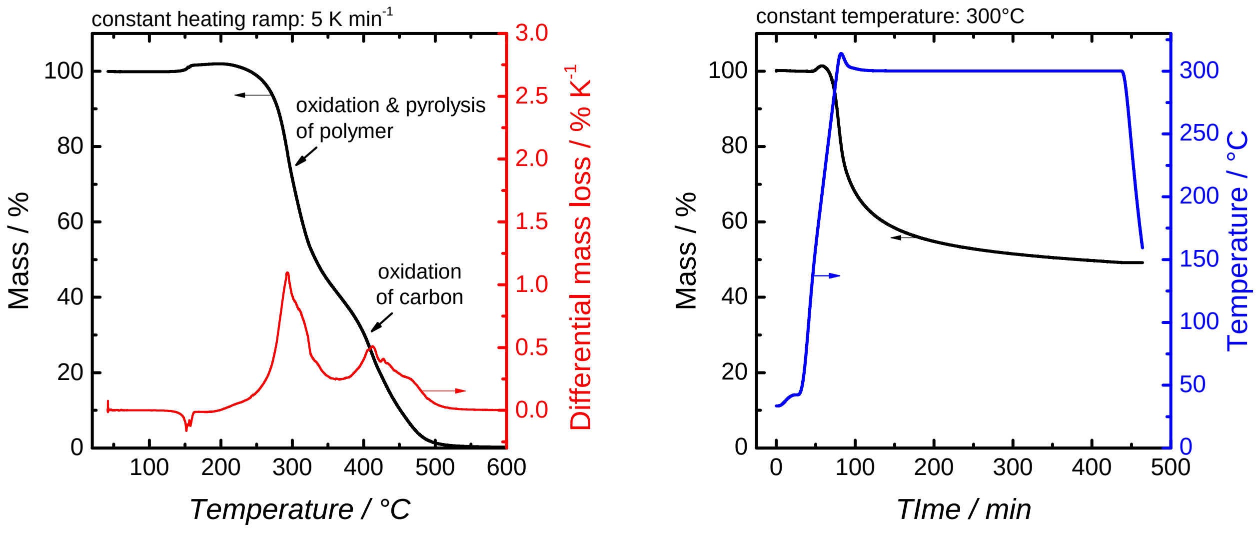

(a) (b)

**Figure 5.12:** TPO measurements in air of 3D printed polymer produced from a resin containing 35 vol% PETA, 35 vol% DVB and 30 vol% DIP; (a): Oxidation with a ramp of 5 K $\text{min}^{-1}$; (b): Oxidation at 300 °C for 6 hours after heating up with 10 K $\text{min}^{-1}$.

These results indicate a structural change in the polymer upon the oxidation until 350 °C, enhancing thermal stability. Through oxidation and dehydrogenation, the polymer converts into an early form of an oxygen-rich carbon species. Taking into account findings from the literature, an onset temperature of around 350 to 400 °C can occur among amorphous carbons [168]. Instead of oxidizing at a high temperature for a short time, treatment at a lower temperature for a longer time is preferable, in order to decrease the impact of pore diffusion limitation.

Figure 5.12(b) presents the TPO of the polymer at 300 °C for 6 hours. After the slight increase of mass at lower temperatures during the heat-up period, the mass quickly decreased through oxidation of the polymer (33 % in 30 min). The final loss in the TPO procedure amounts to 50 %. This is about the value

at which the rate of mass loss in the TPO with constant heating sharply decreased, indicating a change in the polymer structure towards a carbonaceous material. Thus, oxidation at 300 °C for 6 hours is a viable way to stabilize the polymer before pyrolysis.
This oxidation temperature is higher than in chapter 5.1.1. However, in these initial experiments, an uncalibrated muffle furnace was used. There, the real temperature is likely to differ from the set value. In contrast to that, the temperature values in the calibrated TG are considered to be accurate.

In order to convert the oxidized polymers into carbon, pyrolysis at 900 °C in a nitrogen atmosphere was conducted. Figure 5.13 shows the TG curves of differently oxidized polymers in comparison with a pristine as extracted sample. Furthermore, it contains images of the pristine extracted polymer (30 vol% DOctP) and the pyrolyzed samples with different pretreatments. During pyrolysis, the non-oxidized sample lost 80 % of its mass. This decrease is similar to experiments using pellet geometry. Due to the rapid mass loss and the absence of additional crosslinks without an oxidation pretreatment, the sample cannot maintain its structural integrity. The surface looks molten and chippy with bubble-like structures. Nevertheless, the size reduction of 45 % is still smaller than reported in the literature [161]. The oxidation at 200 °C increased the mass of the polymer by 8 % through the addition of oxygen surface groups. Therefore, despite the higher mass loss of 82 % in the pyrolysis, the overall mass loss was unaffected amounting to 80 %. Although the shrinking reduced to 40 %, the surface of the OCS looks chippy and course similar to the sample that was pyrolyzed without stabilization. The oxidation at 300 °C decreased the mass by 44 %. With the additional mass loss of 40 % in the pyrolysis, the total mass loss amounted to 67 %. Through the oxidation pretreatment, the shape of the open-cell structure was retained well throughout the process. The size reduction amounted to 35 % in each direction.

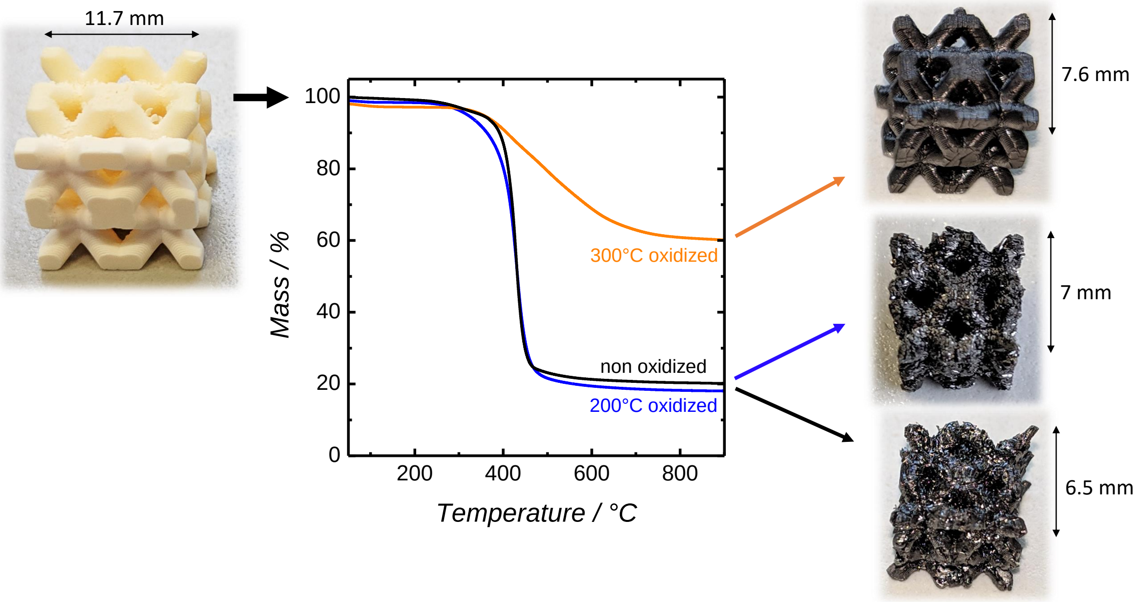

**Figure 5.13:** TG measurements of differently in a tubular furnace oxidized polymers (35 vol% PETA, 35 vol% DVB and 30 vol% DIP) and images of the pristine polymer made with 30 vol% DOctP as porogens and the through different oxidations with subsequent pyrolysis (prepared in a tubular furnace) prepared carbon materials.

It has to be mentioned that when using 30 vol% DIP as a porogen, layer separation occurred frequently. At first, the layers of the printed object seemed to be conjunct. Still, during the oxidation and pyrolysis, the additional mechanical stress through shrinking of the material seems to be sufficient to separate some layers of the open-cell structure. A DSC analysis of the extracted polymer was conducted to investigate, if post-curing is possible. The results are shown in Figure 5.14(a). The first run shows the presence of exothermal reactions occurring in the range between 150 and 240 °C, which do not occur in the second run. Since the photopolymerization during the printing process utilizes a limited illumination for each layer, there are still unreacted vinyl groups in the polymer network or even non-polymerized monomers, which explains the observations in the DSC measurement. Furthermore, in commercial stereolithography, post-curing is common in order to achieve the final properties of the printed part. Whether post-curing can be used to prevent layer separation was examined in a short experiment. Instead of heat, UV irradiation was used for the post-polymerization. After washing away the excess resin from the printed parts, the sample was submerged in 10 ml of xylene and directly illuminated under a HPHg lamp for 30 minutes. Afterwards, the extraction procedure was conducted as usual. Figure 5.14(b) illustrates the effect of this addition treatment on the macrostructure. While pyrolysis usually induced layer separation, the UV cured sample exhibited a much better macrostructure. Thus, post-curing is a promising method to ensure the mechanical stability of the printed part in case layer separation occurs. Since 30 vol% DOctP was used for the production of larger monoliths that do not exhibit layer separation, post-curing methods were not examined further.

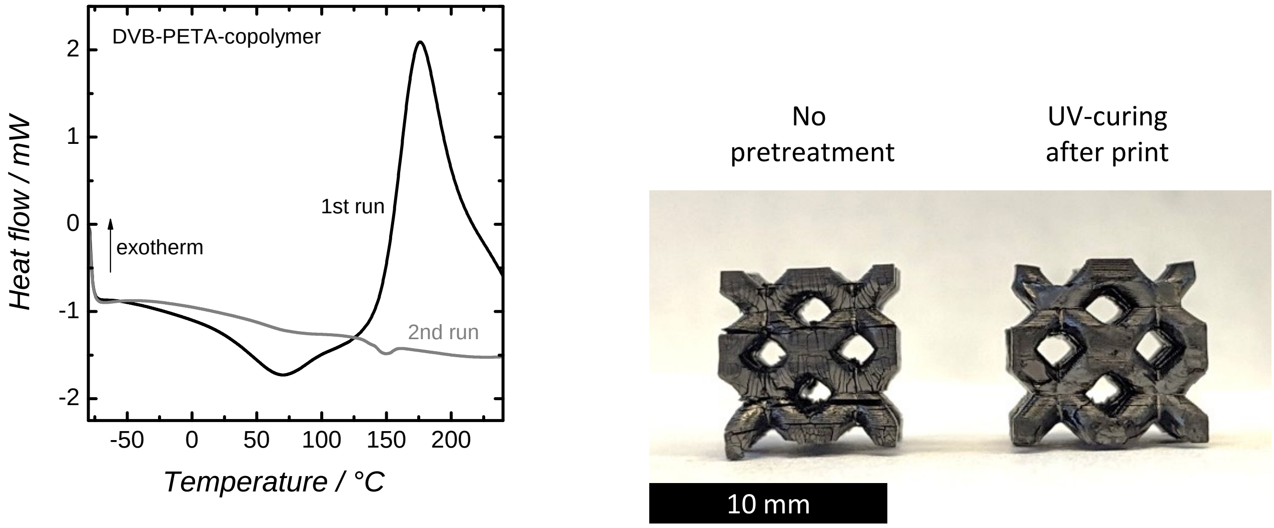

(a) (b)

**Figure 5.14:** (a): DSC measurement of extracted and dried polymer produced from 35 vol% PETA, 35 vol% DVB and 30 vol% DIP; (b): Samples oxidized at 300 °C and pyrolyzed at 900 °C without and with UV post-curing in air (increased brightness for better visibility).

### 5.3.2 Micro- and mesoporosity after pyrolysis

During decomposition of the polymer, the carbon phase rearranged with a large degree of freedom unconstrained due to the absence of crosslinks. In this case, the reduction in volume resulting from the mass loss in the pyrolysis and the increase in density (roughly 1.2 g $cm^{-1}$ for the polymer to 2.1 g $cm^{-1}$ for the carbon) lead towards the reduction in size of the whole printed part instead of the establishment of pore volume.
In the previous chapter, the impact of the oxidation temperature on macroscopic stability was already evaluated and a reduction in shrinking was observed. Here, the impact on the porosity will be examined.

In a series of experiments, 3D printed polymer tetragonal open-cell test structures (as used previously) were oxidized at different temperatures and subsequently pyrolyzed. Figure 5.15 displays the $N_2$ adsorption isotherms and the calculated BET specific surface areas. Despite several attempts, two problems occurred during the analysis. Firstly, not every isotherm was fully measured but sometimes stopped during the analysis. The non and at 200 °C oxidized samples' measurement aborted during the adsorption isotherm between 0.8 and 1.0 relative pressure and for the 280 °C oxidized sample, the desorption was recorded only down to a relative pressure of 0.6. Furthermore, all samples that were fully measured exhibited an open hysteresis. It is believed that both phenomena are caused by nearly closed pores with diffusion limitation, as discussed in chapter 5.2.1 (p.47).

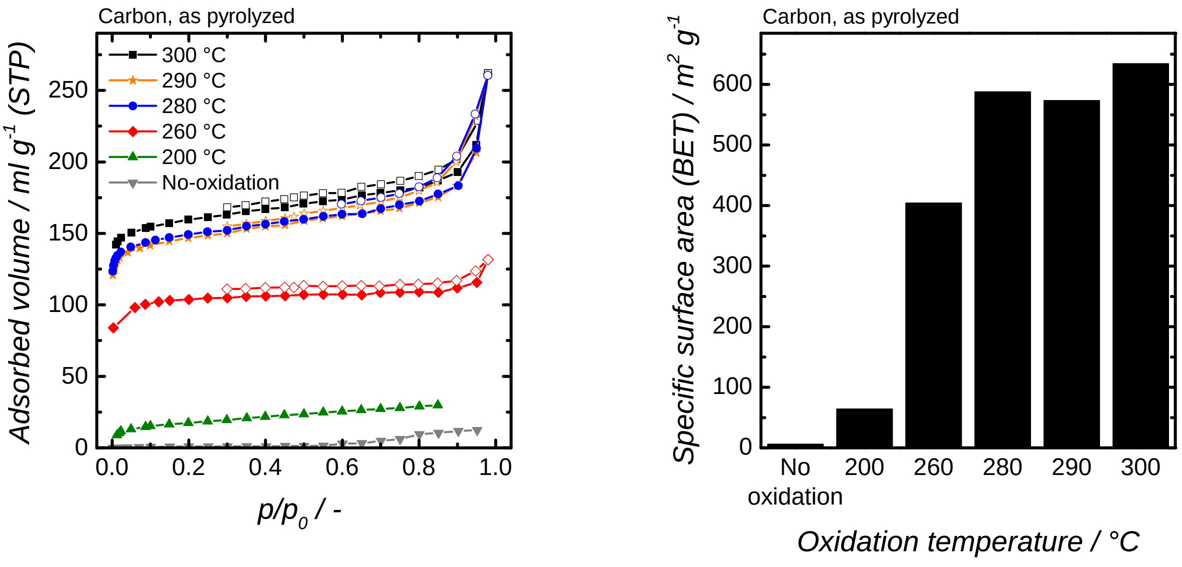

(a) (b)

**Figure 5.15:** $N_2$ adsorption analysis results of 3D printed polymer (30 vol% DIP) derived carbon produced with different oxidation temperatures from 200 to 300 °C or without oxidation; (a): Isotherms; (b): BET specific surface area.

The 200 °C oxidized sample exhibited a small SSA close to the non-oxidized sampled, which has no open micropores. Therefore, the mere addition of oxygen to the polymer, as it is the case for oxidation at 200 °C, is not enough to create a high SSA material. Instead, there needs to be a combination of oxidation and decomposition of oxygen surface groups. While oxidation at 260 °C before the pyrolysis produced a material with 400 $m^2g^{-1}$, a stabilization in the range of 280 to 300 °C created material with around 600 $m^2g^{-1}$. In comparison to the 260 °C specimen, the high temperature oxidized samples also exhibited a more substantial increase in the adsorbed volume of the isotherm towards ambient pressure ($p/p_0 > 0.85$), which indicates a larger fraction of macropores. This observation proves that a high oxidation temperature does not only stabilize the macrostructure but also creates a microporous carbon and retains the porogen templated pores upon pyrolysis.

In the previous variation of the oxidation temperature, 30 vol% DIP were used as porogen. However, in order to tailor the meso- or macropores size, also other porogens might be utilized. Using 300 °C as oxidation temperature, polymer OCS produced with different porogens were oxidized and pyrolyzed. Figure 5.16 displays the results of their pore characterization using Hg porosimetry and $N_2$ adsorption (the values are listed in Table 5.2).

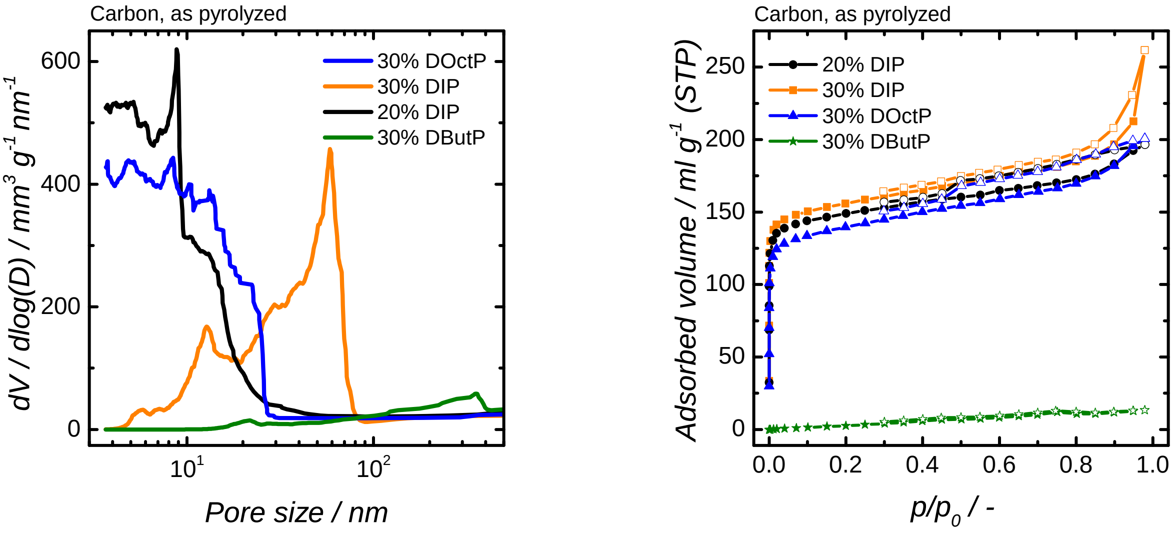

(a)

(b)

**Figure 5.16:** Pore analysis of oxidized (300 °C) and pyrolyzed (900 °C) 3D printed polymers produced with different concentrations and types of phthalates; (a): Differential volume distribution from mercury intrusion porosimetry; (b): $N_2$ adsorption isotherms.

After oxidation and pyrolysis, all of the specimens experienced a similar reduction of mass of 65 to 68 %. The reduction in volume, however, followed the amount of porogen used. The volume reduction for 20 vol% DIP amounted to 63 %. This decrease is significantly smaller than the other samples, which were produced with 30 vol% of porogen and underwent a reduction of 67 to 72 %. The calculated maximum pore diameter decreased for all porogens but 30 vol% DButP. In contrast to its polymer precursor, it did not show mesopores anymore and a new fraction of large macropores in the range of 3 to 30 $\mu$m formed instead. The whole pore size distribution is presented in the appendix in Figure 7.5. Among the other samples, 30 vol% DIP kept having the largest pores after the pyrolysis with a maximum of 69 nm in contrast to 28 and 26 nm for 20 vol% DIP and 30 vol% DOctP respectively.

**Table 5.2:** Results of $N_2$ sorption and Hg porosimetry of the oxidized (300 °C) and pyrolyzed (900 °C) 3D printed polymers printed using different phthalates as porogen.

| Porogen | Carbonization | | $N_2$ adsorption (QSDFT) | | | Hg porosimetry | |
|---|---|---|---|---|---|---|---|
| | $\Delta m/m$ /% | $\Delta V/V$ /% | $a_{SSA}$ /$m^2g^{-1}$ | $v_{Pore}$ $cm^3g^{-1}$ | $d_{Micropore}$ /nm | $d_{90\%,Polymer}$ /nm | $d_{90\%,Carbon}$ /nm |
| 20 vol% DIP | 68 | 63 | 601 | 0.28 | 0.75 | 30 | 28 |
| 30 vol% DIP | 66 | 72 | 655 | 0.35 | 0.72 | 156 | 69 |
| 30 vol% DOctP | 67 | 71 | 536 | 0.29 | 0.80 | 81 | 26 |
| 30 vol% DButP | 65 | 67 | 21 | 0.02 | 2.30 | 52 | 21443 |

As in the Hg porosimetry, 30 vol% DButP showed no meso- or macropores in the $N_2$ adsorption measurement. Furthermore, it lacked open microporosity resulting in only 21 $m^2g^{-1}$. While 20 vol% DIP and 30 vol% DOctP both exhibited a mesopore hysteresis, the isotherm of 30 vol% DIP indicated the presence of macropores and large mesopores with a slight hysteresis. The samples had a similar specific surface area of 536 $m^2g^{-1}$ for 30 vol% DOctP on the lower end to 655 $m^2g^{-1}$ for 30 vol% DIP on the upper end. Among these samples, also the average pore diameter and pore volume is similar.

Thus, through stabilization and pyrolysis, it was possible to retain the meso- and macroporosity for most of the samples. Using the same method, similar specific surface areas, as well as similar micropore diameters, were created in the material. Only if the phthalate with the shortest substituents, dibutyl phthalate, was used, the structure collapsed and no open porosity was measured. However, mass loss and degree of shrinking were similar to the other samples and much smaller than without oxidation, so the presence of pores can be assumed for 30 vol% DButP as well.

### 5.3.3 Increasing SSA through $CO_2$ activation

Post-pyrolysis activation methods are a poplar tool to increase porosity or alter surface chemistry. In this work, $CO_2$ activation was applied to partially oxidize the carbon material after the pyrolysis. In a first series of tests, the impact of activation temperature and time was investigated. As carbon base material 30 vol% DOctP was used, as it is most promising in terms of stability and morphology after the print and also exhibits sufficient specific surface areas after the pyrolysis. Figure 5.17 and Table 5.3 display the results of the $N_2$ adsorption analysis. The two blue dashed lines illustrate the increase in the specific surface area assuming a solely reduction of the mass at constant total surface area.

Despite the low degree of mass reduction of 23 % at a temperature of 860°C, the specific surface area (+145 %) and pore volume (+107 %) more than doubled. This improvement was far greater than could be expected just from the reduction of the carbon reference mass in the calculation of the specific surface area. Also, the more substantial percentual increase in the SSA indicates a reduction in the calculated average pore diameter. This calculation leads to the conclusion that new pores opened through the activation that could not be accessed priorly. Impacted by the shrinking during the pyrolysis process, the new pores were very narrow. Thus, they contributed more to the surface area than to the pore volume.

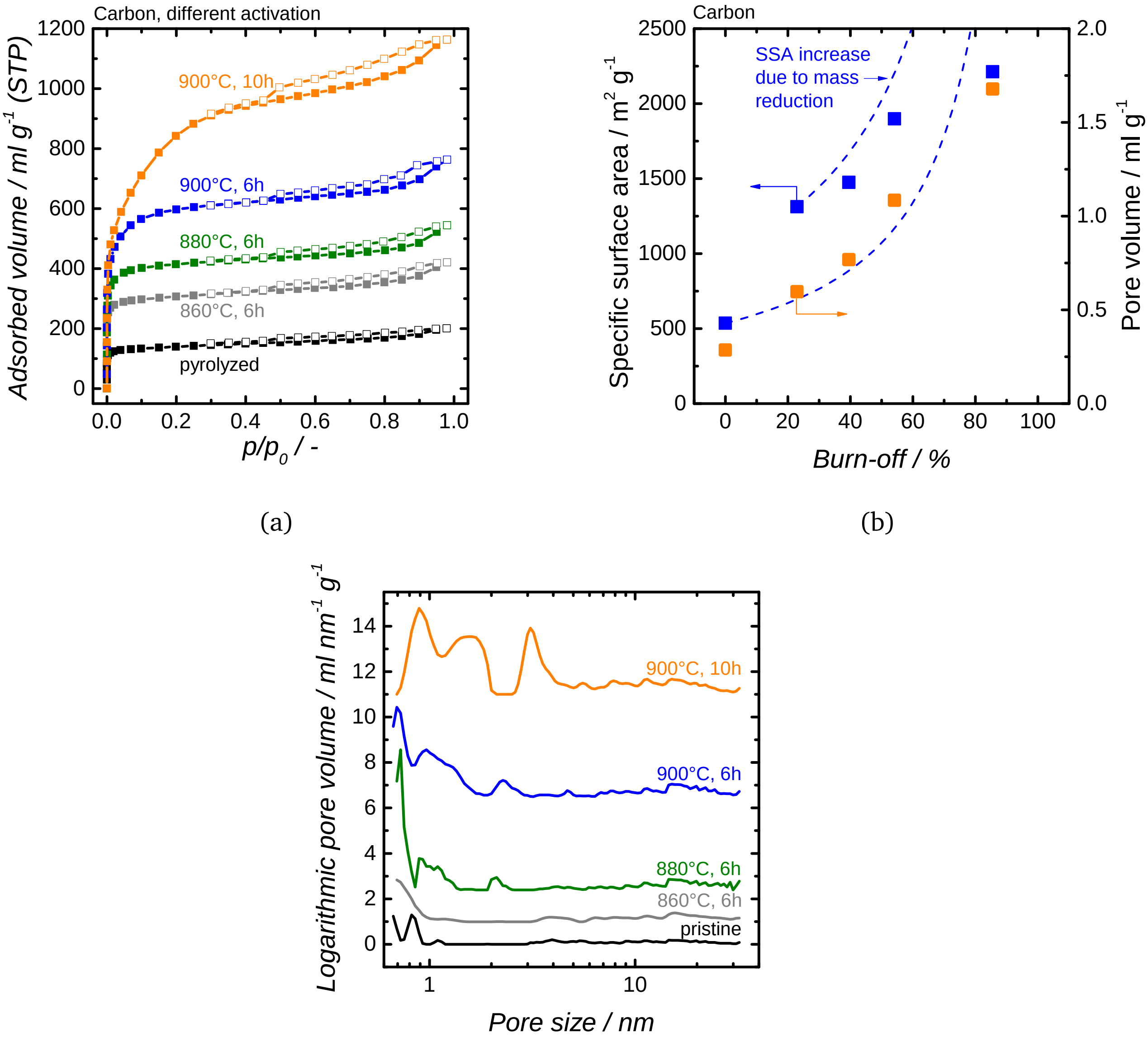

(a)

(b)

(c)

**Figure 5.17:** Variation of the activation procedure for carbon (2x2x2 tetragonal OCS) produced from 3D printed polymer (30 vol% DOctP) produced via oxidation (300 °C) and pyrolysis (900°C); (a): $N_2$ adsorption isotherms; (b): Specific surface area and specific pore volume calculated with QSDFT method, dashed lines represent the increase in SSA due to just the burn-off of the carbon through activation; (c): Logarithmic pore size distribution.

At higher activation temperatures and times, the burn-off became larger and both the specific surface area and pore volume increased. However, in contrast to the lowest activation temperature, the SSA rose less than expected through the reduction in mass, as the second dashed line shows starting from 860 °C illustrates. Simultaneously, the average pore diameter steadily increased. Hence, all of the closed pores became accessible for the nitrogen already at a low degree of activation. At the higher temperatures, some pores widened while some pores were joined together as the pore size distribution shows. This was likely caused by the removal of the separating wall between the pores due to the extremely high mass loss. Thus, the surface area decreased and the average micropore diameter increased. At the highest degree of activation, the specific surface area rose to 2213 $m^2g^{-1}$ at a pore volume of 1.68 $cm^3g^{-1}$. A BET calculation delivers a value of 3019 $m^2g^{-1}$. As BET is not recommended for microporous materials, this value only serves for a comparison with other publications that do not perform a DFT evaluation.

**Table 5.3:** Results of $N_2$ sorption of variation of the activation procedure for carbon produced from 3D printed polymer (30 vol% DOctP) produced via oxidation (300 °C) and pyrolysis (900°C).

| Activation method | Burn off | Nitrogen sorption (QSDFT evaluation) | | |
|---|---|---|---|---|
| | Δm/m /% | $a_{SSA}$ /$m^2g^{-1}$ | $v_{Pore}$ $cm^3g^{-1}$ | $d_{Micropore}$ /nm |
| Non-activated | - | 536 | 0.29 | 0.81 |
| 860 °C, 6 h | 23 | 1312 | 0.60 | 0.75 |
| 880 °C, 6 h | 40 | 1474 | 0.77 | 0.83 |
| 900 °C, 6 h | 54 | 1898 | 1.08 | 0.96 |
| 900 °C, 10 h | 86 | 2213 | 1.68 | 1.27 |

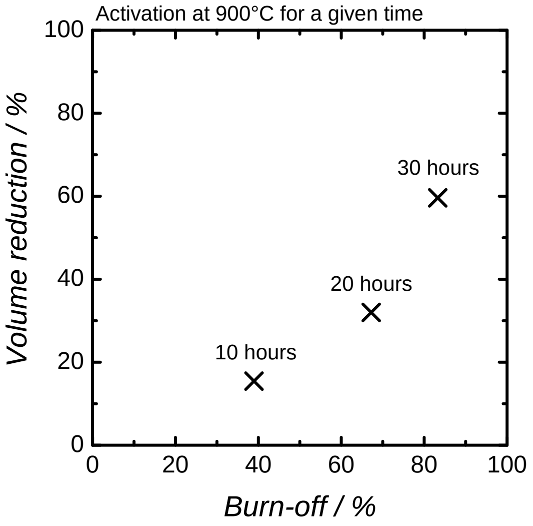

**Figure 5.18:** Reduction of volume as a function of mass loss caused by $CO_2$ activation at 900 °C for 10, 20 or 30 hours of a 3D structure carbon monolith ($T_{Oxidation}$=300°C, $T_{Pyrolysis}$=900°C) with a diameter of 20 mm and a length of 45 mm based on a tetragonal unit cell ($d_{Cell}$=5,7mm, $d_{Cylinder}$=2mm).

In Figure 5.18, the dependency of reduction in volume and mass is shown (values can be found in the appendix in Table 7.1). In contrast to earlier experiments, not a small piece of carbon but a larger open-cell monolith (diameter: 15 mm, length: 40 mm) was utilized in order to increase the accuracy of the volume measurement. While the small test subjects fit in a crucible, the monolith was hold down by weight in the form of a halved stainless steel tube with a wall thickness of 2 mm. This shell insulated the monolith and reduced the inner temperature. Thus, despite the activation at 900 °C for 10 hours, the burn-off amounted to only 39 % in contrast to earlier experiments that yielded a value of 86 %. At this low degree of burn-off, the size reduction amounted to only 15 %. At higher burn-offs, the reduction in volume sharply increased, reaching a value of 60 % for an 83 % burn-off. This observation proves that also after the pyrolysis, the carbon framework is not entirely rigid, but can undergo changes when subjected to oxidation processes.

With an SSA of 1474 $m^2g^{-1}$, the $CO_2$ activation at 880 °C for 6 hours poses a compromise between the increase in SSA and pore volume and not degrading the carbon due to a high mass loss. At these conditions, pristine carbons produced with different porogens were activated and analyzed by $N_2$ adsorption. Figure 5.19 displays the results. Through $CO_2$ activation, the specific surface area of all carbons increased. 30 vol% DIP reached the highest value of 1791 $m^2g^{-1}$. The other carbons achieved a similar SSA in the range of 1510 to 1577 $m^2g^{-1}$. Even 30 vol% DButP, which did not exhibit open porosity after the pyrolysis reached an equal value. The meso- and macroporosity remained unchanged, judging from the shape of the isotherm. 30 vol% DButP, however, exhibited a tiny amount of mesopores even though it caught up in terms of microporosity. This collapse of the transport pores might be the reason for the non-accessibility of the pores after the pyrolysis.

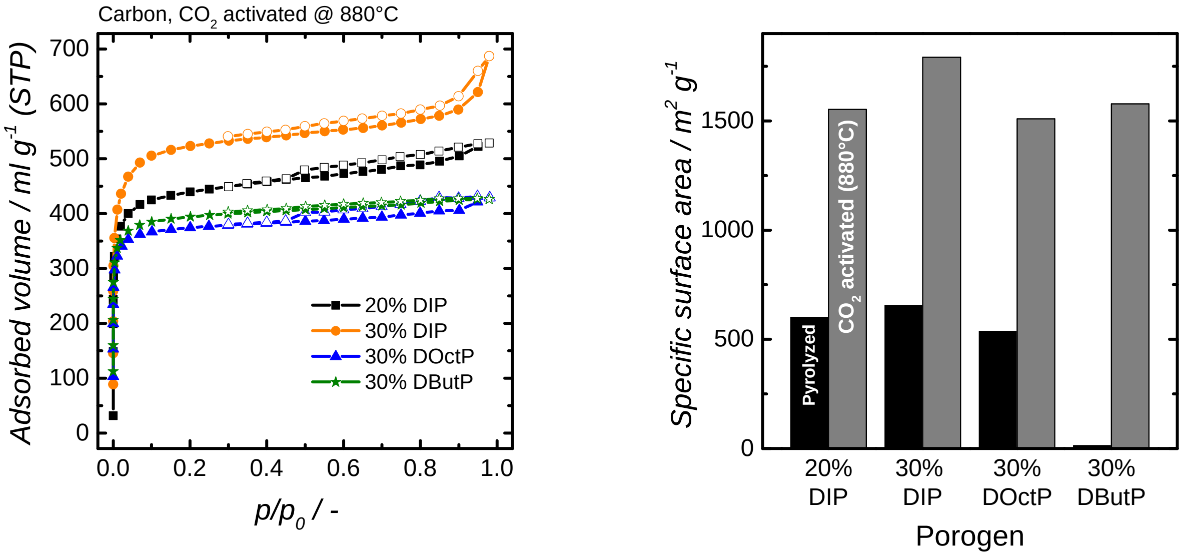

(a) (b)

**Figure 5.19:** Porogen variation of $CO_2$ activated carbon (6 hours at 880 °C) synthesized from oxidized (300 °C) and pyrolyzed (900 °C) 3D printed polymers; (a): $N_2$ adsorption isotherms; (b): QSDFT calculated specific surface area after pyrolysis and after $CO_2$ activation.

Figure 5.20 depicts an overview of the reduction of mass over the whole process, starting with the extracted polymer. In comparison to the other samples, 30 vol% DButP lost less mass in the oxidation. The additional reduction compensated this difference during the pyrolysis. As described in chapter 5.3.2, a low degree of mass loss in the oxidation has a negative influence on the stabilization and thus leads to a small specific surface area. In fact, 30 vol% DButP suffered from a lack of open porosity, although judging from the density, there should be pores present. In the activation, the samples exhibited a mass loss of 10 % (30 vol% DOctP) to 14 % (20 vol% DIP).

In summary, it was shown that $CO_2$ activation is a viable tool to tailor the porous properties of the 3D modeled carbon. Either closed pores can be made accessible at a low degree of activation or the pore size can be increased at a high degree of activation. Furthermore, it became clear that this process delivers similar outcomes regardless of the porogen. However, in the case of high degrees of activation, the reduction in size needs to be taken into account.

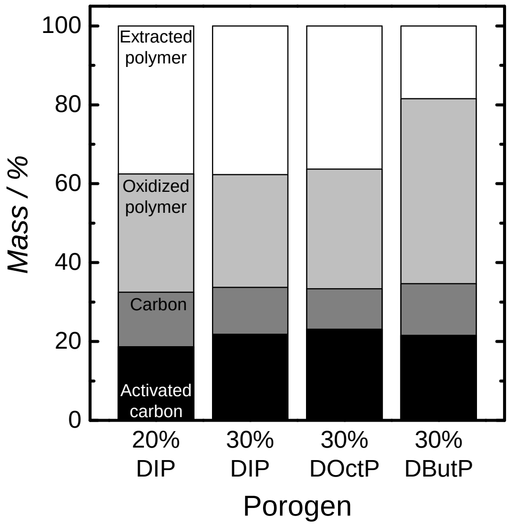

**Figure 5.20:** Reduction of mass for all porogen throughout oxidation, pyrolysis and $CO_2$ activation based onthe mass of the extracted polymer.

In previous experiments, a polymerization time of 120 seconds for each layer was used to 3D print small open-cell structures comprised of 8 single unit cells. However, when printing larger monolithic structures, blocking of pores in the macrostructure can be observed. Disruptions in the x-y-plane are most prominent, but also in the z-direction, a clogging of channels was observed. In order to counteract the deviations from the programmed geometry, a variation of the layer's illumination time was conducted. Figure 5.21 illustrates the results.

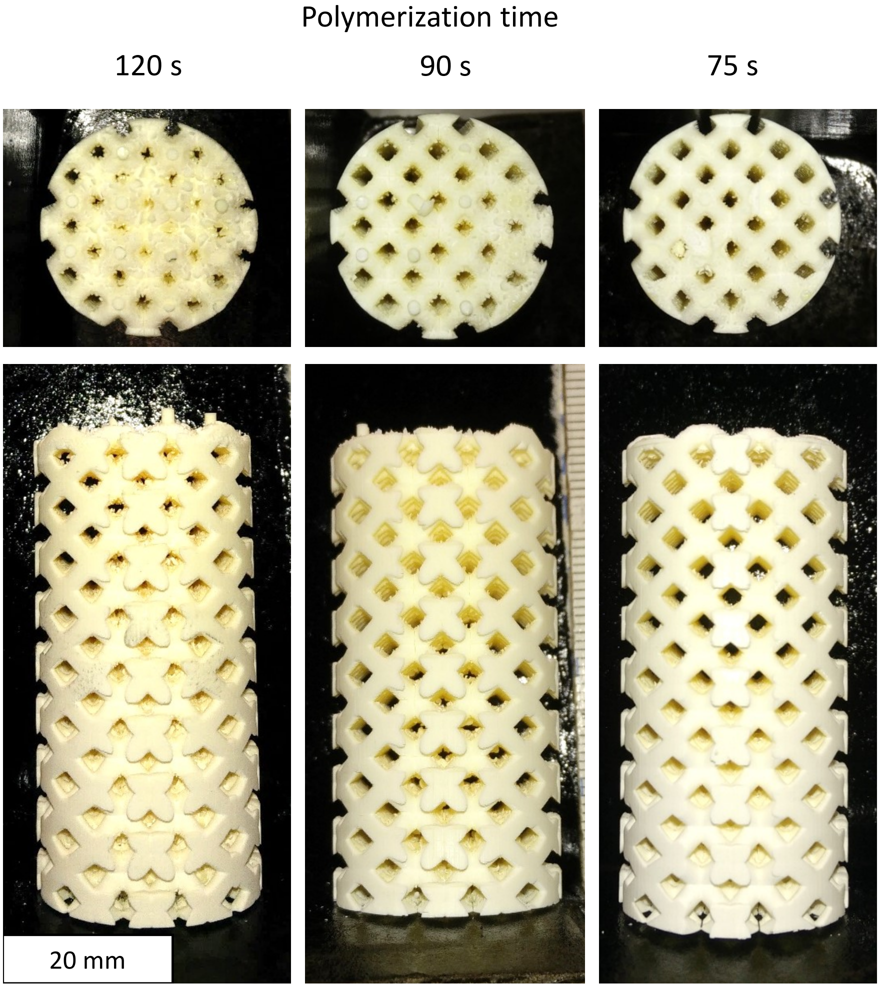

**Figure 5.21:** Printed and extracted 3D printed polymer monoliths (30 vol% DOctP, 35 vol% DVB, 35 vol% PETA, 0.4 mg ml$^{-1}$ Sudan1) printed with different illumination times viewed from the front and the top.

With the original illumination time of 120 s, the blocking of the channels in the structure increased towards the middle. While they are open near the outside with just a chippy surface, these flakes increase in volume and block most of the vertical channels in the middle (visible from the top). The horizontal channels (visible from the side) are also nearly wholly blocked in the middle of the structure. Here the outer channels are also less impacted. With the reduction to 90 and ultimately 75 seconds of illumination time, there is less of a chippy surface structure and less blocking of channels in the vertical as well as in the horizontal direction.

Several factors could explain these occurrences. Since an increase in temperature was observed already, it likely occurs even more for a large illuminated area. Through the diffusion and convection of oligomers and radicals, polymerization can also occur at non-illuminated volumes and accelerated by the temperature. Likewise, less time is necessary for the solidification at the illuminated spots. At 75 s the channels at the inside of the structure remained open.

With the adjusted parameters, different open-cell structures were created. Their unit cells consisted of a diamond, gyroid and a tetragonal structure. Figure 5.22 displays the porous polymers and the derived pyrolyzed carbon structures.

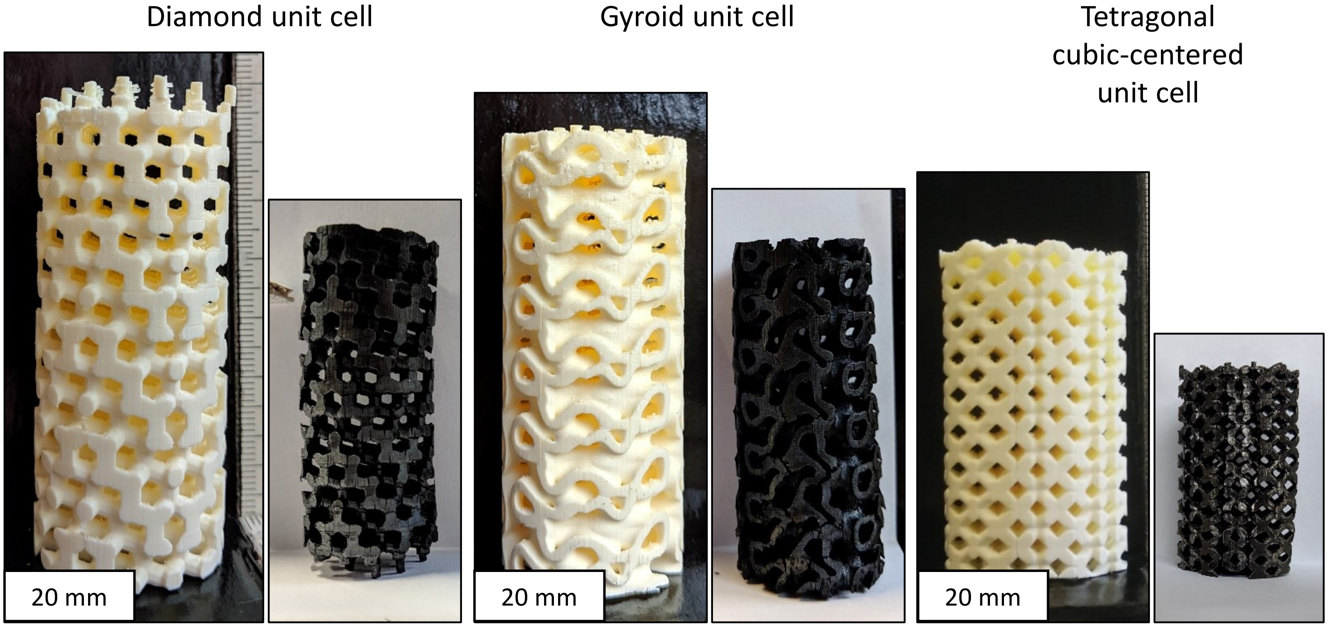

**Figure 5.22:** Porous polymers and the from this derived porous carbons (oxidized at 300 °C for 6 h, pyrolyzed 900 °C) open-cell structures from a diamond, gyroid and tetragonal cubic-centered unit cell.

In summary, in the previous chapters, it was shown how to 3D print a porous polymer with tailored meso- and macropore size. These polymers were converted into porous carbon while maintaining the templated pores and creating a new fraction of micropores with the use of the right conditions of oxidation before the pyrolysis. Furthermore, the microporosity can be tuned by $CO_2$ activation in terms of pore size, specific surface area and pore volume. Lastly, it was shown how to upscale the dimensions of the printed parts by adjusting the illumination time of the printer.

## 5.5 Electic swing adsorption using conventional and 3D printed carbons

Every temperature swing adsorption process is based on regenerating the adsorbent at an elevated temperature. In the particular case of the electric swing adsorption, Joule heating introduces the energy required for the heat-up. In the following, resistive heating is examined for a 3D printed carbon (oxidized at 300 °C, pyrolyzed at 900 °C, no activation) monolith and commercial carbon pellets (Norit RX 1.5 Extra).

### 5.5.1 Electrical resistive heating of carbon adsorbers

At first, an infrared camera is used to evaluate the time dependency and temperature distribution when heating the monolith in air. A thermographic measurement in the adsorption cell is not possible since the adsorption cell, which is made of borosilicate glass, adsorbs infrared light. Furthermore, also the carbon pellets were not analyzed by this method since they are not free-standing and need to be framed by a measurement cell. Figure 5.23 displays the setup for the 3D printed carbon monolith and temperature over time.

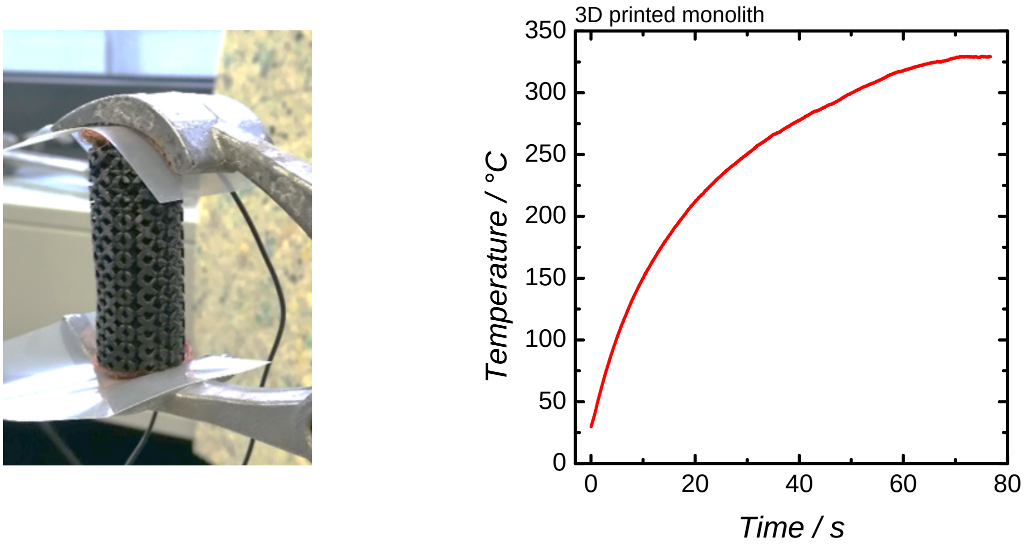

(a)

(b)

**Figure 5.23:** Thermographic measurements of a carbon monolith produced via oxidation (300 °C) and pyrolysis (900 °C) of a 3D printed polymer (30 vol% DOctP, 35 vol% DVB, 35 vol% PETA); (a): Electrode carbon assembly; (b): Temperature over time of the hot-spot during heat-up (4.5 A, 4 V, 18 W).

Through resistive heating, the monolith with a mass of 5.2 g quickly increased its temperature to 300 °C after 50 s. The measurement was stopped after 70 s in order not to damage the monolith. Still, it was not used in further adsorption experiments. In order to evaluate the temperature distribution, the image of the thermographic measurement with the highest temperature was evaluated further. Figure 5.24 depicts a thermographic depiction of the monolith, together with a vertical and horizontal temperature profile. The pixel with the highest temperature of this frame constitutes the point of intersection of the temperature profiles depicted as dashed black lines in the image.

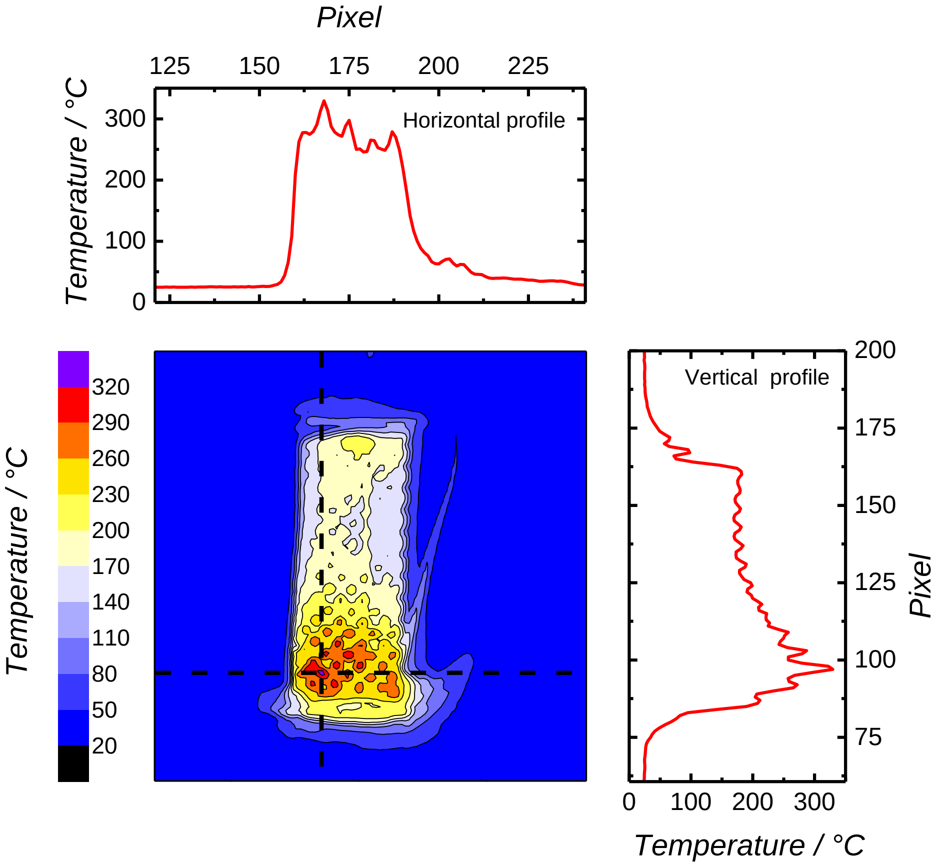

**Figure 5.24:** Thermographic measurements of a carbon monolith produced via oxidation (300 °C) and pyrolysis (900 °C) of a 3D printed polymer (30 vol% DOctP, 35 vol% DVB, 35 vol% PETA): Highest temperature containing frame together with the vertical and horizontal temperature profiles.

Superficially observing the thermographic image, it seems that there is a notable temperature hot-spot at the lower end reaching 320 °C of the monolith and another small hot-spot at the top with a temperature above 200 °C. Simultaneously, significant parts in the upper half of the monolith exhibited a temperature of only 140 to 170 °C. Regarding the profiles, the temperature distribution seems uneven with regularly occurring spikes, especially in the lower third of the monolith in the part of the image, which comprised the hot-spot.

As seen in Figure 5.23a, the monolith exhibited channels originating from the design of its unit cells (see Figure 5.6 for an image). However, the resolution of the thermographic camera (240 x 320 pixel) is not sufficient to fully resolve these channels. Thus, the temperature of out- and inside mix and the temperature profile exhibited sharp spikes. However, this phenomenon occurred if the camera aligned with the channels, specifically at the lower half of the monolith. In contrast, at the monolith's top, only a minor temperature oscillation was observed since the camera mostly records the temperature at the outside due to a different viewing angle.

Additionally to the thermographic measurements, the temperature of the adsorbent beds was measured in the adsorption cell with thermocouples. Figure 5.25 displays the corresponding temperature profiles of the 3D printed carbon monolith and the carbon pellet bed (Norit RX 1.5) at three different heights.

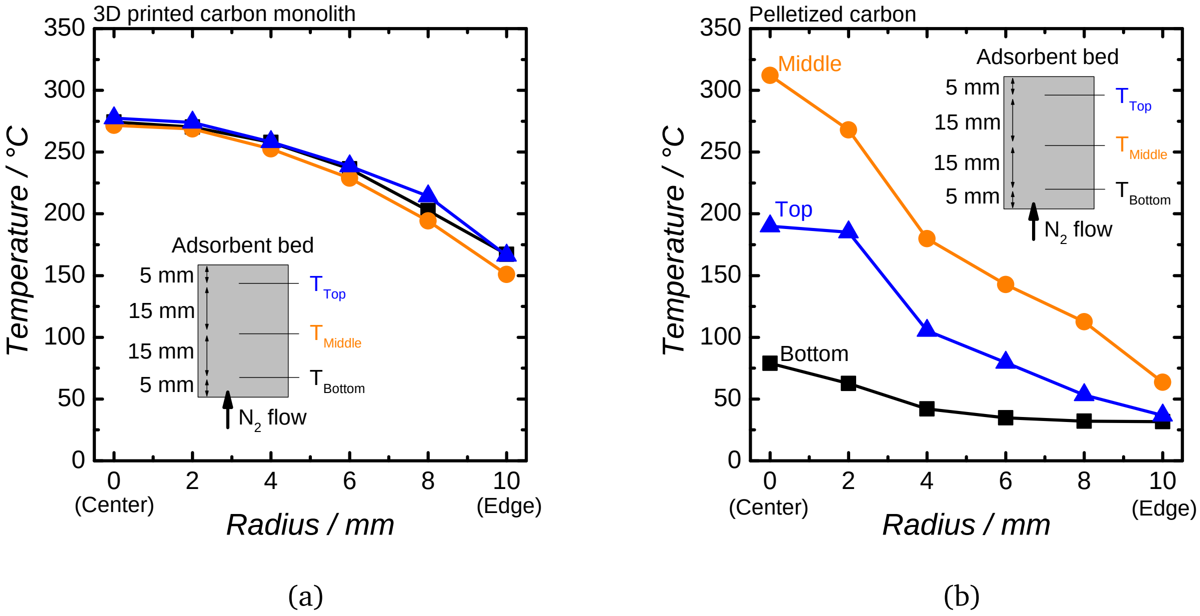

**Figure 5.25:** Temperature profiles of two carbon adsorbents in the ESA adsorptions cell measured at 3 different heights; (a): 3D printed carbon monolith (30 vol% DOctP, $T_{oxidation}$=300 °C, $T_{pyrolysis}$=900 °C); (b): Norit RX 1.5 carbon pellets.

In this measurement, the carbon monolith exhibited a homogeneous temperature profile in vertical direction, using a power of 24.7 W (3.8 V, 6.5 A). While the monolith reached around 275 °C in the center, the temperature decreased towards the edge and the cooled wall of the adsorption cell ($T_{cooling}$ = 30 °C). At least a temperature of 150 °C was measured owing to the presence of a gap between the monolith and cell's wall of approximately 0.5 mm.

Upon resistive heating, the carbon pellets exhibited the highest temperature (310 °C) in the very center of the bed using a power of 30 W (10.7 V, 2.8 A). Both, at the top and towards the bottom of the pellet bed, the temperatures decreased. Also, towards the cell's wall, the temperatures fell below 100 °C.

In summary, both adsorbents can be electrically heated. In contrast to the pellet bed, the monolith exhibited a much more homogeneous temperature profile due to the heat conductivity of the continuous carbon structure. Especially at the bottom, the influx of nitrogen gas cooled the pellet bed. Due to the narrow points of contact of the single pellets with each other, the heat conductivity is low and the deviation in temperature high.

### 5.5.2 Cyclic electric swing adsorption

Three different carbon materials were analyzed in cyclic electric swing adsorption. In addition to the 3D printed pristine monolith and the extruded carbon pellets “Norit RX 1.5 Extra”, a 3D printed activated carbon monolith was used. It underwent $CO_2$ activation up to a mass reduction of 49 %. The adsorption was conducted at the high hexane vapor concentration of 5.5 mol% equal to a mass flow of 2.1 mg min$^{-1}$

for at least 22 hours. After adsorption, the carbon material was heated to a temperature of 300 °C measured in the middle of the carbon bed or structure, which facilitated the desorption of the hexane. After 22 hours, the desorption was terminated. Figure 5.26 displays the breakthrough curves and vapor concentration profiles of the desorption. Further data about the pore characteristics and from the analysis of the ESA are listed in Table 5.4. The calibration curves for adsorption and desorption are displayed in the appendix in Figure 7.8 (p. 82).

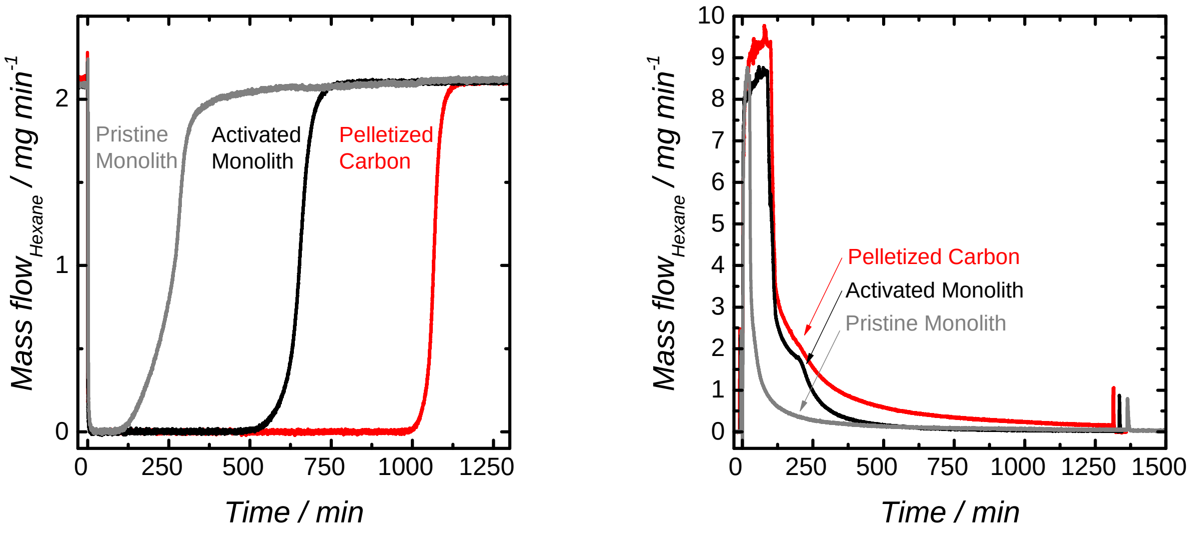

(a) (b)

**Figure 5.26:** First adsorption cycle of different carbon materials in an electric swing adsorption: pristine carbon monolith, activated carbon monolith ($CO_2$, 12 h @ 900 °C); (a): adsorption breakthrough curves; (b): concentration profiles of the desorption.

**Table 5.4:** Results of QSDFT evaluation of nitrogen sorption analysis prior to the ESA tests, and from the first breakthrough test of every material.

| Specimen | Mass | Nitrogen sorption (QSDFT)[a] | | | Electric swing adsorption | | | |
|---|---|---|---|---|---|---|---|---|
| | | $a_{SSA}$ | $v_{PV}$ | $d_{Pore}$ | $m_{C_6H_{14},Ads}$ | $\delta_{Hexane}$ | $t_b$[b] | $A_{Hexane}$ |
| | / g | / $m^2g^{-1}$ | / cm $g^{-1}$ | / nm | / g | / $g_{Hex}$ $cm^{-3}$ | /min | / $nm^2$ |
| Pristine monolith | 5.18 | 785 | 0.26 | 0.66 | 0.55 | 0.41 | 107 | 1.09 |
| Activated monolith | 1.85 | 2023 | 1.16 | 1.15 | 1.34 | 0.62 | 520 | 0.40 |
| Carbon pellets | 3.91 | 1660 | 0.89 | 1.07 | 2.28 | 0.66 | 1004 | 0.41 |

[a] The nitrogen sorption isotherms are displayed in the appendix in Figure 7.7 (p. 81).
[b] Breakthrough was defined as an increase above the mass flow of 0.021 mg min$^{-1}$, which equals 1 % of the initial mass flow.

The pristine carbon exhibited the lowest pore volume of 0.26 ml g$^{-1}$ of all the carbon materials in the tests. Likewise, an early breakthrough after 107 min occurred. At this point, the outlet hexane concentration slowly increased until, after 400 min, the adsorption completed at an outlet mass flow of 2 mg min$^{-1}$. Both the early onset and the extended time needed for complete adsorption indicate a

slow internal mass transfer of the carbon material. Since pore diffusion issues already occurred during nitrogen adsorption, it likely also impacts the adsorption of hexane. The apparent density of hexane was calculated as the ratio of adsorbed mass and pore volume from the nitrogen sorption. After full adsorption, only 0.41 grams of hexane adsorbed per milliliter of the pore volume. From nitrogen sorption it is known that the density of the adsorbed species in the pores is as large as the liquid density or even larger for smaller pores. From the literature it is known that the density of adsorbed hexane in micropores is at least as large as its liquid density [169]. At 30 °C, the liquid density of hexane amounts to 0.6502 $\mathrm{g\,ml^{-1}}$ [170]. A lower calculated density means that not all the pores, which were accessible in the $N_2$ adsorption analysis, could be utilized for the adsorption of hexane in the ESA. Therefore, the size restricted access impact the pore utilization as well as the speed of diffusion inside the pristine monolith.
Upon $CO_2$ activation of the monolith, the specific surface area, as well as the pore volume, increased to 2023 $\mathrm{m^2g^{-1}}$ and 1.15 $\mathrm{cm^3g^{-1}}$, respectively. Thus, the adsorbed mass of hexane more than doubled from 0.55 to 1.34 g. Furthermore, the breakthrough time increased to 520 min. In contrast to the pristine carbon, the breakthrough is much sharper. This observation can be explained by the larger average pore diameter, which was increased by the activation. The calculated density of hexane amounts to 0.62 $\mathrm{g}_{Hex}\,\mathrm{cm}^{-3}_{Pore}$, which is close to the liquid density of hexane of 0.65 $\mathrm{g\,cm^{-3}}$ at 30 °C [170]. The contribution of mesopores can explain this difference, since, depending on the vapor pressure, pore condensation might not take place.
The steam activated pelleted carbon incorporated a specific surface area of 1660 $\mathrm{m^2g^{-1}}$ and a pore volume of 0.889 $\mathrm{cm^3g^{-1}}$, which is considerably lower than the activated monolith. But due to denser packing of the carbon in the test cell, a larger mass was used. Therefore, the carbon pellets adsorbed a hexane mass of 2.28 g leading to a sharp breakthrough at a time of 1004 min. The calculated density of hexane is 0.66 $\mathrm{g}_{Hex}\,\mathrm{cm}^{-3}_{Pore}$, which is similar to the activated monolith.
From the specific surface area determined in $N_2$ adsorption and the adsorbed mass, the area per hexane molecule can be calculated. For the pristine monolith, this value amounts to 1.09 $\mathrm{nm^2}$, which is around three times the one of 0.36 $\mathrm{nm^2}$, which was reported in the literature [171]. The values for the activated monolith and the carbon pellets are 0.40 and 0.41 $\mathrm{nm^2}$, respectively. These values are much closer to the literature value. In general, the mesopores do not contribute much to the specific surface area. Thus, the adsorption capacity scales with the specific surface area of the carbon, if a size exclusion effect is not present.

In desorption, the temperature was increased to 300 °C at 5 min after switching to 10 $\mathrm{ml\,min^{-1}}$ of pure nitrogen gas flow. Upon the beginning of the heating, the TCD signal decreased due to a higher flow rate caused by the thermal expansion of the gas in the measurement cell. Shortly after, it increased due to the lower thermal conductivity of the hexane in the gas. In all desorptions, the hexane mass flow, which was calculated from the TCD signal, peaked at values of 8.5 to 9.5 $\mathrm{mg\,min^{-1}}$. The equilibrium concentration at ambient temperature caps this value. Although the measurement cell was temperated to 30 °C, the gas line between the measurement cell and TCD was not temperature controlled but at ambient temperature at around 27 °C. Thus, the hexane condensed at the outlet of the measurement cell and accumulated at the bottom of the same. Therefore, a slight variation of the ambient temperature in the laboratory caused the peak concentration to be slightly higher in the case of the carbon pellets. In the desorption of the pristine carbon monolith, the hexane gas concentration quickly decreased due to the desorption of the major fraction of the adsorbed hexane. In the case of the activated carbon, the desorption at the high hexane flow of 8.5 mg ml$^{-1}$ continued for around 100 min and then quickly decreased. In contrast to the pristine monolith, there is a knee at around 200 min. This phenomenon emanated from the evaporation of accumulated liquid hexane at the measurement cell's bottom, which originated from earlier condensation at the cell wall. The carbon pellets show a similar behavior at the start of the desorption to the activated monolith, although it has a 70 % higher mass of hexane adsorbed. After that, there is a long tailing of low amounts of hexane adsorbed even after 22 hours of runtime. The short spike of the TCD signal at the end of the desorption originates from a short pressure buildup caused by turning the 4-way ball valve. This leads to the conclusion that there is still hexane adsorbed on the carbon pellets after the desorption period of 22 hours. This different behavior of the 3D printed monoliths and the pellets can be explained by the different temperature profiles shown in Figure 5.25. Through the uneven temperature profile of the pellet bed, a sufficient temperature for the fast desorption of hexane cannot be reached close to the wall of the adsorption cell.

Each carbon material was subjected to three subsequent adsorption-desorption cycles. Figure 5.27 displays the concentration profiles of the breakthrough tests and the desorptions for all the carbon materials. The breakthrough curves were evaluated in terms of their breakthrough time and the total adsorbed mass of hexane (see Table 5.5). Earlier experiments showed a good convergence of weighed mass difference of the carbon material before and after adsorption. Nevertheless, when the measurement cell was opened, water from the air adsorbed on its glass surface inside, which disturbed the TCD signal upon desorption in later operation, since water vapor has a higher thermal conductivity than nitrogen. Therefore, in the results presented here, the adsorbed hexane mass was derived from the breakthrough data.

**Table 5.5:** Breakthrough times and adsorbed mass of hexane in three subsequent adsorption-desorption cycles and change of these values from the 1st to the 3rd cycle.

| Specimen | Breakthrough time * | | | | Adsorbed mass | | | |
|---|---|---|---|---|---|---|---|---|
| | 1st run / min | 2nd run / min | 3rd run / min | Change - | 1st run / $g_{C_6H_{14}}$ | 2nd run / $g_{C_6H_{14}}$ | 3rd run / $g_{C_6H_{14}}$ | Change - |
| Pristine monolith | 107 | 126 | 132 | +23 % | 0.55 | 0.52 | 0.51 | -7 % |
| Activated monolith | 520 | 510 | 491 | -6 % | 1.34 | 1.32 | 1.34 | 0 % |
| Carbon pellets | 1004 | 861 | 876 | -13 % | 2.28 | 1.94 | 1.94 | -15 % |

* Breakthrough was defined as an increase above the mass flow of 0.021 mg min$^{-1}$, which equals 1 % of the initial mass flow.

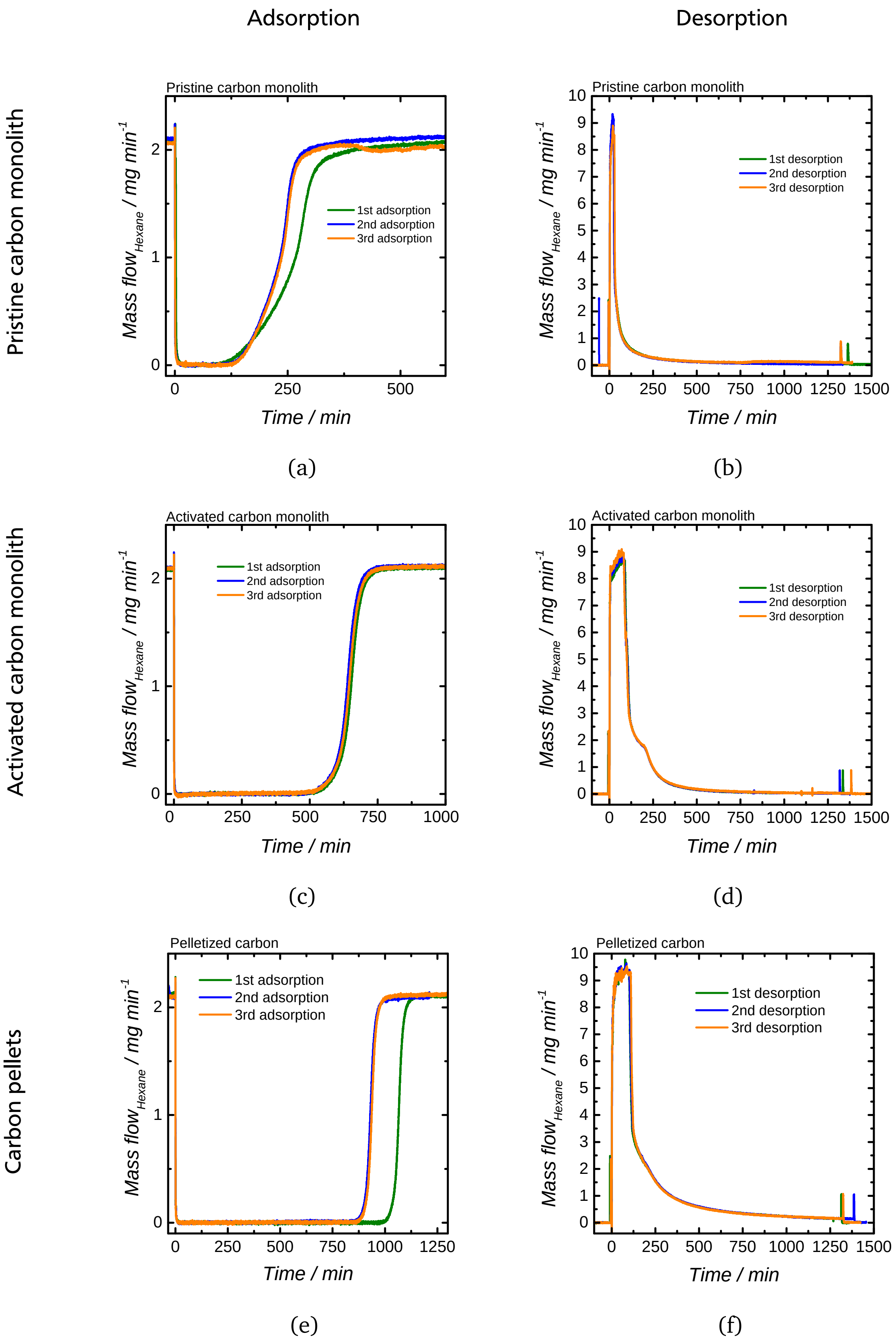

(a) (b) (c) (d) (e) (f)

**Figure 5.27:** Full three adsorption and desorption cycles of the pristine (a,b) and activated (c,d) carbon monolith, and the pelletized carbon (e,f).

On the one hand, the pristine carbon monolith showed an increase in breakthrough time of + 23 % from the first to the third run. On the other hand, the amount of adsorbed mass of hexane decreased by 7 %. This change mainly originated from a change in the shape of the adsorption curve. From the first to the second adsorption, the breakthrough became steeper with a later onset and an earlier reaching of full adsorption. The decrease of total adsorption capacity can be explained by the pore structure of the pristine carbon monolith. The small pores, which are similar to the size of the hexane molecules, confined them and decreased their vapor pressure, so complete desorption could not occur. The change in curve shape indicates an increase in internal mass transport.
The activated carbon monolith exhibited a slight reduction in the breakthrough time of 6 %, but the adsorbed mass did not change significantly. Earlier, it was shown that a significant fraction of the pores were accessible to the hexane molecules through the larger pore size. Thus, the vapor pressure of the hexane increased and the monolith fully regenerated during adsorption.
The carbon pellets experienced a substantial drop in breakthrough time of 13 %, which was caused by a lower capacity for hexane of 15 %. This phenomenon stemmed from the inhomogeneous temperature distribution during the desorption. The peripherals of the carbon bed close to the inlet stream of nitrogen and cell wall were relatively cold, so a substantial part of the hexane remained there.

In the adsorption tests, a pristine and an activated 3D printed carbon monolith, as well as carbon pellets, were used. Through the continuous carbon structure, the pristine monolith exhibited a more homogeneous temperature profile than the carbon pellet bed, both in radial and axial direction. This consistency benefited the monoliths in the desorption of the ESA tests, in which they regenerated to a higher degree.
The activation of the carbon monolith tremendously increased the specific surface area and pore volume and surpassed the values of the carbon pellets. Thus, the total adsorption capacity for hexane improved likewise. By widening the micropores, also the mass transfer inside the pellet, and the pore utilization, bettered. However, based on the same cell volume for the pellets and the monolith, the pellets adsorbed a higher mass of hexane and had a higher breakthrough time.
The monolith geometry had an open porosity of 54 %, which is much more than the porosity between the carbon pellets. By tweaking the size of the unit cell as well as the fraction of void space, the performance can be expected to increase.

# 6 Conclusion

In this work, a 3D printing method for activated carbon was developed. The process is based on the conversion of lithographically 3D printed porous polymers and aimed for tailoring the macrostructure as well as the porous properties in terms of size and amount of micropores and larger meso- or macropores.

In a first step, a suitable photoresin was identified that could be printed to a polymer and converted into carbon. In a screening process, two monomers were combined. Pentaerythritol tetraacrylate exhibited an extremely high polymerization rate upon illumination in the 3D printer, but had a poor carbon yield. In contrast, DVB, a monomer that has not yet been utilized in 3D printing, could only be polymerized at a sluggish rate but showed a high carbon yield. By combining these two monomers, a polymer was printed with an adequate illumination time of 75 s and converted into porous carbon while maintaining the macrostructure. Through monitoring the conversion of vinyl groups, it was shown that both monomers take part in the polymerization with similar reaction rates of their vinyl groups and that a copolymer was created. By varying the dye concentration, the printing was adjusted for either quick manufacturing, while losing accuracy, or slow manufacturing, which made it possible to print fine details down to $100\,\mu$m. Through the addition of a porogen, which acts as an inert substance during photopolymerization, the porogen templating method was successfully transferred to lithographic 3D printing. By variation of the type and amount of porogen, the maximum pore size was tailored from 30 to 150 nm. This illustrates a new method of production of nanoporous polymers with a freely designable macrostructure. The bottom-up molecular design through monomer composition makes this material promising for novel applications in catalysis, since it allows for the introduction of heteroatoms.

In this work, the porous polymer was utilized as a precursor for the transformation into activated carbon. As direct pyrolysis led to the deformation of the macrostructure without open porosity, facile oxidation in air as a pretreatment at temperatures between 280 and 300 °C for 6 hours retained the macrostructure as well as the templated pores and led to the formation of new open micropores. Mass loss and reduction in size were smaller than presented in the literature for obtaining lithographic 3D printed carbon, in which a non-optimized photoresin and methodology were used [161]. In the activation, the porosity was significantly increased to up to $2213\,\text{m}^2\text{g}^{-1}$ and $1.68\,\text{ml}\,\text{g}^{-1}$ (QSDFT), while maintaining mechanical stability. With this new method, activated carbon monoliths can be manufactured with a vast degree of freedom. A hierarchical pore system comprised of templated meso-/macropores and micropores was introduced and tailored in size and volume. Therefore, it can compete even with the most advanced activated carbons that are commercially available.

In the second part of this work, the 3D printed carbon open-cellular structures demonstrated their suitability as an adsorbent for an electric swing adsorption system. In comparison with carbon pellets, they exhibited excellent thermal conductivity due to the continuous structure. The adsorption capacity greatly improved through activation. Upon desorption by electric resistivity heating of the carbon, they created high vapor concentrations without long tailing. Therefore they can be regenerated in a short period of time, with the activated monolith recovered to 100 % of its original capacity. Due to a higher packing density of the pellet bed, their maximum adsorption capacity exceeded the activated carbon monolith. Although they can be used in an ESA principally, as was shown in the literature before, only

85 % of their capacity was restored.
With further improvement of its macrostructure, the 3D printed carbon is an excellent alternative to common ESA materials. Since desorption can be facilitated much faster, investment costs decrease due to a lower amount of parallel apparatuses needed.

Furthermore, 3D printed carbon structures have great potential in catalysis. In addition to optimized pore diffusion, the continuous structure prevents the hot-spot formation and therefore allows higher conversion or selectivity in highly exo- or endothermic reactions.

# 7 Appendix

## 7.1 SCAD source code for 3D modeling of the cubic-centered tetragonal open-cell structures

```
r_0=1;          //Radius of the cylinder, which the unit cell consists of
l_0=5.7;        //Edge length of the unit cell
r_ges=14.5;     //Radius of the whole OCS (14.5 results in 19mm after the carbonization
genau=10;       //Level of approximation of the cylinders
h_ges=10;       //Height of the OCS

repxy=ceil(30/l_0);     //calculated unit cells in x-y direction
echo(repxy);            //Display repxy
repz=ceil(h_ges/l_0);   //calculated unit cells in z direction
echo(repz);

//Creating a cylinder for the unit cell
module bond(x2,y2,z2,x1,y1,z1){
  tx = (x2 + x1)/2;
  ty = (y2 + y1)/2;
  tz = (z2 + z1)/2;
  ax = x2 - x1 ;
  ay = y2 - y1;
  az = z2 - z1;
  translate(v=[tx,ty,tz])
    rotate(a = [-acos(az/sqrt(ax*ax+ay*ay+az*az)),0,-atan2(ax, ay)])
      cylinder(r=r_0,h=sqrt(ax*ax+ay*ay+az*az),center=true,$fn=genau); }

//Beginning of the main part
intersection() {
  for (k = [0:l_0:l_0*(repxy)]){      //x loop
    for (i = [0:l_0:l_0*(repxy)]){    //y loop
      for (j = [0:l_0:l_0*(repz)]){   //z loop
        intersection() {                //Creation of a single unit cell
          union() {
            bond(0+k,   0+i,   0+j,   l_0+k, l_0+i, l_0+j);
            bond(l_0+k, 0+i,   0+j,   0+k,   l_0+i, l_0+j);
            bond(0+k,   l_0+i, 0+j,   l_0+k, 0+i,   l_0+j);
            bond(0+k,   0+i,   l_0+j, l_0+k, l_0+i, 0+j);}
            translate([k,i,j])
              cube([l_0,l_0,l_0],false);} }}}
  translate([15,15,0])  //Intersection of the cylinder that defines the shape of the whole OCS with the unit cells. Maximum diameter 30 mm (If not repxy has to be changed)
    cylinder(r=r_ges,h=h_ges,center=false,$fn=genau);}

//Creation of the supporting cylinders
intersection() {
  union(){
    for (k = [0:(l_0):(l_0*(repxy)-0.5)]){    //x
      for (i = [0:(l_0):(l_0*(repxy)-0.5)]){  //y
        translate([0+k, 0+i, -3])
          cylinder(h = 5, r1 = 0.7, r2 = 0.7, center = false,$fn=genau); }}}
  translate([15,15,-3])
    cylinder(r=r_ges+5,h=50,center=false,$fn=genau);}
```

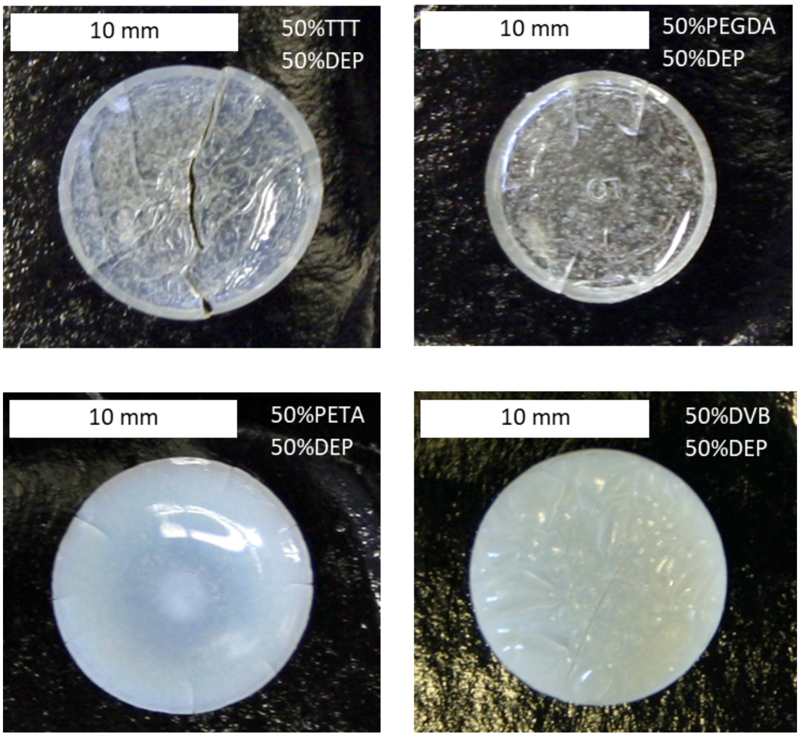

**Figure 7.1:** Pictures of polymerized and extracted pellets from the initial investigation of the polymerization time.

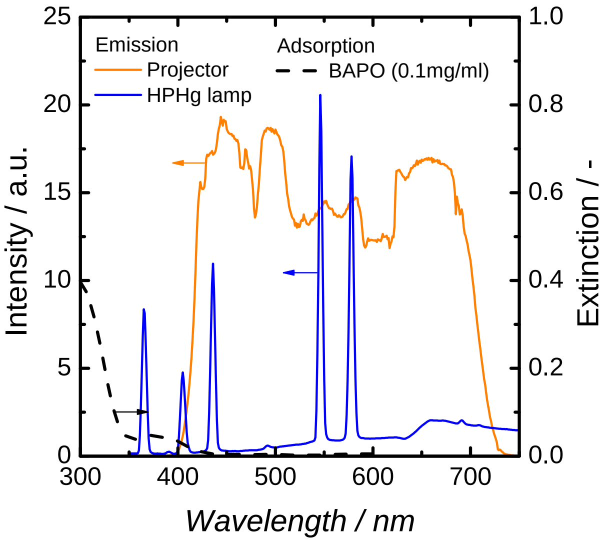

**Figure 7.2:** Emission spectrum of the 3D printers projector and a high-pressure mercury lamp, and absorption spectrum of the photoinitiator BAPO.

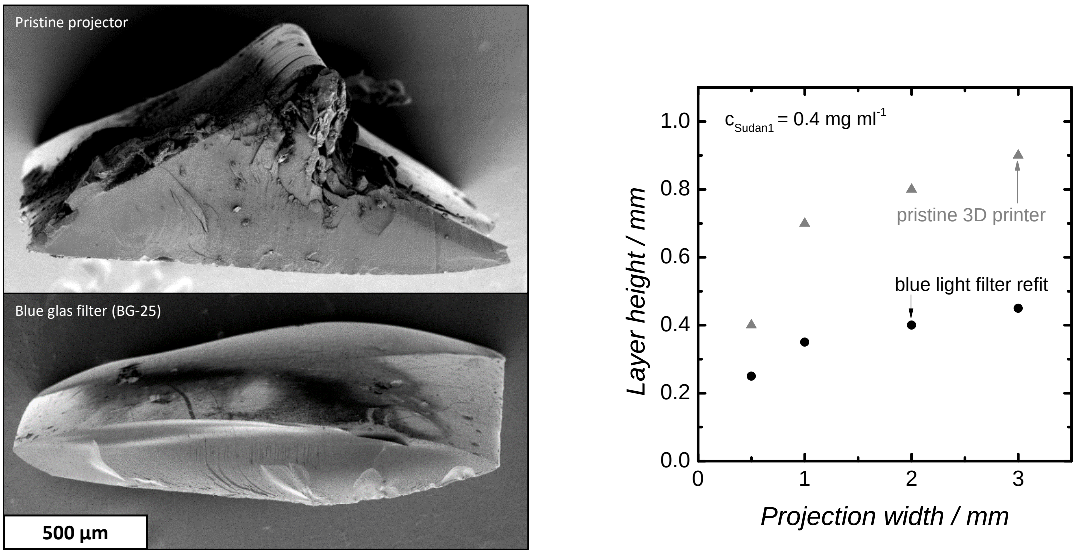

(a) (b)

**Figure 7.3:** Layer height measurements investigating the impact of a blue light filter added to the 3D printer using a photoresin with 35 vol% PETA, 35 vol% DVB, 30 vol% DIP and 0.4 mg ml$^{-1}$ sudan1 with an illumination time of 120 s; (a): SEM images of the crosssection of single 3D printed layers; (b): Layer height as a function of projection width.

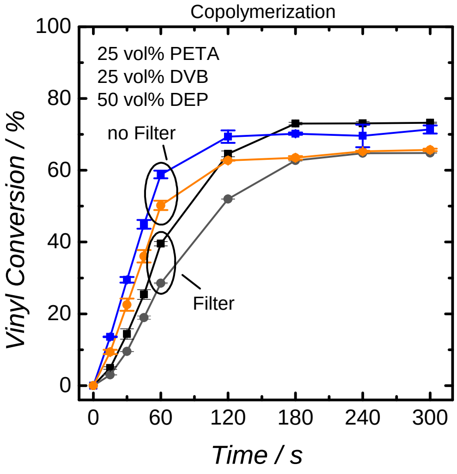

**Figure 7.4:** Conversion of aromatic (DVB) and acrylic (PETA) vinyl groups as a function of illumination time in the 3D printer investigating the impact of a blue light filter added to the 3D printer.

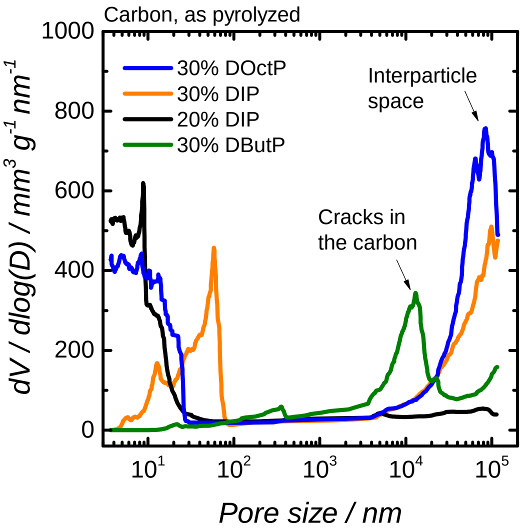

**Figure 7.5:** Pore size distribution from mercury intrusion porosimetry of oxidized (300 °C) and pyrolyzed (900 °C) 3D printed polymers produced with different concentrations and types of phthalates; large pore sizes seem to have a bigger differential volume due to the logarithmic calculation.

**Table 7.1:** Reduction of volume as a function of mass loss caused by $CO_2$ activation at 900 °C for 10, 20 or 30 hours of a 3D structure carbon monolith ($T_{Oxidation}$=300°C, $T_{Pyrolysis}$=900°C) with a diameter of 20 mm and a length of 45 mm based on a tetragonal unit cell ($d_{Cell}$=5,7mm, $d_{Cylinder}$=2mm).

| $t_{Activation}$ hours | m g | $h_{Mololith}$ mm | $d_{Mololith}$ mm |
|---|---|---|---|
| 0 | 5.19 | 45.5 | 20.8 |
| 10 | 3.17 | 43.6 | 19.5 |
| 20 | 1.70 | 40.0 | 18.3 |
| 30 | 0.87 | 34.7 | 15.1 |

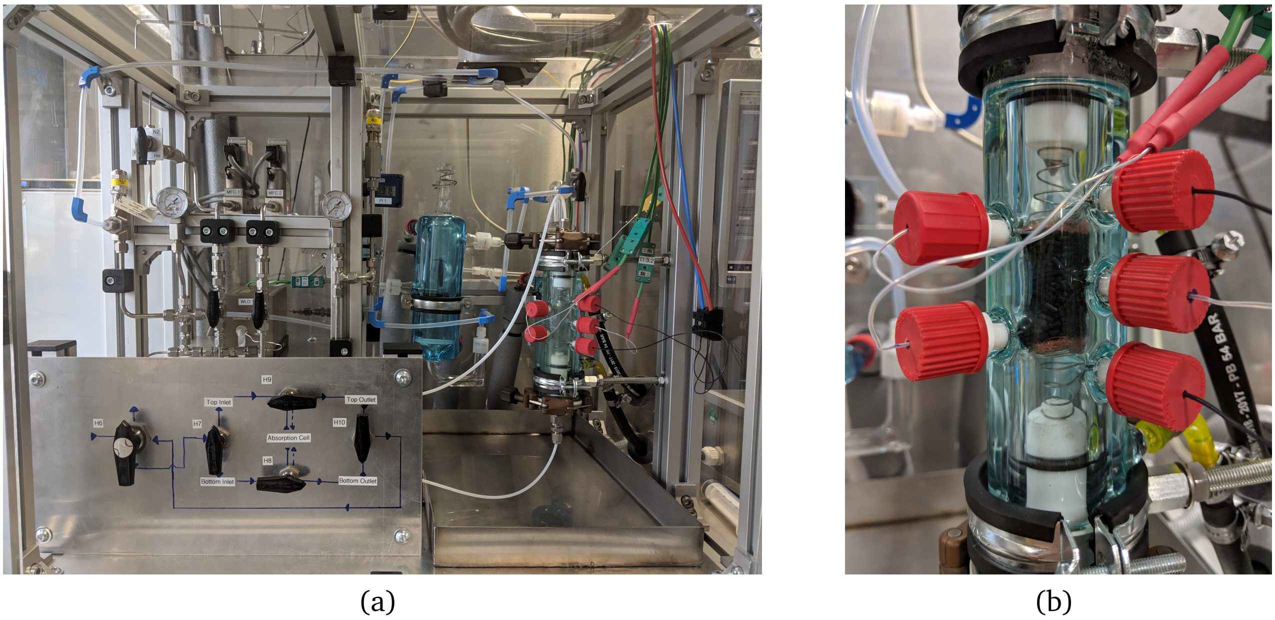

**Figure 7.6:** (a): Electric swing adsorption laboratory plant; (b): Adsorption cell with three thermocouples and two cables for power supply.

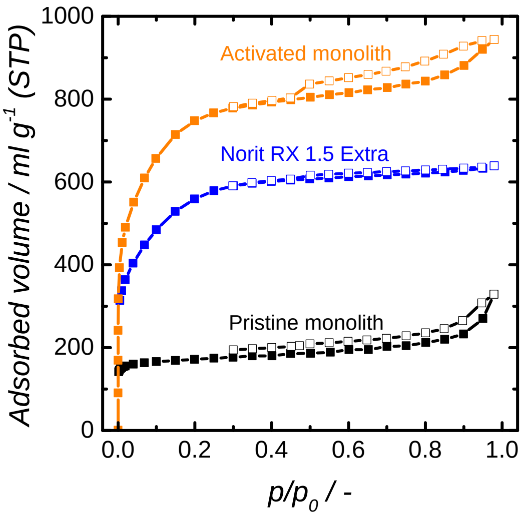

**Figure 7.7:** Nitrogen sorption isotherms (77 K) of the pristine and activated carbon, as well as the carbon pellets Norit RX 1.5 Extra.

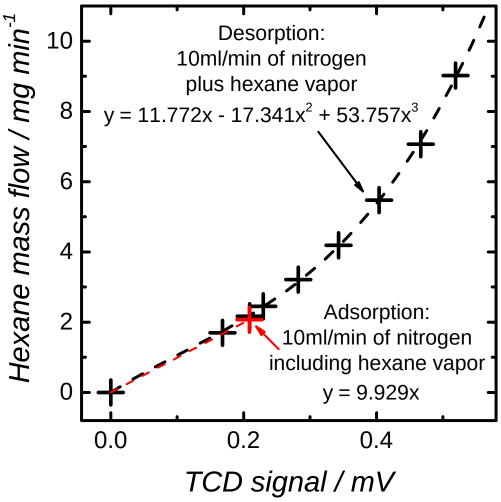

**Figure 7.8:** Black: Multi-point calibration for the desorption of hexane in the ESA calculated from the vapor-liquid equilibrium of hexane; Red: Single-point calibration for the adsorption of hexane in the ESA measured by condensing and weighing the hexane.

## References

[1] Oswin Öttinger et al. “Kohlenstoff-Metall Verbundwerkstoff”. German pat. 2017.

[2] Zhangwei Chen et al. “3D printing of ceramics: A review”. In: *Journal of the European Ceramic Society* 39.4 (2019), pp. 661–687.

[3] Niklas Hedin et al. “Adsorbents for the post-combustion capture of CO2 using rapid temperature swing or vacuum swing adsorption”. In: *Applied Energy* 104 (2013), pp. 418–433.

[4] Laishuan Liu et al. “Preparation of activated carbon honeycomb monolith directly from coal”. In: *Carbon* 44.8 (2006), pp. 1598–1601.

[5] Wilhelm Schwieger et al. “Hierarchy concepts: classification and preparation strategies for zeolite containing materials with hierarchical porosity”. In: *Chemical Society Reviews* 45.12 (2016), pp. 3353–3376.

[6] J. G. Calvert. “Glossary of atmospheric chemistry terms (Recommendations 1990)”. In: *Pure and Applied Chemistry* 62.11 (1990), p. 2167.

[7] M. Thommes. “Physical Adsorption Characterization of Nanoporous Materials”. In: *Chemie Ingenieur Technik* 82.7 (2010), pp. 1059–1073.

[8] D. H. Everett. “Manual of Symbols and Terminology for Physicochemical Quantities and Units, Appendix II: Definitions, Terminology and Symbols in Colloid and Surface Chemistry”. In: *Pure and Applied Chemistry* 31.4 (1972), pp. 577–638.

[9] Luca Riboldi et al. “Overview on Pressure Swing Adsorption (PSA) as CO2 Capture Technology: State-of-the-Art, Limits and Potentials”. In: *Energy Procedia* 114 (2017), pp. 2390–2400.

[10] Jorge A. Pena Lopez et al. “Natural gas based hydrogen production with zero carbon dioxide emissions”. In: *International Journal of Hydrogen Energy* 36.20 (2011), pp. 12853–12868.

[11] Rafael L. S. Canevesi et al. “Evaluation of simplified pressure swing adsorption cycles for biomethane production”. In: *Adsorption* 25.4 (2019), pp. 783–793.

[12] Marcin Liszka et al. “Energy and exergy analysis of hydrogen-oriented coal gasification with CO2 capture”. In: *Energy* 45.1 (2012), pp. 142–150.

[13] Wee Chong Kuah et al. “Industrial Scale Propylene/Propane Separation Using Pressure Vacuum Swing Adsorption”. In: *Industrial & Engineering Chemistry Research* 57.18 (2018), pp. 6451–6463.

[14] Fengsheng Su et al. “Adsorption, Desorption, and Thermodynamic Studies of CO2 with High-Amine-Loaded Multiwalled Carbon Nanotubes”. In: *Langmuir* 27.13 (2011), pp. 8090–8098.

[15] Babak Ashourirad et al. “Exceptional Gas Adsorption Properties by Nitrogen-Doped Porous Carbons Derived from Benzimidazole-Linked Polymers”. In: *Chemistry of Materials* 27.4 (2015), pp. 1349–1358.

[16] Abdelkrim Azzouz et al. “Truly reversible capture of CO2 by montmorillonite intercalated with soya oil-derived polyglycerols”. In: *International Journal of Greenhouse Gas Control* 17 (2013), pp. 140–147.

[17] Rui Feng et al. “Ethylene, xylene, toluene and hexane are major contributors of atmospheric ozone in Hangzhou, China, prior to the 2022 Asian Games”. In: *Environmental Chemistry Letters* 17.2 (2019), pp. 1151–1160.

[18] Xueyang Zhang et al. “Adsorption of VOCs onto engineered carbon materials: A review”. In: *Journal of Hazardous Materials* 338 (2017), pp. 102–123.

[19] Faisal I. Khan et al. “Removal of Volatile Organic Compounds from polluted air”. In: *Journal of Loss Prevention in the Process Industries* 13.6 (2000), pp. 527–545.

[20] M. Petkovska et al. “Temperature-Swing Gas Separation with Electrothermal Desorption Step”. In: *Separation Science and Technology* 26.3 (1991), pp. 425–444.

[21] Wilhelm Hauck et al. “Induktionsheizung: Anwendung auf die Regenerierung von beladenen Aktivkohle-Festbetten”. In: *Chemie Ingenieur Technik* 69.8 (1997), pp. 1138–1142.

[22] F. Moskal et al. “Internal heat source capacity at inductive heating in desorption step of ETSA process”. In: *International Communications in Heat and Mass Transfer* 34.5 (2007), pp. 579–586.

[23] J. Reuß et al. “Desorption by Microwaves: Mechanisms of Multicomponent Mixtures”. In: *Chemical Engineering & Technology* 25.4 (2002), pp. 381–384.

[24] Zaher Hashisho et al. “Microwave-Swing Adsorption To Capture and Recover Vapors from Air Streams with Activated Carbon Fiber Cloth”. In: *Environmental Science & Technology* 39.17 (2005), pp. 6851–6859.

[25] Bela M Fabuss et al. “Apparatus and process for desorption of filter beds by electric current”. U.S. pat. US3608273A. 1971.

[26] D. Downarowicz. “Adsorption characteristics of propan-2-ol vapours on activated carbon Sorbonorit 4 in electrothermal temperature swing adsorption process”. In: *Adsorption* 21.1 (2015), pp. 87–98.

[27] Lingai Luo et al. “Adsorption and electrothermal desorption of organic vapors using activated carbon adsorbents with novel morphologies”. In: *Carbon* 44.13 (2006), pp. 2715–2723.

[28] Rui P. P. L. Ribeiro et al. “Adsorption of Water Vapor on Carbon Molecular Sieve: Thermal and Electrothermal Regeneration Study”. In: *Industrial & Engineering Chemistry Research* 50.4 (2011), pp. 2144–2156.

[29] Jon D. Snyder et al. “Methyl Bromide Recovery on Activated Carbon with Repeated Adsorption and Electrothermal Regeneration”. In: *Industrial & Engineering Chemistry Research* 40.13 (2001), pp. 2925–2933.

[30] Katherine D. Dombrowski et al. “Organic Vapor Recovery and Energy Efficiency during Electric Regeneration of an Activated Carbon Fiber Cloth Adsorber”. In: *Journal of Environmental Engineering* 130.3 (2004), pp. 268–275.

[31] Hui An et al. “Desorption of CO2 from activated carbon fibre–phenolic resin composite by electrothermal effect”. In: *International Journal of Greenhouse Gas Control* 4.1 (2010), pp. 57–63.

[32] Tae Soo Lee et al. “Carbon dioxide removal using carbon monolith as electric swing adsorption to improve indoor air quality”. In: *Building and Environment* 92 (2015), pp. 209–221.

[33] Feng Dong Yu et al. “Electrothermal swing adsorption of toluene on an activated carbon monolith: Experiments and parametric theoretical study”. In: *Chemical Engineering and Processing: Process Intensification* 46.1 (2007), pp. 70–81.

[34] Carlos A. Grande et al. “Electric Swing Adsorption for CO2 removal from flue gases”. In: *International Journal of Greenhouse Gas Control* 2.2 (2008), pp. 194–202.

[35] Maria João Regufe et al. “Electrical conductive 3D-printed monolith adsorbent for CO2 capture”. In: *Microporous and Mesoporous Materials* 278 (2019), pp. 403–413.

[36] Kaitlin E. Mallouk et al. “Capture and Recovery of Isobutane by Electrothermal Swing Adsorption with Post-Desorption Liquefaction”. In: *Environmental Science & Technology* 44.18 (2010), pp. 7070–7075.

[37] Mehrdad Lordgooei et al. “Activated carbon cloth adsorption-cryogenic system to recover toxic volatile organic compounds”. In: *Gas Separation & Purification* 10.2 (1996), pp. 123–130.

[38] A. Subrenat et al. “Electrical behaviour of activated carbon cloth heated by the joule effect: desorption application”. In: *Carbon* 39.5 (2001), pp. 707–716.

[39] Albert Subrenat et al. “Thermal Behavior of Activated Carbon Cloths Heated by Joule Effect”. In: *Journal of Environmental Engineering* 129.12 (2003), pp. 1077–1084.

[40] Albert S. Subrenat et al. “VOLATILE ORGANIC COMPOUND (VOC) REMOVAL BY ADSORPTION ONTO ACTIVATED CARBON FIBER CLOTH AND ELECTROTHERMAL DESORPTION: AN INDUSTRIAL APPLICATION”. In: *Chemical Engineering Communications* 193.4 (2006), pp. 478–486.

[41] D. Camargo-Trillos et al. *Activated carbon monolith production by organic binders to capture CO2*. 2013.

[42] Masoud Jahandar Lashaki et al. “Stability of amine-functionalized CO2 adsorbents: a multifaceted puzzle”. In: *Chemical Society Reviews* 48.12 (2019), pp. 3320–3405.

[43] Feng Dong Yu et al. “Electrothermal Desorption Using Joule Effect on an Activated Carbon Monolith”. In: *Journal of Environmental Engineering* 130.3 (2004), pp. 242–248.

[44] R. P. P. L. Ribeiro et al. “Activated carbon honeycomb monolith – Zeolite 13X hybrid system to capture CO2 from flue gases employing Electric Swing Adsorption”. In: *Chemical Engineering Science* 104 (2013), pp. 304–318.

[45] Ruikai Zhao et al. “Thermodynamic analysis on carbon dioxide capture by Electric Swing Adsorption (ESA) technology”. In: *Journal of CO2 Utilization* 26 (2018), pp. 388–396.

[46] Klaus-Dirk Henning et al. “Carbon, 5. Activated Carbon”. In: *Ullmann’s Encyclopedia of Industrial Chemistry*. 2010.

[47] Mi Hyung Kim et al. “Analysis of environmental impact of activated carbon production from wood waste”. In: *Environmental Engineering Research* 24.1 (2019), pp. 117–126.

[48] Muhammad Khalid Rafiq et al. “Influence of Pyrolysis Temperature on Physico-Chemical Properties of Corn Stover (Zea mays L.) Biochar and Feasibility for Carbon Capture and Energy Balance”. In: *PLOS ONE* 11.6 (2016), e0156894.

[49] Longfeng Hu et al. “Natural Biomass-Derived Hierarchical Porous Carbon Synthesized by an in Situ Hard Template Coupled with NaOH Activation for Ultrahigh Rate Supercapacitors”. In: *ACS Sustainable Chemistry & Engineering* 6.11 (2018), pp. 13949–13959.

[50] Jaan Leis et al. “Carbon nanostructures produced by chlorinating aluminium carbide”. In: *Carbon* 39.13 (2001), pp. 2043–2048.

[51] Volker Presser et al. “Carbide-Derived Carbons – From Porous Networks to Nanotubes and Graphene”. In: *Advanced Functional Materials* 21.5 (2011), pp. 810–833.

[52] S. Osswald et al. “Porosity control in nanoporous carbide-derived carbon by oxidation in air and carbon dioxide”. In: *Journal of Solid State Chemistry* 182.7 (2009), pp. 1733–1741.

[53] M. Sevilla et al. “Activation of carbide-derived carbons: a route to materials with enhanced gas and energy storage properties”. In: *Journal of Materials Chemistry* 21.13 (2011), pp. 4727–4732.

[54] Johannes Landwehr et al. “Introducing sulphur surface groups in microporous carbons: A mechanistic study on carbide derived carbons”. In: *Catalysis Today* 301 (2018), pp. 191–195.

[55] Moriguchi Isamu et al. “Micelle-Templated Mesophases of Phenol-Formaldehyde Polymer”. In: *Chemistry Letters* 28.11 (1999), pp. 1171–1172.

[56] Guang-Ping Hao et al. “Structurally Designed Synthesis of Mechanically Stable Poly(benzoxazine-co-resol)-Based Porous Carbon Monoliths and Their Application as High-Performance CO2 Capture Sorbents”. In: *Journal of the American Chemical Society* 133.29 (2011), pp. 11378–11388.

[57] Masami Matsuda et al. “Influence of functional sulfonic acid groups on styrene–divinylbenzene copolymer pyrolysis”. In: *Journal of Polymer Science Part A: Polymer Chemistry* 25.2 (1987), pp. 669–673.

[58] Dhanya Puthusseri et al. “3D micro-porous conducting carbon beehive by single step polymer carbonization for high performance supercapacitors: the magic of in situ porogen formation”. In: *Energy & Environmental Science* 7.2 (2014), pp. 728–735.

[59] Mingjiang Zhong et al. “Electrochemically Active Nitrogen-Enriched Nanocarbons with Well-Defined Morphology Synthesized by Pyrolysis of Self-Assembled Block Copolymer”. In: *Journal of the American Chemical Society* 134.36 (2012), pp. 14846–14857.

[60] James W. Neely. “Characterization of polymer carbons derived from porous sulfonated polystyrene”. In: *Carbon* 19.1 (1981), pp. 27–36.

[61] Habtom D. Asfaw et al. “Boosting the thermal stability of emulsion–templated polymers via sulfonation: an efficient synthetic route to hierarchically porous carbon foams”. In: *ChemistrySelect* 1.4 (2016), pp. 784–792.

[62] Dong Wang et al. “Polymerization and carbonization of high internal phase emulsions”. In: *Polymer International* 54.2 (2005), pp. 297–303.

[63] Shozo Horikiri et al. “Process for production of carbon fiber”. U.S. pat. 1978.

[64] F. Kucera et al. “Sulfonation of solid polystyrene using gaseous sulfur trioxide”. In: *Polymer Engineering & Science* 49.9 (2009), pp. 1839–1845.

[65] Danish J. Malik et al. “Synthesis and characterization of nanostructured carbons with controlled porosity prepared from sulfonated divinylbiphenyl copolymers”. In: *Carbon* 46.2 (2008), pp. 310–319.

[66] Ana Jaqueline Barreto de Oliveira et al. “How to maintain the morphology of styrene-divinylbenzene copolymer beads during the sulfonation reaction”. In: *Materials Letters* 59.8 (2005), pp. 1089–1094.

[67] Munir Ahmed et al. “Effect of porosity on sulfonation of macroporous styrene-divinylbenzene beads”. In: *European Polymer Journal* 40.8 (2004), pp. 1609–1613.

[68] Robert T. Woodward et al. “Hypercrosslinked polyHIPEs as precursors to designable, hierarchically porous carbon foams”. In: *Polymer* 115 (2017), pp. 146–153.

[69] Weijiong Li et al. “Preparation and characterization of bimodal porous carbons derived from a styrene-divinylbenzene copolymer”. In: *Adsorption* 3.1 (1997), pp. 67–79.

[70] Danish J. Malik et al. “Nanostructured Synthetic Carbons Obtained by Pyrolysis of Spherical Acrylonitrile/Divinylbenzene Copolymers”. In: *PLOS ONE* 7.8 (2012), e43354.

[71] Motoyuki Suzuki. “Activated carbon fiber: Fundamentals and applications”. In: *Carbon* 32.4 (1994), pp. 577–586.

[72] Zhonglun Li et al. “Morphology and properties of porous polyimide films prepared through thermally induced phase separation”. In: *RSC Advances* 5.47 (2015), pp. 37837–37842.

[73] Fredrik Elwinger et al. “Diffusive Transport in Pores. Tortuosity and Molecular Interaction with the Pore Wall”. In: *The Journal of Physical Chemistry C* 121.25 (2017), pp. 13757–13764.

[74] Martin Hartmann et al. “Catalytic test reactions for the evaluation of hierarchical zeolites”. In: *Chemical Society Reviews* 45.12 (2016), pp. 3313–3330.

[75] Johannes Knossalla et al. “Shape-Controlled Nanoparticles in Pore-Confined Space”. In: *Journal of the American Chemical Society* 140.46 (2018), pp. 15684–15689.

[76] Benjamin Krüner et al. “Sub-micrometer Novolac-Derived Carbon Beads for High Performance Supercapacitors and Redox Electrolyte Energy Storage”. In: *ACS Applied Materials & Interfaces* 8.14 (2016), pp. 9104–9115.

[77] Hye-Min Lee et al. “Comparison studies on pore development mechanisms of activated hard carbons from polymeric resins and their applications for electrode materials”. In: *Renewable Energy* 144 (2019), pp. 116–122.

[78] Wen-Hong Li et al. “Preparation of sludge-based activated carbon made from paper mill sewage sludge by steam activation for dye wastewater treatment”. In: *Desalination* 278.1 (2011), pp. 179–185.

[79] S. Rio et al. “Preparation of Adsorbents from Sewage Sludge by Steam Activation for Industrial Emission Treatment”. In: *Process Safety and Environmental Protection* 84.4 (2006), pp. 258–264.

[80] A. Méndez et al. “Preparation of carbon-based adsorbents from pyrolysis and air activation of sewage sludges”. In: *Chemical Engineering Journal* 108.1 (2005), pp. 169–177.

[81] Marta Sevilla et al. “Energy storage applications of activated carbons: supercapacitors and hydrogen storage”. In: *Energy & Environmental Science* 7.4 (2014), pp. 1250–1280.

[82] Gianluca Barco et al. “The oxidized soot surface: Theoretical study of desorption mechanisms involving oxygenated functionalities and comparison with temperature programed desorption experiments”. In: *The Journal of Chemical Physics* 125.19 (2006), p. 194706.

[83] K. Jurewicz et al. “Efficient Capacitor Materials from Active Carbons Based on Coconut Shell/Melamine Precursors”. In: *Energy & Fuels* 24.6 (2010), pp. 3429–3435.

[84] Marit Jagtoyen et al. “Activated carbons from yellow poplar and white oak by H3PO4 activation”. In: *Carbon* 36.7 (1998), pp. 1085–1097.

[85] M. Molina-Sabio et al. “Role of chemical activation in the development of carbon porosity”. In: *Colloids and Surfaces A: Physicochemical and Engineering Aspects* 241.1 (2004), pp. 15–25.

[86] Hasan Sayğılı et al. “High surface area mesoporous activated carbon from tomato processing solid waste by zinc chloride activation: process optimization, characterization and dyes adsorption”. In: *Journal of Cleaner Production* 113 (2016), pp. 995–1004.

[87] Suwiwat Sangon et al. “Valorisation of waste rice straw for the production of highly effective carbon based adsorbents for dyes removal”. In: *Journal of Cleaner Production* 172 (2018), pp. 1128–1139.

[88] E. Gonzalez-Serrano et al. “Development of Porosity upon Chemical Activation of Kraft Lignin with ZnCl2”. In: *Industrial & Engineering Chemistry Research* 36.11 (1997), pp. 4832–4838.

[89] Jiacheng Wang et al. “KOH activation of carbon-based materials for energy storage”. In: *Journal of Materials Chemistry* 22.45 (2012), pp. 23710–23725.

[90] Chaoji Chen et al. “All-wood, low tortuosity, aqueous, biodegradable supercapacitors with ultra-high capacitance”. In: *Energy & Environmental Science* 10.2 (2017), pp. 538–545.

[91] Takashi Kyotani et al. “Formation of New Type of Porous Carbon by Carbonization in Zeolite Nanochannels”. In: *Chemistry of Materials* 9.2 (1997), pp. 609–615.

[92] Zhixin Ma et al. “Very High Surface Area Microporous Carbon with a Three-Dimensional Nano-Array Structure: Synthesis and Its Molecular Structure”. In: *Chemistry of Materials* 13.12 (2001), pp. 4413–4415.

[93] H. Nishihara et al. “Zeolite-templated carbons – three-dimensional microporous graphene frameworks”. In: *Chemical Communications* 54.45 (2018), pp. 5648–5673.

[94] Ryong Ryoo et al. “Synthesis of Highly Ordered Carbon Molecular Sieves via Template-Mediated Structural Transformation”. In: *The Journal of Physical Chemistry B* 103.37 (1999), pp. 7743–7746.

[95] R. Ryoo et al. “Ordered Mesoporous Carbons”. In: *Advanced Materials* 13.9 (2001), pp. 677–681.

[96] Michal Kruk et al. “Characterization of MCM-48 Silicas with Tailored Pore Sizes Synthesized via a Highly Efficient Procedure”. In: *Chemistry of Materials* 12.5 (2000), pp. 1414–1421.

[97] Michal Kruk et al. “Characterization of Ordered Mesoporous Carbons Synthesized Using MCM-48 Silicas as Templates”. In: *The Journal of Physical Chemistry B* 104.33 (2000), pp. 7960–7968.

[98] Liang Cao et al. “Synthesis of Ultra-Large-Pore SBA-15 Silica with Two-Dimensional Hexagonal Structure Using Triisopropylbenzene As Micelle Expander”. In: *Chemistry of Materials* 21.6 (2009), pp. 1144–1153.

[99] Lung-Ching Sang et al. “Ordered mesoporous carbon with tunable, unusually large pore size and well-controlled particle morphology”. In: *Journal of Materials Chemistry* 21.20 (2011), pp. 7410–7417.

[100] Kripal S. Lakhi et al. “Synthesis of mesoporous carbons with controlled morphology and pore diameters from SBA-15 prepared through the microwave-assisted process and their CO2 adsorption capacity”. In: *Microporous and Mesoporous Materials* 233 (2016), pp. 44–52.

[101] Seong-Su Kim et al. “A low cost route to hexagonal mesostructured carbon molecular sieves”. In: *Chemical Communications* 23 (2001), pp. 2418–2419.

[102] Michal Kruk et al. “Synthesis and Characterization of Hexagonally Ordered Carbon Nanopipes”. In: *Chemistry of Materials* 15.14 (2003), pp. 2815–2823.

[103] Anvar A. Zakhidov et al. “Carbon Structures with Three-Dimensional Periodicity at Optical Wavelengths”. In: *Science* 282.5390 (1998), p. 897.

[104] Youngchan Kim et al. “Synthesis of Porous Carbon Balls from Spherical Colloidal Crystal Templates”. In: *Langmuir* 28.28 (2012), pp. 10543–10550.

[105] Zongping Chen et al. “Three-dimensional flexible and conductive interconnected graphene networks grown by chemical vapour deposition”. In: *Nature Materials* 10.6 (2011), pp. 424–428.

[106] Hirotomo Nishihara et al. “Oxidation-Resistant and Elastic Mesoporous Carbon with Single-Layer Graphene Walls”. In: *Advanced Functional Materials* 26.35 (2016), pp. 6418–6427.

[107] Zuojiang Li et al. “A novel vesicular carbon synthesized using amphiphilic carbonaceous material and micelle templating approach”. In: *Carbon* 42.4 (2004), pp. 767–770.

[108] Chengdu Liang et al. “Synthesis of a Large-Scale Highly Ordered Porous Carbon Film by Self-Assembly of Block Copolymers”. In: *Angewandte Chemie International Edition* 43.43 (2004), pp. 5785–5789.

[109] H. Kosonen et al. “Functional Porous Structures Based on the Pyrolysis of Cured Templates of Block Copolymer and Phenolic Resin”. In: *Advanced Materials* 18.2 (2006), pp. 201–205.

[110] Shunsuke Tanaka et al. “Synthesis of ordered mesoporous carbons with channel structure from an organic–organic nanocomposite”. In: *Chemical Communications* 16 (2005), pp. 2125–2127.

[111] J. R. Conder et al. “Thermal decomposition of polyethylene glycol 20m and essential oils in gas—liquid chromatography and the effect of traces of oxygen”. In: *Journal of Chromatography A* 269 (1983), pp. 171–178.

[112] Fuqiang Zhang et al. “An Aqueous Cooperative Assembly Route To Synthesize Ordered Mesoporous Carbons with Controlled Structures and Morphology”. In: *Chemistry of Materials* 18.22 (2006), pp. 5279–5288.

[113] Yan Meng et al. “A Family of Highly Ordered Mesoporous Polymer Resin and Carbon Structures from Organic-Organic Self-Assembly”. In: *Chemistry of Materials* 18.18 (2006), pp. 4447–4464.

[114] Charles M. Hansen. *The three dimensional solubility parameter and solvent diffusion coefficient : Their importance in surface coating formulation*. Cph: Danish Technical Press, 1967.

[115] Dong-Xia Hao et al. “Porogen effects in synthesis of uniform micrometer-sized poly(divinylbenzene) microspheres with high surface areas”. In: *Journal of Colloid and Interface Science* 323.1 (2008), pp. 52–59.

[116] Stanislav Dubinsky et al. “Microfluidic Synthesis of Macroporous Copolymer Particles”. In: *Macromolecules* 41.10 (2008), pp. 3555–3561.

[117] Aleck H. Alexopoulos et al. “On the prediction of internal particle morphology in suspension polymerization of vinyl chloride. Part I: The effect of primary particle size distribution”. In: *Chemical Engineering Science* 62.15 (2007), pp. 3970–3983.

[118] Milan J. Benes et al. “Methacrylate-based chromatographic media”. In: *Journal of Separation Science* 28.15 (2005), pp. 1855–1875.

[119] A. I. Cooper et al. “Synthesis of Molded Monolithic Porous Polymers Using Supercritical Carbon Dioxide as the Porogenic Solvent”. In: *Advanced Materials* 11.15 (1999), pp. 1270–1274.

[120] Colin D. Wood et al. “Synthesis of Macroporous Polymer Beads by Suspension Polymerization Using Supercritical Carbon Dioxide as a Pressure-Adjustable Porogen”. In: *Macromolecules* 34.1 (2001), pp. 5–8.

[121] I. R. Kamrupi et al. “Synthesis of macroporous polymer particles by suspension polymerization using supercritical carbon dioxide as a pressure-adjustable porogen”. In: *Advances in Polymer Technology* 31.2 (2012), pp. 154–162.

[122] Haebong Byun et al. “Fabrication of macroporous carbon foam using glycol-derivatives as liquid templates”. In: *Macromolecular Research* 24.3 (2016), pp. 240–248.

[123] Yuerong Ba et al. “Nitrogen-doped hierarchical porous carbon derived from a chitosan/polyethylene glycol blend for high performance supercapacitors”. In: *RSC Advances* 8.13 (2018), pp. 7072–7079.

[124] Hedong Jiang et al. “Toward high-rate supercapacitor: Preparation of hierarchical porous carbon binder-free electrode with controllable texture”. In: *Applied Surface Science* 470 (2019), pp. 573–580.

[125] Yusei Kaneda et al. “Fabrication Procedure for Porous Carbon Material with Three Dimensionally Networked Structure: Ceramic Engineering and Science Proceedings Volume 39, Issue 3”. In: 2019, pp. 77–86.

[126] Xishi Wu et al. “Pore structure control of porous carbon via the synergistic effect of boric acid and divalent metal iron salt”. In: *Materials Letters* 255 (2019), p. 126539.

[127] Zhi-Guo Shi et al. “Carbon monolith: Preparation, characterization and application as microextraction fiber”. In: *Journal of Chromatography A* 1216.28 (2009), pp. 5333–5339.

[128] Julián Patiño et al. “Deep eutectic assisted synthesis of carbon adsorbents highly suitable for low-pressure separation of CO2–CH4 gas mixtures”. In: *Energy & Environmental Science* 5.9 (2012), pp. 8699–8707.

[129] N. López-Salas et al. “Use of Eutectic Mixtures for Preparation of Monolithic Carbons with CO2-Adsorption and Gas-Separation Capabilities”. In: *Langmuir* 30.41 (2014), pp. 12220–12228.

[130] L. E. Murr. “Open-cellular metal implant design and fabrication for biomechanical compatibility with bone using electron beam melting”. In: *Journal of the Mechanical Behavior of Biomedical Materials* 76 (2017), pp. 164–177.

[131] Zak C. Eckel et al. “Additive manufacturing of polymer-derived ceramics”. In: *Science* 351.6268 (2016), pp. 58–62.

[132] K. Swainson Wyn. “Method, Medium And Apparatus For Producing Three Dimensional Figure Product”. U.S. pat. US 4238840 A. 1980.

[133] W. Hull Charles. “Apparatus For Production Of Three-dimensional Objects By Stereolithography”. U.S. pat. US 4575330 A. 1986.

[134] Ze-Xian Low et al. “Perspective on 3D printing of separation membranes and comparison to related unconventional fabrication techniques”. In: *Journal of Membrane Science* 523 (2017), pp. 596–613.

[135] L. E. Murr. “A Metallographic Review of 3D Printing/Additive Manufacturing of Metal and Alloy Products and Components”. In: *Metallography, Microstructure, and Analysis* 7.2 (2018), pp. 103–132.

[136] Tae Jun Jeon et al. “Control of Porosity in Parts Produced by a Direct Laser Melting Process”. In: *Applied Sciences* 8.12 (2018), p. 2573.

[137] C. Buchanan et al. “Metal 3D printing in construction: A review of methods, research, applications, opportunities and challenges”. In: *Engineering Structures* 180 (2019), pp. 332–348.

[138] Swetha Chandrasekaran et al. “Direct ink writing of organic and carbon aerogels”. In: *Materials Horizons* 5.6 (2018), pp. 1166–1175.

[139] Moritz Emons et al. “Two-photon polymerization technique with sub-50 nm resolution by sub-10 fs laser pulses”. In: *Optical Materials Express* 2.7 (2012), pp. 942–947.

[140] Aparna Boddapati et al. “Gel time prediction of multifunctional acrylates using a kinetics model”. In: *Polymer* 52.3 (2011), pp. 866–873.

[141] L. U. Kim et al. “Effects of Molecular Structure of the Resins on the Volumetric Shrinkage and the Mechanical Strength of Dental Restorative Composites”. In: *Biomacromolecules* 7.9 (2006), pp. 2680–2687.

[142] Biwu Huang et al. “Preparation of a novel hybrid type photosensitive resin for stereolithography in 3D printing and testing on the accuracy of the fabricated parts”. In: *Journal of Wuhan University of Technology-Mater. Sci. Ed.* 32.3 (2017), pp. 726–732.

[143] R. Liska et al. “Photopolymers for rapid prototyping”. In: *Journal of Coatings Technology and Research* 4.4 (2007), pp. 505–510.

[144] Edward J. Murphy et al. “Method of forming a three-dimensional object by stereolithography and composition therefore”. U.S. pat. US4942001A. 1989.

[145] R. Liska et al. “Water-soluble photopolymers for rapid prototyping of cellular materials”. In: *Journal of Applied Polymer Science* 97.6 (2005), pp. 2286–2298.

[146] Beate Ganster et al. “New Photocleavable Structures. Diacylgermane-Based Photoinitiators for Visible Light Curing”. In: *Macromolecules* 41.7 (2008), pp. 2394–2400.

[147] Sigrid Jauk et al. “Photoinitiators with Functional Groups, 8”. In: *Macromolecular Rapid Communications* 26.21 (2005), pp. 1687–1692.

[148] Ali Bagheri et al. “Photopolymerization in 3D Printing”. In: *ACS Applied Polymer Materials* 1.4 (2019), pp. 593–611.

[149] Paricher Esfandiari et al. “Efficient stabilization of thiol-ene formulations in radical photopolymerization”. In: *Journal of Polymer Science Part A: Polymer Chemistry* 51.20 (2013), pp. 4261–4266.

[150] Ali Hayek et al. “Poly(glycidyl methacrylate)s with controlled molecular weights as low-shrinkage resins for 3D multibeam interference lithography”. In: *Journal of Materials Chemistry* 18.28 (2008), pp. 3316–3318.

[151] Stephen C. Lapin et al. “Stereolithography using vinyl ether-epoxide polymers”. U.S. pat. US5437964A. 1995.

[152] Simone Lantean et al. “Development of New Hybrid Acrylic/Epoxy DLP-3D Printable Materials”. In: *Inventions* 3 (2018), p. 29.

[153] Tetsuya Yamamura et al. “Photo-curable resin composition used for photo-fabrication of three-dimensional object”. U.S. pat. USRE42593E1. 1997.

[154] Surésh K. Rajaraman et al. “Interaction of epoxy and vinyl ethers during photoinitiated cationic polymerization”. In: *Journal of Polymer Science Part A: Polymer Chemistry* 37.21 (1999), pp. 4007–4018.

[155] James V. Crivello. “The discovery and development of onium salt cationic photoinitiators”. In: *Journal of Polymer Science Part A: Polymer Chemistry* 37.23 (1999), pp. 4241–4254.

[156] Hajime Kitano et al. “Unexpected visible-light-induced free radical photopolymerization at low light intensity and high viscosity using a titanocene photoinitiator”. In: *Journal of Applied Polymer Science* 128.1 (2013), pp. 611–618.

[157] Matthew J. Lacey et al. “Porosity Blocking in Highly Porous Carbon Black by PVdF Binder and Its Implications for the Li–S System”. In: *The Journal of Physical Chemistry C* 118.45 (2014), pp. 25890–25898.

[158] Cheng Zhu et al. “Supercapacitors Based on Three-Dimensional Hierarchical Graphene Aerogels with Periodic Macropores”. In: *Nano Letters* 16.6 (2016), pp. 3448–3456.

[159] Qiangqiang Zhang et al. “3D Printing of Graphene Aerogels”. In: *Small* 12.13 (2016), pp. 1702–1708.

[160] Gregorio de la Osa et al. “Printing of Graphene Nanoplatelets into Highly Electrically Conductive Three-Dimensional Porous Macrostructures”. In: *Chemistry of Materials* 28.17 (2016), pp. 6321–6328.

[161] Bin Bian et al. “3D printed porous carbon anode for enhanced power generation in microbial fuel cell”. In: *Nano Energy* 44 (2018), pp. 174–180.

[162] Daimay Lin-Vien et al. “CHAPTER 6 - Alkenes”. In: *The Handbook of Infrared and Raman Characteristic Frequencies of Organic Molecules*. San Diego: Academic Press, 1991, pp. 73–94.

[163] Seongok Han et al. “Thermal/oxidative degradation and stabilization of polyethylene glycol”. In: *Polymer* 38.2 (1997), pp. 317–323.

[164] Benoît Lessard et al. “Styrene/tert-Butyl Acrylate Random Copolymers Synthesized by Nitroxide-Mediated Polymerization: Effect of Free Nitroxide on Kinetics and Copolymer Composition”. In: *Macromolecules* 40.26 (2007), pp. 9284–9292.

[165] İbrahim Şahin et al. “Kinetics of Supercritical Drying of Gels”. In: *Gels* 4.1 (2018), p. 3.

[166] Jekaterina Jeromenok et al. “Restricted Access: On the Nature of Adsorption/Desorption Hysteresis in Amorphous, Microporous Polymeric Materials”. In: *Langmuir* 29.42 (2013), pp. 12982–12989.

[167] Stanislav Dubinsky et al. “Toward Controlling the Surface Morphology of Macroporous Copolymer Particles”. In: *Macromolecules* 42.6 (2009), pp. 1990–1994.

[168] Ali Shahverdi et al. “Selective oxidation of excess amorphous carbon during single-walled carbon nanotubes synthesis by induction thermal plasma process”. In:

[169] R. Marguta et al. “Molecular simulation and adsorption studies of n-hexane in ZSM-11 zeolites”. In: *Microporous and Mesoporous Materials* 142.1 (2011), pp. 258–267.

[170] T. M. Aminabhavi et al. “Density, Viscosity, and Refractive Index of the Binary Mixtures of Cyclohexane with Hexane, Heptane, Octane, Nonane, and Decane at (298.15, 303.15, and 308.15) K”. In: *Journal of Chemical & Engineering Data* 41.3 (1996), pp. 521–525.

[171] A. L. McClellan et al. “Cross-sectional areas of molecules adsorbed on solid surfaces”. In: *Journal of Colloid and Interface Science* 23.4 (1967), pp. 577–599.

Hendryk Steldinger

Feldbergplatz 3A

76199 Karlsruhe, Germany

April 29, 2020

**Erklärung**

Ich erkläre hiermit, dass ich meine Dissertation selbstständig und nur mit den angegebenen Hilfsmitteln angefertigt und noch keinen Promotionsversuch unternommen habe.

Hendryk Steldinger

Hendryk Steldinger

Feldbergplatz 3A

76199 Karlsruhe, Germany

April 29, 2020

**Erklärung**

Ich erkläre hiermit, dass die vorliegende elektronische Version meiner Dissertation identisch mit der vorliegenden schriflichen Fassung ist.

Hendryk Steldinger

## Lebenslauf

Name: Hendryk Steldinger

Addresse: Feldbergplatz 3A, 76199 Karlsruhe, Germany

Geboren: 05. Juli 1990, Berlin

### Ausbildung

| | |
|---|---|
| 05/2016 - 10/2019 | **Wissenschaftlicher Mitarbeiter / Doktorand**<br>*Technische Universität Darmstadt, Deutschland*<br>**Promotionsthema:** “3D Printing of Activated Carbon and Exemplary Application as Adsorbent in the Electric Swing Adsorption” |
| 10/2013 - 05/2016 | **Master of Science with Honours - Chemie- und Bioingenieurwesen**<br>*Friedrich-Alexander-Universität Erlangen-Nürnberg*<br>**Master thesis:** “Funktionalisierung von Karbid abgeleiteten Kohlenstoffen als Katalysator für die Veresterung von Levulinsäure mit Ethanol” |
| 10/2009 - 09/2013 | **Bachelor of Science - Verfahrenstechnik**<br>*Brandenburgische Technische Universität Cottbus*<br>**Bachelor thesis:** “Optimierung der Ligninseparation durch Laccase katalysierte Polymerisation im AlkaPolP Prozess.” |

Hendryk Steldinger